Antidust Coating for Lunar Applications

A Layer-by-Layer Approach

Pedro Carvalho

Delft University of Technology

Antidust Coating for Lunar Applications

A Layer-by-Layer Approach

by

Pedro Carvalho

to obtain the degree of Master of Science in Aerospace Engineering
at Delft University of Technology

To be defended publicly on Friday March 28, 2025 at 10:00 AM.

Student number:	5846064	
Supervisors:	Riccardo Biella,	TU Delft, Aerospace faculty
	Dr. Santiago J. García Espallargas,	TU Delft, Aerospace faculty
Thesis committee:	I. Uriol Balbin,	TU Delft, Aerospace faculty
	Dr. J. J. E. Teuwen,	TU Delft, Aerospace faculty

Cover: SEM image of the lunar dust simulant LMS-1. Magnification: 65x

TU Delft

Acknowledgments

It is done. Or in a more positive view, it has just begun. And I couldn't have done it alone.

To my supervisor, Santiago, thank you for your guidance, support, and attention throughout these months. Your out-of-the-box ideas made it possible to bring the Moon into the lab. To my daily supervisor, Riccardo, your constant support and patience have been invaluable. It wasn't easy, but we did it. A special thanks to Miisa, whose knowledge played a crucial role in completing this thesis. I would also like to express my gratitude to Dr. Yinglu Tang for kindly providing the zirconium diboride samples, to Natalia Guevara-Sotelo for the alumina platelets, to Antonio Mattia Grande from Politecnico di Milano for supplying the lunar simulant LMS-1, to Hans Brouwer at 3mE for his assistance in performing Spark Plasma Sintering and to Jeroen Koning at DEMO for his expertise and support in the manufacturing of the vacuum chamber. Their contributions greatly enhanced the quality and scope of this research.

Mãe e Pai, obrigado por terem sempre acreditado em mim. Sem o vosso apoio nunca teria conseguido estar aqui. Esta tese também é para vocês. Salva, não fizeste muito, mas obrigado na mesma por existires.

To my belle ragazze Anna, Sara and Emma thank you for bringing the warmth of Italy to this country. Manel and Mafalda, you made aerospace a more friendly environment from the beginning, in that chemistry class in the first year in Lisbon. To all of the "Study Group", each and every one of you have a special place in my heart and I will never forget how at home you made me feel. And Vasco, I hope you know how important you were this last year. You helped me through the complicated times and made the good ones even better. I hope I have the opportunity to do the same for you.

To my friends and family back in Madeira, you made me the person I am today. Trolhas, afilhados, primas, even 2750 km away, everyday I thought of the moments we spent together and that made all the difficult moments easier.

Pedro Carvalho
Delft, March 2025

Abstract

Lunar dust poses significant challenges for future lunar missions due to its high adherence, abrasive nature, and electrostatic charging behavior. This thesis investigates the development of an antidust coating composed of polyimide and alumina platelets, employing a layer-by-layer deposition approach to enhance durability and antidust performance. The study explores the fundamental adhesion mechanisms governing particle-surface interactions, including van der Waals, electrostatic, and capillary forces, and evaluates the coating's performance under lunar-relevant conditions.

A custom-designed vacuum chamber was utilized to simulate the lunar environment, allowing for systematic dust adhesion measurements under varying pressure and electrostatic conditions. The results demonstrate that the coating effectively reduces dust adhesion through both material composition and electrostatic repulsion. The multilayer structure ensures long-term functionality by allowing self-renewing exposure of alumina layers upon wear.

This research contributes a novel approach by integrating surface energy matching with electrostatic repulsion to minimize lunar dust accumulation. These findings provide a foundation for further development of durable antidust coatings, crucial for the success of future lunar missions.

Contents

List of Figures

List of Tables

Nomenclature

Abbreviations

Abbreviation	Definition
APTES	(3-Aminopropyl)triethoxysilane
CA	Contact angle
EDS	Energy dispersive X-ray spectroscopy
FTIR	Fourier Transform Infrared spectroscopy
ISRU	In-Situ resource utilization
LMS	Lunar Mare Simulant
NMP	1-methyl-2-pyrrolidinone
ODA	Oxydianiline
PAA	Polyamic acid
PA	Polyamide
PEEK	Polyether ether ketone
PFC	Perfluorocarbon
PI	Polyimide
PMMA	Polymethyl methacrylate
PTFE	Polytetrafluoroethylene
RH	Relative humidity
RMS	Root mean square
SEM	Scanning electron microscopy
SiC	Silicon carbide
SPS	Spark Plasma Sintering
UV	ultraviolet
ZrB_2	Zirconium diboride

Symbols

Symbol	Definition	Unit
A	Hamaker Constant	[J]
D_s	Minimum physical distance between two surfaces	[nm]
E_{IT}	Indentation modulus	[GPa]
F_{vdw}	Van der Waals force	[mN]
r	Roughness ratio	[-]
R	Radius of the particle	[µm]

Symbol	Definition	Unit
S_{dr}	Developed interfacial area ratio	[-]
S_q	Root mean square height	[µm]
$\gamma_{s,p}$	Interfacial tension	[mn/M]
θ_m	Measured contact angle	[º]
θ_Y	Actual contact angle	[º]

1

Introduction

”It’s almost like a powder.” These words that came before one of the most iconic quotes in the history of mankind, describe the surface of the Moon as Neil Armstrong, commander of NASA’s Apollo 11 mission, descends the ladder of the Apollo Lunar Module.

From then on, the problems with the lunar dust started to become evident. During the Apollo missions it obstructed chamber seals, ruined spacesuits, deteriorated mechanical gears, and reduced the lunar rover’s range. Therefore, it was determined that one of the primary obstacles to a long-term presence on the Moon is the mitigation of dust adherence. For both manned and unmanned missions, dust mitigation is essential because over time, dust can contaminate and deteriorate vital infrastructures including dwellings, solar panels, greenhouse windows, spacesuits, surface rovers, and excavation equipment [32].

The present study aims to develop an antidust coating composed of polyimide and alumina platelets and to evaluate its antidust performance in a context relevant to the lunar environment.

The literature review in this chapter examines the nature of the lunar environment and how it can be used in designing antidust surfaces. The mechanisms that rule particle adhesion were also explored. The review revealed that few passive antidust coatings based on electrostatic repulsion exist, highlighting a gap in current research and opportunities for innovation in dust mitigation strategies. Based on these findings, the research question and objectives were formulated, focusing on the feasibility and performance of a layer-by-layer polyimide-alumina coating for lunar applications.

Chapter 2 details the manufacturing of the coatings and the characterization methods used to assess their physical and chemical properties.

Chapter 3 describes the experimental setup developed to simulate the lunar environment and to test the antidust properties of the coating. Additionally, it presents the antidust performance tests, designed to explore different aspects of the coating’s behavior under varying environmental and experimental conditions. The results for each test case are discussed in depth, analyzing the effectiveness of the coating in repelling dust.

Chapter 4 summarizes the key findings of the study, drawing conclusions regarding the research questions. Additionally, recommendations for future research are provided, outlining potential improvements and further investigations to refine passive antidust coatings for lunar applications.

1.1. Regolith

The lunar surface is covered by a layer of fine particulate material known as lunar regolith, which extends several meters into the lunar soil bed. The regolith's formation can be traced back to meteorite impacts that induce fragmentation, glass formation and melting processes [30].The thickness of the regolith layer varies across the Moon, reaching depths of around 5 meters in the mare regions and up to 10 meters in the highlands. With a density of roughly 1.5 g/cm^3, the regolith has a fine gray appearance, composed of loose soil, breccia, and rock fragments that originate from the underlying bedrock [52]. Breccia is a type of rock that forms when fragments of regolith and rock are fused together through shock-metamorphism, a process driven by meteorite impacts[17].

1.1.1. Physical and chemical composition

Lunar regolith exists in different particle size distributions, with particles smaller than 20 μm being classified as lunar dust. These fine particles constitute roughly 20% of the total regolith mass [59]. The morphology of lunar dust grains is highly variable, ranging from spherical to extremely angular shapes, with many exhibiting sharp edges. Generally, dust grains tend to be elongated, and due to their low electrical conductivity, they can accumulate and retain charge in the lunar environment[48].

The chemical composition of lunar regolith has been extensively analyzed, particularly through samples returned from lunar missions. These analyses reveal that the primary constituents of lunar dust include olivine, plagioclase, pyroxene, and agglutinitic glass, along with trace amounts of other minerals [21]. However, the chemical makeup varies significantly across different regions of the Moon. Highland regions are richer in calcium (Ca) and aluminum (Al), while mare regions have a higher concentration of titanium (Ti) and iron (Fe)[30]. As seen in Table 1.1, the predominant minerals found in lunar regolith are silicates. While this table provides a general overview of lunar regolith composition, it is important to note that local variations exist, making any single dataset non-representative of the entire lunar surface.

Table 1.1: Chemical composition of lunar soil shown in abundance of oxides as lithology signature [17].

Compound	**Formula**	**Concentration (%)**
Silica	SiO_2	42 - 48
Alumina	Al_2O_3	12 - 27
Lime	CaO	10 - 17
Iron (II) Oxide	FeO	4 - 18
Magnesia	MgO	4 - 11
Titanium Dioxide	TiO_2	1 - 7
Sodium Oxide	Na_2O	0.4 - 0.7

1.2. The problem of Moon dust

The behavior of lunar dust particles is fundamentally shaped by their long-term exposure, over millions or even billions of years, to extreme environmental conditions. Unlike on Earth, due to the lack of a global magnetic field or protective atmosphere, lunar dust is subjected to vacuum, solar irradiation, solar electron and ion bombardment and micrometeoroid impacts. These conditions lead to unique surface properties of the lunar dust [2].

One of the key factors influencing lunar dust behavior is the absence of passivation mechanisms. While on Earth fracture surfaces are almost instantly passivated by oxygen or water in the atmosphere that react with newly exposed molecular bonds, in a lunar setting these surfaces can remain pristine for extended periods. The surface condition of lunar regolith particles is then defined by their unpassivated, chemically reactive state [2]. The lack of erosion of generated debris often forms sharp-edged particles, as seen in Figure 1.1. These act as a severe abrasive agent [30].

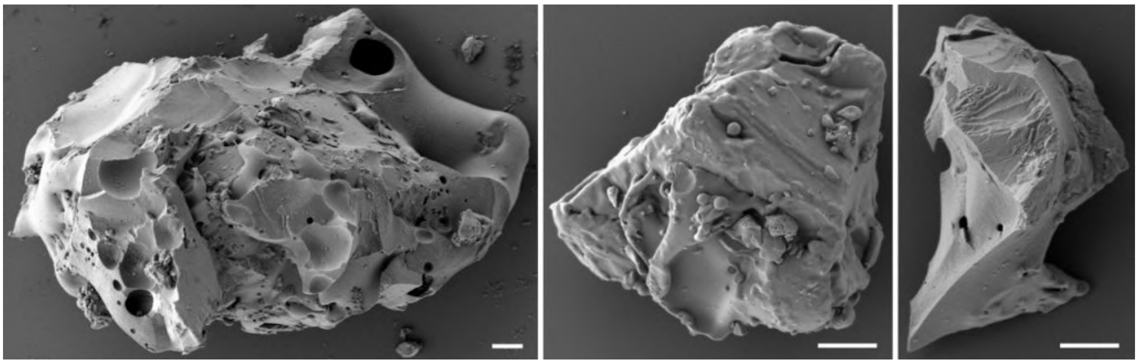

Figure 1.1: Micrographs of three particles of Moon dust collected during the Apollo 11 mission in 1969 [13].

1.2.1. Electrostatic Charging of Lunar Dust

Another major consequence of the lunar environment is the dynamic electrostatic charging of dust particles, due to exposure to solar radiation and interactions with surrounding plasma environment, illustrated in 1.2.

The primary charging mechanism on the sunlit side of the Moon is photoelectric ionization, driven by exposure to solar ultraviolet (UV) radiation. The high-energy photons induce photoemission of electrons from the lunar regolith, that leads to a net positive charge accumulation on the dayside. In the dark side of the Moon, the lunar surface typically acquires a negative charge. This is the result of the plasma electrons moving faster than the plasma positive ions. Consequently, there is a flux of electrons moving towards the lunar surface greater than the flux of ions, causing a net negative charge accumulation [49].

The Suprathermal Ion Detector Experiments (SIDE) deployed on the Moon during the Apollo missions provided valuable quantitative data on lunar surface charging. Measurements indicated that the surface potential can reach +10V on the dayside, while on the nightside, it can drop to -100V due to plasma interactions. [49].

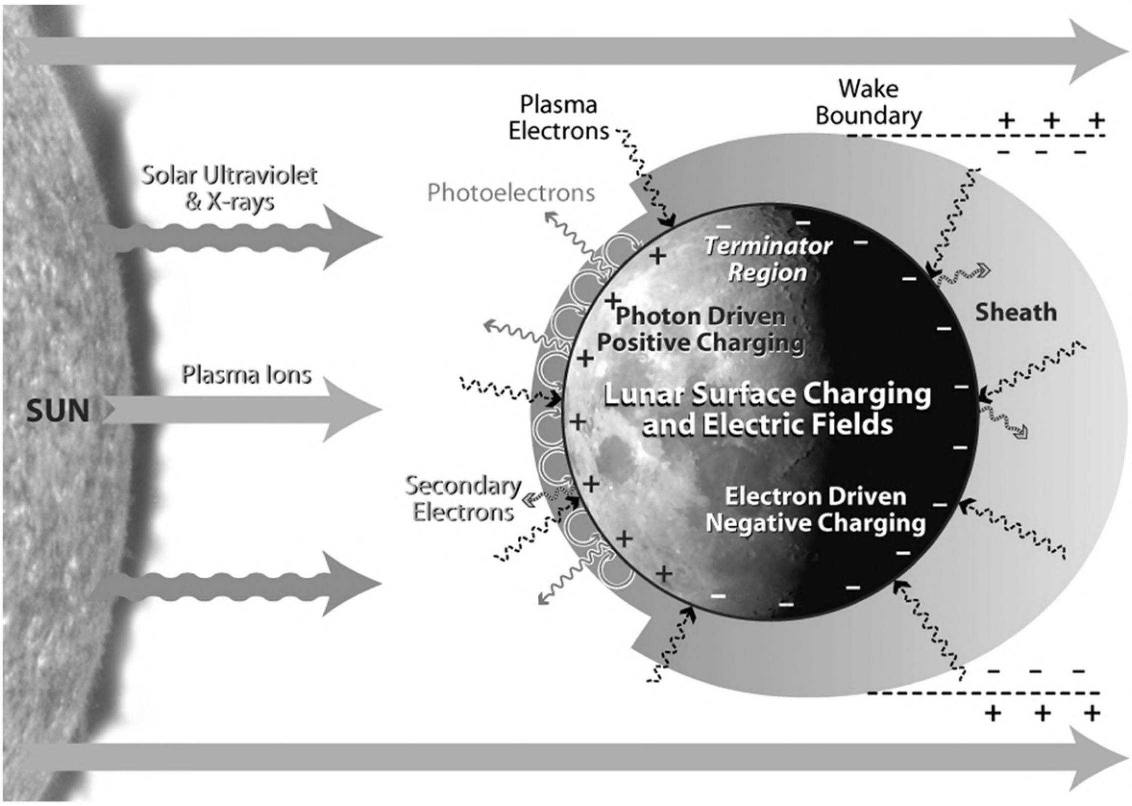

Figure 1.2: Schematic of the electric field environment of the Moon [49].

1.2.2. Lunar Dust Mobilization

Lunar dust can move across the surface due to various natural and anthropogenic forces. The most common natural process responsible for dust mobilization is micrometeoroid impact, which ejects particles from the surface and redistributes them across the landscape. However, electrostatic forces can also cause dust movement. [9]. Laboratory experiments have demonstrated that electric fields generated by plasma sheaths can levitate small charged particles several centimeters above a lunar dust simulant surface [52]. This levitated layer of fine charged lunar dust particles means that even a surface far from any anthropogenic disturbances and not in contact with the soil can accumulate layers of dust over time.

With the advent of Moon exploration, human and robotic activity is now also another factor to consider. Human activities such as spacecraft landings on the lunar surface contribute significantly to the phenomenon of impact wear. Soft landings on the Moon involve the use of retrograde rocket engines, which accelerate regolith particles and cause erosive wear on nearby structures. Rocket exhaust impingement creates high-speed dust flows, with particles traveling at velocities between 50 and 2000 m/s, that can impact infrastructure and scientific instruments, and habitats. Particle size, shape, and hardness, as well as impact parameters like velocity and angle, all affect the rate of erosion [30].

1.2.3. The Adverse Effects of Lunar Dust

Lunar dust poses severe challenges to both human exploration and technological operations on the Moon:

Surface Adhesion and Contamination:

First of all, lunar dust clings to surfaces due to its small particle size, irregular morphology, high surface activity, and electrostatic charge. This makes it difficult to remove from spacesuits, mechanical systems, and optical instruments, leading to operational failures [32].

Abrasion and Wear on Mechanical Components:

Secondly, abrasion caused by the hardness and roughness of dust grains can accelerate wear on mechanical components, particularly affecting mechanisms with moving parts such as gears, bearings and seals [15].

Thermal and Optical Degradation:

Furthermore, dust accumulation on solar panels, optical surfaces, and radiators cause thermal and optical effects that eventually reduce their performance. It affects thermal optical properties such as absorptance and emittance and therefore influences thermal radiation of instruments to space, affecting their radiative balance and potentially leading to overheating or energy loss [15].

Health Hazards for Astronauts:

Last but not least, fine dust particles pose a significant respiratory risk when inhaled within a pressurized habitat or spacecraft. The reactive nature of lunar dust can cause lung irritation, with potential long-term health implications for astronauts on extended lunar missions.[9]

1.3. Particle-surface interaction

The adhesion of particles to surfaces is influenced by multiple factors, including environmental conditions, dust characteristics, surface treatments, and the actual contact area between particles and surfaces. The most common adhesion forces that govern these interactions include van der Waals forces, electrostatic forces and capillary forces[11]. Additionally, gravitational forces become significant for larger particles, particularly those greater than 500 µm in diameter [43].

1.3.1. Van der Waals Forces

Van der Waals forces consist of dispersion and polarization forces, both of which originate from dipole interactions at the atomic and molecular level. These forces arise due to temporary or permanent dipole moments induced by the electric fields of nearby charges and dipoles. Dispersion forces, also known as London forces, result from fluctuating electron densities, creating instantaneous dipoles that induce attraction between otherwise neutral atoms and molecules. Polarization forces, on the other hand, occur when a permanent dipole induces a dipole moment in a nearby molecule, enhancing the attractive interaction. Dispersion forces provide the most significant contribution to adhesion between atoms and molecules. These forces act between all types of matter, including totally neutral atoms and molecules, and they generally exceed dipole-dependent induction and orientation forces except in cases involving small, highly polar molecules [12].

For a spherical particle near a flat surface (Figure 1.3), the van der Waals force is given by the equation from Krupp (1967)[28]:

$$F_{vdw} = \frac{AR}{6D_s^2} \tag{1.1}$$

Rabinovich [45] later adapted this equation to account for the effect of surface roughness, proposing an adhesion model that can be expressed as:

$$F_{vdw} = \frac{AR}{6D_s^2}\left(\frac{1}{1+\frac{R}{1.48S_q}} + \frac{1}{\left(1+\frac{1.48S_q}{D_s}\right)^2}\right) \tag{1.2}$$

where R is the radius of the dust particle, D_s is the minimum physical distance between two surfaces (approximately 0.4 nm), and S_q is the root mean square height of the asperity of the rough surface. A is the Hamaker constant. The Hamaker constant's calculation is far from trivial. Israelachvili (2011)[25] derived a complex analytical formula based on Lifshitz theory. However, due to the complexity of this approach, multiple researchers have proposed simplified models for particle adhesion, although with little consensus among them [16][15][53]. Despite these discrepancies, a common feature among these models is the dependence of the Hamaker constant on interfacial tension between the materials in contact ($\gamma_{s,p}$):

$$\mathrm{A} = 24\pi D_s^2\gamma_{s,p} \tag{1.3}$$

Following the work of El Baraka et al. (2023) [16], the Girifalco and Good (1957)[20] rule provides an empirical approach to link interfacial tension with the surface energies of each material, giving us a practical equation that allows for estimating the Hamaker constant in particle adhesion studies and that equates the interfacial tension with the Lifshitz–Van der Waals interactions between two materials ($\gamma_{s,p}^{LW}$):

$$\gamma_{s,p^{LW}} = \left(\sqrt{\gamma_s^{LW}} - \sqrt{\gamma_p^{LW}}\right)^2 \tag{1.4}$$

where γ_s^{LW} and γ_p^{LW} are the Lifshitz–Van der Waals components of the surface energy of the surface and of the particle.

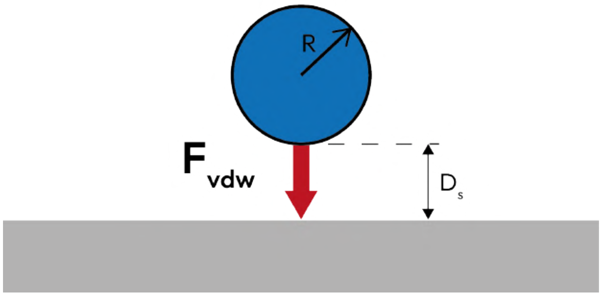

Figure 1.3: Illustration of van der Waals forces on a flat surface.

1.3.2. Electrostatic forces

One of the situations of electrostatic interactions occur when charged particles come into contact with a conducting surface, inducing an opposite image charge that results in a Coulombic attraction, like the one in Figure 1.4. The electrostatic force can be expressed as [8]:

$$F_{\mathrm{e}} = \frac{q^2}{4\pi\varepsilon\varepsilon_o l^2} \tag{1.5}$$

where q is the charge of the dust particle, ε is the dielectric constant of the medium (for air, ε = 1), ε_o is the permittivity of free space, and l is the separation distance between charge centers (approximately 2R for a spherical particle).

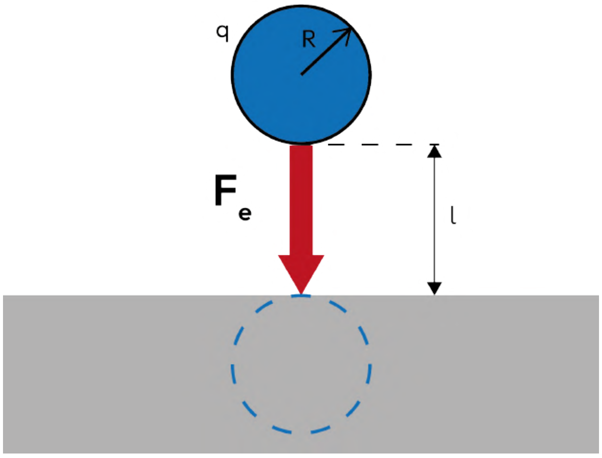

Figure 1.4: Illustration of electrostatic attraction on a flat surface.

On non-conductive materials, electrostatic force can also emerge from tribocharging, the transfer of electrons from surfaces in contact, and it is connected to the difference in the materials' work function. The work function refers to the least amount of energy that is required to extract an electron from an electrically neutral material to a point right outside the solid's surface. When different materials come into contact, a transfer of electrons occurs from the one with lower work function to the one with higher work function. This means that even particles and surfaces previously electrostatically neutral, can acquire charge and therefore be affected by the electrostatic attraction [52].

However, particles and surfaces may already possess a charge before coming into contact due to external environmental conditions. This initial charge state will influence the interaction with the incoming particles. Depending on the relative charge magnitudes and polarities, this Coulombic force can also be repulsive, in case the particles and the surface have the same sign.

1.3.3. Capillary forces

Capillary forces arise from the presence of moisture in the surrounding environment, which promotes adhesion through capillary action [27]. When humidity is present, water condenses at the surface creating a thin water layer that can form a concave meniscus between the particle and the surface, as seen in Figure 1.5. As the relative humidity (RH) increases, capillary forces gradually become more significant. Below a critical threshold of 60–70% RH, the increase in adhesion is gradual, but beyond this point, this force rises sharply [24].

The capillary force between a spherical particle and a flat surface is given by [44]:

$$F_c = 4\pi R\gamma \cos\theta \left[1 - \frac{D_s}{2r\cos\theta}\right] \tag{1.6}$$

where R is the particle radius, γ is the surface tension of the liquid, θ is the contact angle, and r is the equilibrium radius of the meniscus, which is determined by using Kelvin's equation, that accounts for relative humidity effects.

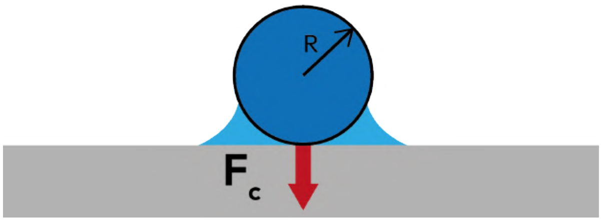

Figure 1.5: Illustration of capillary forces on a flat surface.

1.3.4. Gravitational force

For larger dust particles, gravitational attraction, as depicted in Figure 1.6, also plays a role in adhesion. The gravitational force for a spherical particle is given by:

$$F_{\text{gravily}} = \frac{4}{3}\pi R^3 \rho g \tag{1.7}$$

where R is the particle radius, ρ is the dust particle density, and g is the gravitational acceleration.

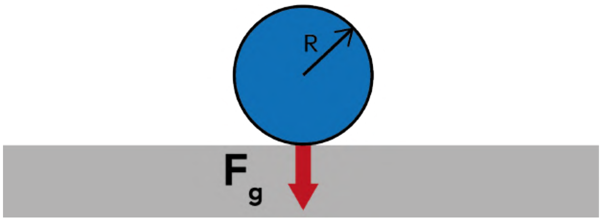

Figure 1.6: Illustration of gravitational forces on a flat surface.

1.3.5. Lunar dust adhesion

The lunar environment has some peculiarities that turn the issue of particle adhesion different from adhesion of dust here on Earth. First, its lack of moisture in its very fine atmosphere means that capillary forces can be neglected [15]. Furthermore, gravity is roughly a sixth of the one on earth, so gravitational force is much weaker and plays a negligible role in fine dust adhesion [52]. On the other hand, the lunar surface is largely non-conductive, due to the nonexistence of liquid water and the fact that the regolith's minerals are insulators. As mentioned before, charges will then remain on the particles on the surface of the Moon. [52].

This means that, when regolith dust is deposited on a surface, the two factors that most contribute to adhesion are surface energy related adhesion forces (van der Waals), at short-range, and static-electric-image forces at long-range [59].

1.4. Antidust approaches

Dust mitigation strategies can be categorized into active and passive approaches, each with distinct mechanisms and challenges. Active approaches require an external input such as human intervention or mechanical/electrical systems to remove dust from surfaces, whereas passive approaches rely on pre-treated materials that inherently resist dust adhesion without requiring additional energy [59].

Active dust mitigation methods involve direct external actions to remove adhered particles. Examples are fluidal cleaning, mechanical sweeping or electrostatic/electrodynamic particle manipulation. Fluidal methods describes techniques that use liquids, gels, foams, and gases to remove particles from surfaces. Mechanical cleaning includes brushing, blowing, vibrating, or ultrasonic methods to dislodge and remove dust particles. Electrodynamic/electrostatic methods work by generating electric fields to manipulate dust particles, either by repelling them or causing them to move along the surface. This approach is inspired by naturally occurring solar-induced electrostatic levitation of dust particles on the Moon[3].

The majority of modern antidust technologies focus on removing dust after it has already adhered to surfaces. However, little attention is given to preventing dust from accumulating in the first place, which remains a significant gap in dust mitigation research [59].

Each of these active techniques presents specific challenges when considering their application in lunar environments. Fluidal washing methods, while effective, are impractical due to the extreme scarcity of water on the Moon, making it unfeasible to bring sufficient quantities for regular cleaning. Mechanical brushes, though simple, are often inefficient, as they can damage pre-existing coatings or protective layers. Electrodynamic methods face issues related to limited energy availability and the potential for mechanical or electrical failures during long-duration missions [54].

On the other hand, passive dust mitigation technologies aim to reduce dust adhesion from the start, eliminating the need for external inputs or frequent maintenance. These methods typically involve modifying the surface properties of materials through chemical or physical treatments. [3]

Passive approaches hold significant potential for long-term lunar operations, as they minimize the need for astronaut or robotic intervention. A successful passive antidust solution would prevent dust accumulation rather than requiring frequent removal efforts, offering a low-maintenance, energy-efficient alternative to active methods.

Surface roughness

Among passive dust mitigation technologies, modifying surface roughness at the micro- and nanoscale has emerged as a promising approach. By engineering surface topographies, it is possible to reduce dust adhesion forces and prevent particles from settling permanently. Techniques such as composite etching and nanocoining have demonstrated significant potential in creating surfaces that inherently resist dust accumulation.

Nature provides effective models for surface roughness-based dust mitigation. The lotus leaf is well-known for its self-cleaning properties, which arise from its hierarchical micro- and nanostructures that create a superhydrophobic effect. This lotus effect, illustrated in Figure 1.7 on a leaf of *Colocasia esculenta*, is based on the Cassie-Baxter state, in which air pockets prevent water from fully wetting the surface. The same nano/microstructures that repel water droplets also reduce dust adhesion by minimizing the contact area between dust particles and the surface. This reduces the force required to detach particles, making it easier for them to be removed with minimal external force [18].

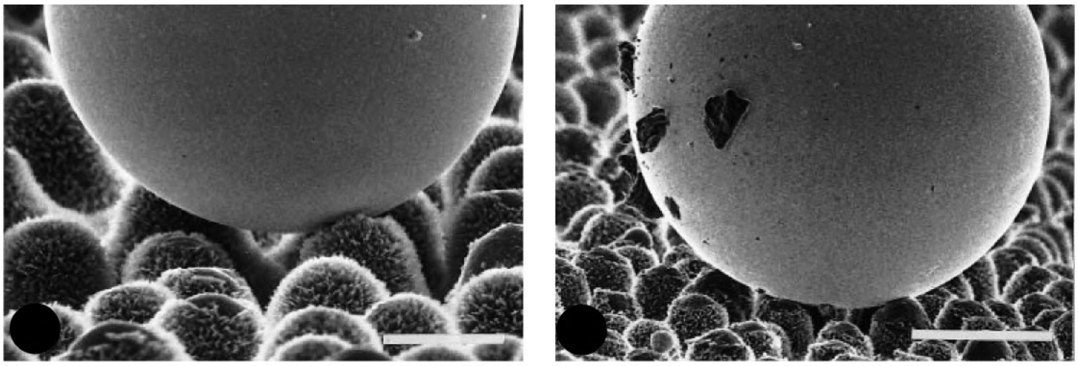

Figure 1.7: Mercury droplet on the leaf surface of *Colocasia esculenta* demonstrating the Lotus-Effect [6].

Inspired by biological surface structures, Lee et al. (2023) [32] engineered surfaces with controlled micro- and nanoscale textures using a scalable nanocoining and nanoimprint process. These precisely structured surfaces were applied to polycarbonate substrates, as seen in Figure 1.8, demonstrating a drastic reduction in dust adhesion. By minimizing the contact area between the material and the dust, these surfaces showed an impressive 93% reduction in dust adhesion compared to smooth surfaces. In experiments using lunar dust simulants, almost all particles larger than 2 µm were removed under the influence of Earth's gravity alone, without requiring additional forces.

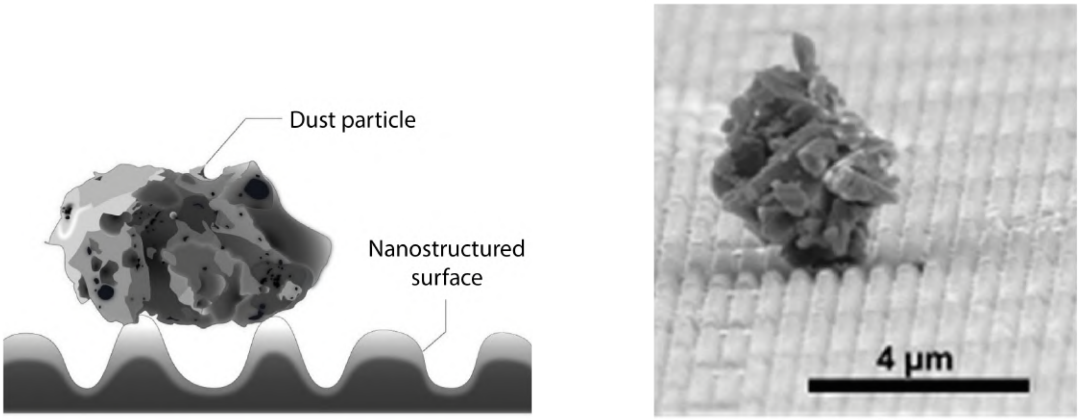

Figure 1.8: Sketch of dust on top of a textured surface (left) and scanning electron microscopy (SEM) image of an aggregation of dust particles on top of the 500 nm period textured surface (right) [32].

A similar approach was taken by Wang et al. (2022) [54], who created hierarchical multiscale surface roughness on aluminum substrates through combined chemical and electrochemical etching. Three different surface textures were tested: Al-C (chemically etched), Al-E (electrochemically etched) and Al-CE (combined chemical and electrochemical etching). The surface morphologies of these treated and untreated aluminum samples (Al-U) were analyzed using scanning electron microscopy (SEM), as shown in Figure 1.9. The results revealed that these engineered rough surfaces significantly reduced dust adhesion. The lunar dust adhesion force was reduced by 80%, dropping from 45.53 nN on untreated aluminum to 8.89 nN on the etched surfaces. Moreover, when the etched samples were placed in a vertical orientation, dust coverage was dramatically reduced to 2.19%, compared to 9.11% on untreated aluminum surfaces.

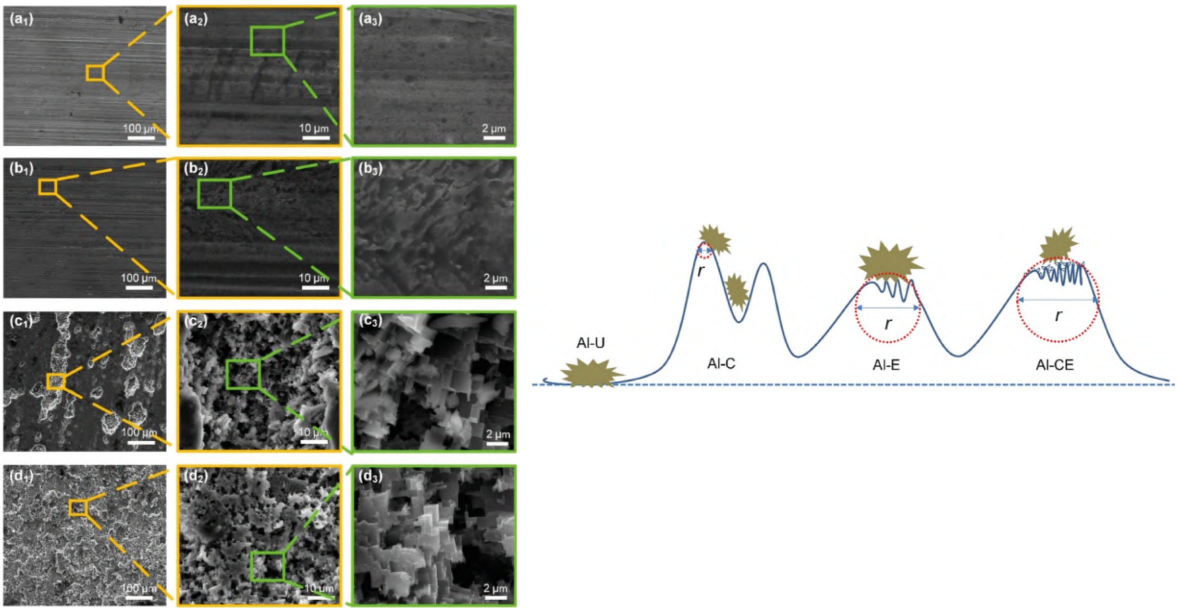

Figure 1.9: SEM images of the surface morphology of (a) Al-U, (b) Al-C, (c) Al-E, and (d) Al-CE substrates (left) and schematic diagram of particles making contact with microstructures on aluminium surfaces (right) [54].

Surface energy

Another approach to passive dust mitigation involves modifying the surface energy of materials to reduce dust adhesion. By lowering the surface energy, the interaction between the surface and dust particles is minimized, making it easier for particles to detach.

Dove et al. (2010) [15] investigated ion beam processing as a technique to modify the surface characteristics of black Kapton, silicon, and quartz. The process begins with an ion source, where precursor gases generate ions that are then extracted and accelerated to high energies using an electric field. The focused ion beam is directed at the surface to modify its properties without causing material growth or removal. Experimental results in a vacuum environment demonstrated that the ion beam treatment significantly reduced adhesion forces on the treated materials. For silicon and quartz, this reduction was attributed to a decrease in van der Waals forces resulting from lowered surface energy. In the case of black Kapton, the primary mechanism for reduced dust adhesion was the diminished electrostatic forces, caused by reduced contact charging.

To evaluate the effectiveness of the treatment, lunar dust simulant was deposited on both untreated and treated surfaces, and the samples were spun in a centrifuge to measure the force required for dust removal. The treated samples consistently shed dust at lower forces compared to the untreated surfaces. SEM images, such as the one shown in Figure 1.10, were taken at various spin increments to quantify the remaining dust coverage.

Additionally, the study examined how ultraviolet radiation affected dust adhesion on these materials. Both untreated and treated quartz surfaces exhibited increased adhesion after UV exposure, suggesting that surface treatments interact with environmental factors in space, and further investigation is required to optimize long-term performance in lunar conditions.

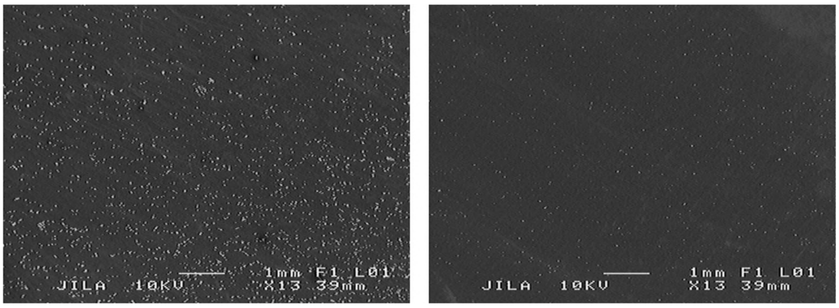

Figure 1.10: Sample SEM images showing dust deposition on black Kapton surfaces before (left) and after (right) applying centrifugal force [15].

Another effective method for reducing dust adhesion is the use of low-surface-energy coatings. Yang et al. (2022) [58] applied plasma-enhanced chemical vapor deposition to create a perfluorocarbon (PFC) film on glass substrates, achieving a hydrophobic surface treatment.

The water contact angle of a surface serves as an indirect measure of its surface energy. A higher contact angle corresponds to lower surface energy. Figure 1.11 compares the water contact angle of untreated glass with that of the PFC-coated surface. The coated surface exhibited a higher contact angle, nearly reaching 120°, indicating lower surface energy and improved hydrophobicity. The efficacy of the PFC coating was further confirmed by dust removal tests using Martian dust simulants. The coated surface significantly outperformed bare glass, proving that low-surface-energy films effectively decrease adhesion forces, thereby reducing dust accumulation.

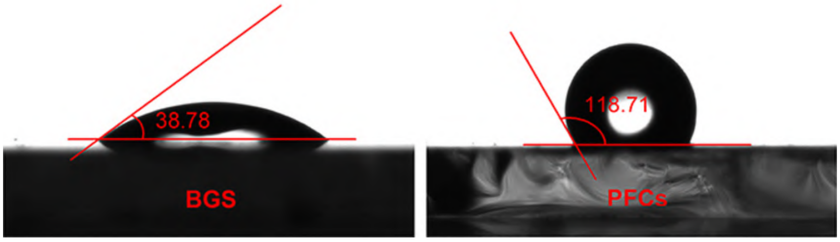

Figure 1.11: Water contact angles of samples before surface treatment (left) and after surface treatment (right) [58].

Work function

Another approach to dust-resistant coatings involves minimizing triboelectric charging, which occurs when different materials come into contact and exchange charge. The key idea behind this method is to apply a coating with a work function that closely matches that of lunar dust, thereby reducing the charge transfer between the surface and the dust particles. In theory, the ideal coating would be one made directly from lunar regolith, as it would have an almost identical work function to the dust itself. This principle led to the development of NASA's work function matching coating, which aims to minimize tribo-charging effects [19].

Films with a thickness of a few tens of nm were used to coat different substrates. The coatings were deposited using ion beam sputter deposition, where an argon ion beam was used to sputter a target made from a slurry of lunar simulant NU-LHT-1D. This technique allowed for the controlled deposition of a regolith-like thin film, maintaining the same work function properties as lunar dust. The experimental results showed that the coated samples retained significantly less dust than the untreated samples in almost all cases. However, one exception was found: the regolith film did not significantly improve dust removal on AZ93 white paint. This was attributed to the chemical composition of the paint, which contains metal oxide pigments embedded in a silicate binder. Since silicates already share chemical similarities with lunar regolith, the paint's inherent surface chemistry already minimized tribo-charging, making additional coatings redundant.

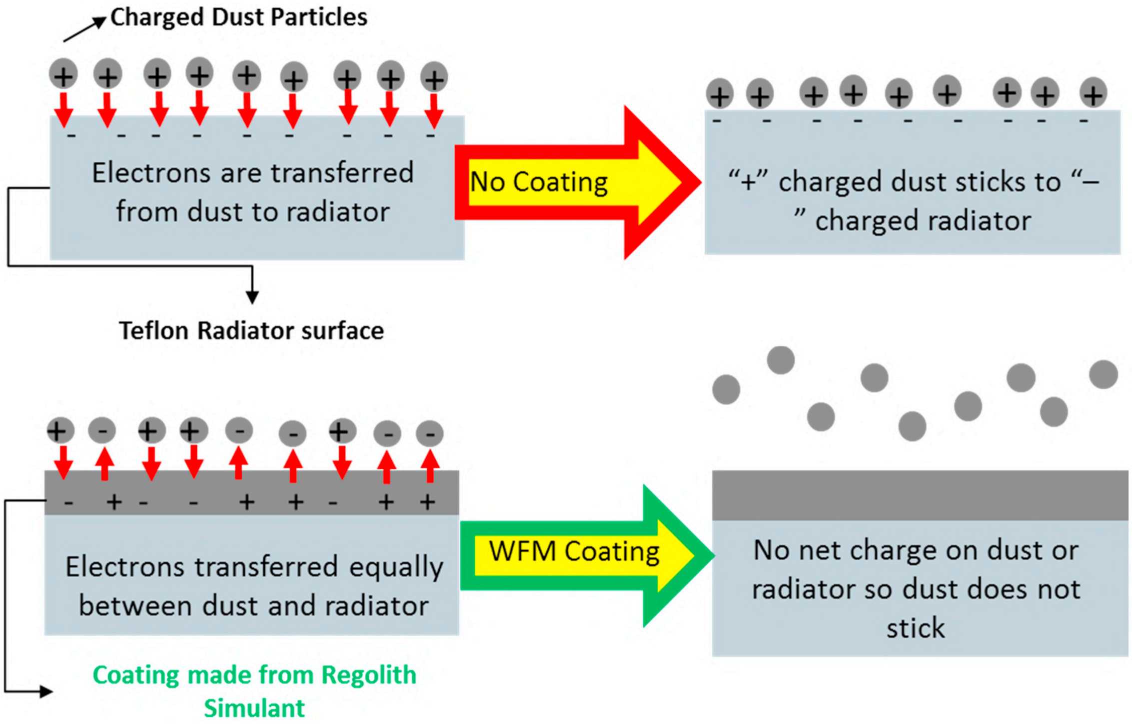

Figure 1.12: Work function matching (WFM) coating concept. ([19])

In a later study on dust mitigation technologies for spacesuits, work function matching coatings were combined with Electrodynamic Dust Shield (EDS) active technology to enhance dust resistance on spacesuit outer layers [37]. The combination of these two methods allowed for a dual-action approach. The work function matching coating minimized triboelectric charge buildup, reducing initial dust adhesion. and the EDS applied electric fields to actively remove any remaining dust. The results confirmed that spacesuit materials coated with the regolith-based thin film exhibited fewer adhered dust particles compared to untreated materials.

1.5. Problem Statement

The primary goal of this research was then to develop a coating with antidust properties suitable for the lunar environment, capable of repelling lunar dust and reducing its accumulation. Given that lunar regolith naturally charges due to interactions with the solar wind and UV radiation, one of the concepts was to create a coating that charges in a similar manner, enabling it to repel incoming dust particles through electrostatic repulsion.

To develop such a dust-repelling coating, a key requirement was that the material should be non-conductive, ensuring that it retains its electrostatic charge over time. A natural starting point was the composition of lunar dust itself, as mimicking its properties could allow for a similar charging mechanism to occur. Among its main constituents, alumina (Al_2O_3) emerged as a promising candidate due to its dielectric nature and wide commercial availability, making it an accessible and practical choice for coating fabrication.

Research into alumina-based coatings led to the work of Bonderer et al. (2009) [7], who developed a layer-by-layer (LBL) coating incorporating alumina platelets in a polyimide matrix. This type of LBL architecture seemed highly relevant in the lunar context, as none of the previously mentioned approaches considered the erosion effects that might occur on the Moon. Nanoroughness, low surface energy coatings, and work function-matching coatings may all contribute to reducing dust adhesion, but their efficacy is expected to decline significantly if the coating is eroded. In contrast, the LBL structure offers a potential advantage, as its layered design could provide self-renewing properties, helping maintain antidust performance even in harsh lunar conditions.

Polyimide is an ideal polymer choice for the layer-by-layer coating method due to its non-conductive nature, high-temperature resistance, and excellent radiation stability. Fully imidized aromatic thermoplastic polyimides are linear polymers that exhibit exceptional thermomechanical performance, making them suitable for high-temperature applications exceeding 230°C while maintaining their structural integrity. These properties are particularly advantageous for lunar applications, where extreme temperature fluctuations occur [12]. One of the most well-known polyimides, Kapton-H, has been extensively used in spacecraft thermal management systems due to its ability to withstand extreme temperature variations, ranging from 4 K to 673 K, without significant degradation. Its radiation resistance makes it highly suitable for space environments, where exposure to UV radiation, cosmic rays, and solar wind can cause polymer degradation [47].

By integrating this layer-by-layer architecture, the hypothesis was that the resulting coating would withstand the lunar conditions while providing the antidust performance. From this foundation, the central research question emerged:

“Can a layer-by-layer coating composed of polyimide and alumina platelets be developed with effective antidust properties for lunar applications?”

To address this question, the study was guided by the following subquestions:

- How can we measure dust adhesion on the coating?
- How does dust adhesion change under different testing conditions?
- How can we measure the material properties that influence dust adhesion?
- How does the layer-by-layer system affect coating durability?
- How does the lunar environment affect the coating’s antidust performance?

These questions framed the experimental approach, ensuring that both fundamental material properties and lunar-relevant conditions were systematically investigated throughout the study.

2

Coating manufacturing and characterization

This chapter outlines the materials and processes used to manufacture the polyimide/alumina platelets coating and the characterization methods implemented to evaluate the coating as well as other relevant surfaces. A comprehensive analysis of surface properties, including morphology, roughness and composition is presented to establish a foundation for understanding the coating's performance. The results obtained in this chapter will play a crucial role in the discussion of antidust performance in the following chapter.

2.1. Materials

2.1.1. Substrates

In a proof-of-concept study such as this one, we found it important to test a diverse range of materials. To this end, three types of bare substrates were selected: a metal, a polymer, and a ceramic. Aluminium 1060, a commonly used high purity aluminium alloy, was chosen for its relevance in aerospace applications. Polyether ether ketone (PEEK), a high-performance semicrystalline thermoplastic, often used for its favorable thermal properties and compatibility with ultra-high vacuum was acquired from Goodfellow. Zirconium diboride (ZrB_2), a ceramic known for its exceptional hardness and thermal stability, was kindly provided by Dr. Yinglu Tang from the Faculty of Aerospace Engineering at TU Delft.

2.1.2. Coating

Polyamic acid (PAA) (15.0-16.0 wt.% in NMP, used as polyimide precursor), alumina platelets in powder form (RonaFlair®White Sapphire, median diameter 10 μm, median width 0.5 μm), (3-Aminopropyl)triethoxysilane (APTES), 1-methyl-2-pyrrolidinone (NMP,99.5%,), iodomethane (containing copper as stabilizer, ReagentPlus®, 99%) and the solvents ethanol, methanol and acetone (analytical grade) were purchased from Sigma-Aldrich.

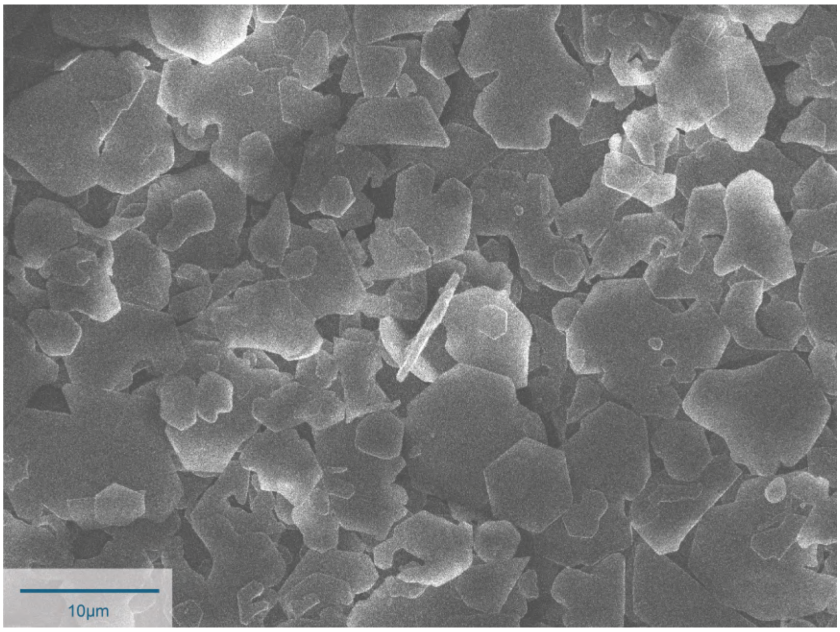

Figure 2.1: SEM image of RonaFlair®White Sapphire alumina platelets. Magnification:2000x.

2.1.3. Lunar dust simulant

As lunar soil samples are not readily available, lunar mare simulant 1 (LMS-1) was acquired from Exolith Lab. The high fidelity of LMS-1 as a lunar mare regolith simulant makes it well-suited for use in this thesis. As demonstrated by Long-Fox et al. (2023) [35], LMS-1 closely matches the properties of mare regolith in terms of composition and mechanical behavior, providing a reliable analog for lunar surface conditions. The chemical composition of LMS-1, as provided in the specification sheet of Exolith Lab, can be seen in Table 2.1 and in Figure 2.2 the SEM picture of the simulant illustrates the size range of the particles of <0.04 µm – 1000 µm with a median size of 60 µm.

Table 2.1: Chemical composition of LMS-1 shown in abundance of oxides as lithology signature [17].

Compound	Formula	Concentration (%)
Silica	SiO_2	48.22
Alumina	Al_2O_3	12.40
Lime	CaO	7.65
Iron (II) Oxide	FeO	8.79
Magnesia	MgO	15.97
Titanium Dioxide	TiO_2	2.70
Sodium Oxide	Na_2O	1.73

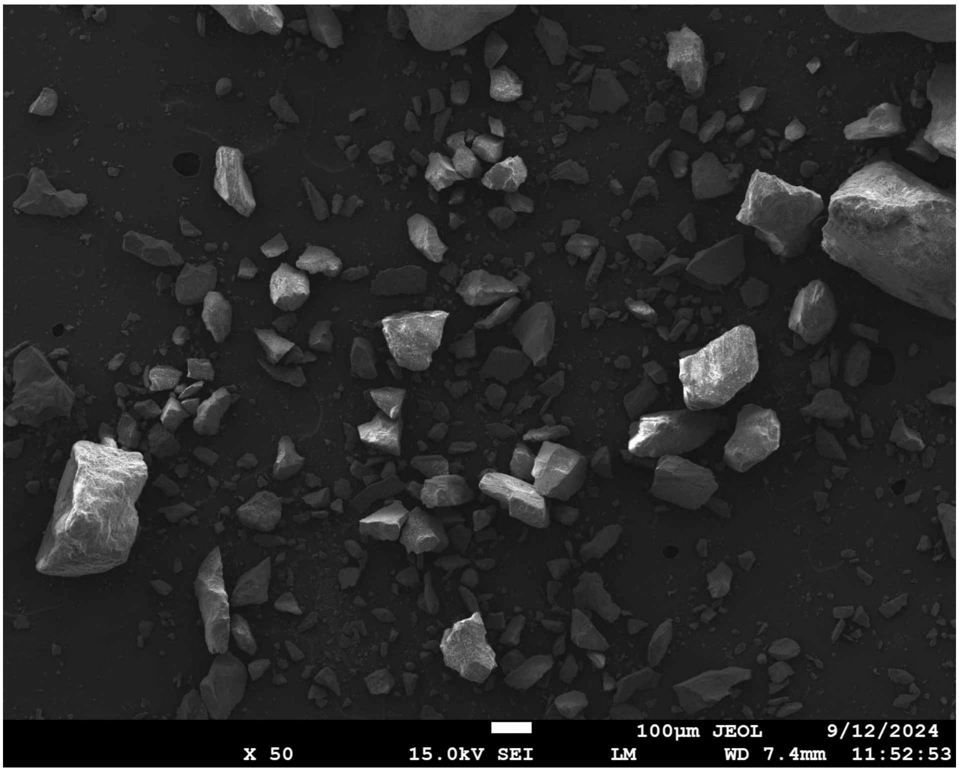

Figure 2.2: SEM image of LMS-1 particles.

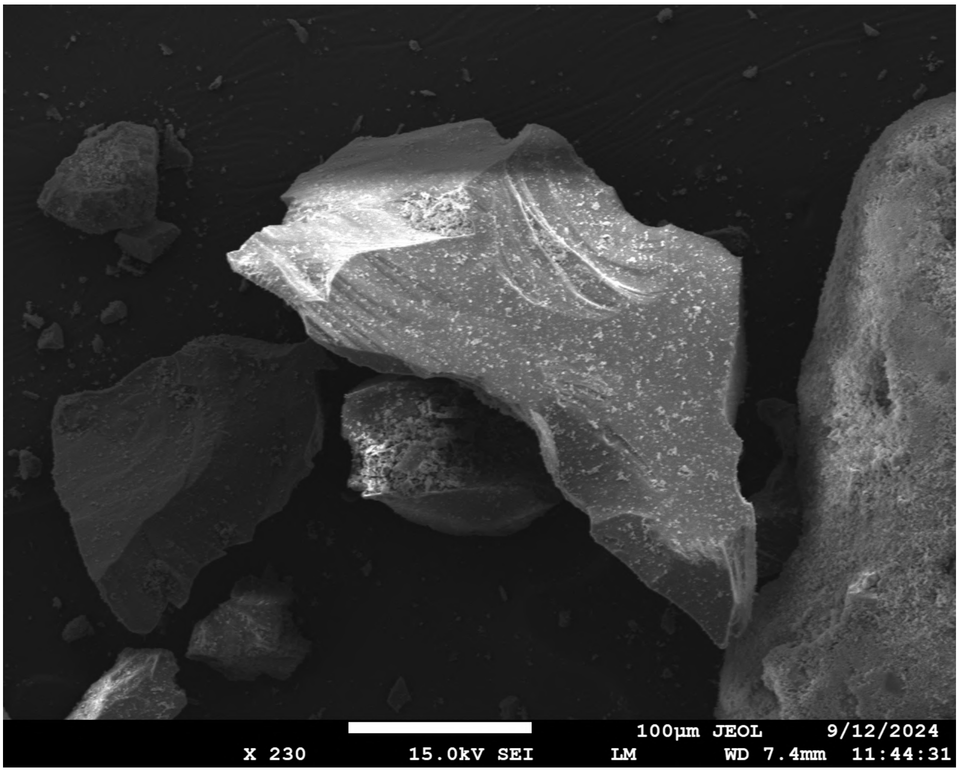

Figure 2.3: Zoomed in SEM image of a LMS-1 particle.

2.2. Sample preparation

2.2.1. Silanization

Silanization of alumina platelets was conducted to enhance compatibility between the platelets and the polyimide matrix, in order to reduce the formation of interfacial defects. The amine-terminated silane coupling agent (3-aminopropyl)triethoxysilane promotes the interaction between alumina and polyimide (PI). For triethoxysilanes such as this one, covalent bonding occurs through the hydrolysis of the Si-OR groups forming silanol groups(Si-OH) and ethanol (C_2H_5OH) as by-product. The Si-OH groups interact with the inherent surface hydroxyl groups on the alumina through a condensation reaction. These reactions can be seen in Figure 2.4.

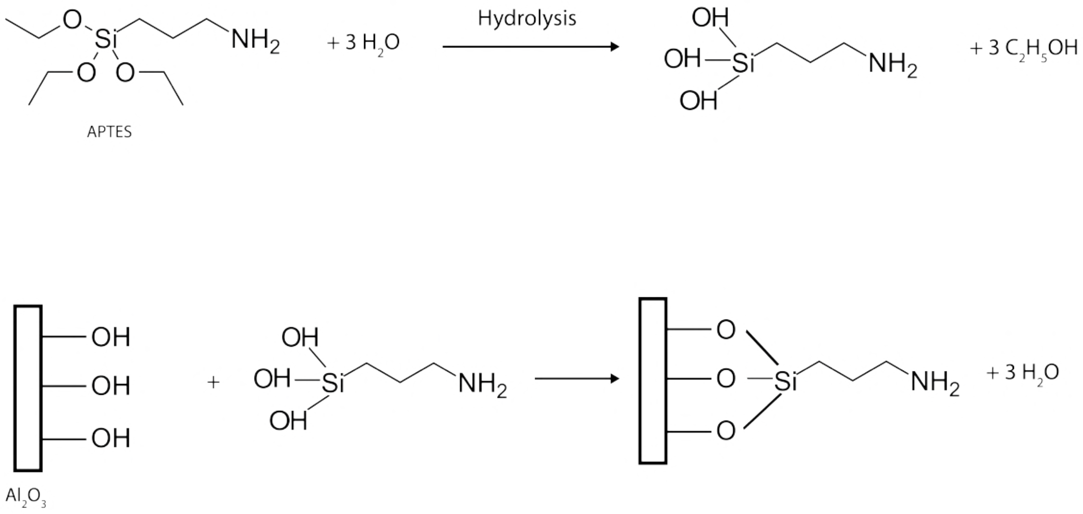

Figure 2.4: Schematic illustration of APTES hydrolysis and subsequent surface grafting on alumina.

The procedure was as follows, using the work of Bonderer et al. (2019)[7] as a base:

1. In a fume hood, in a beaker, measure 100 mL of a 3:1 volume-to-volume mixture of distilled water and methanol.
2. Add 10 mL of APTES to the solvent mixture.
3. Place the beaker on a magnetic stirrer and allow the mixture to hydrolyze for 1 hour.
4. Weigh 4 g of platelets and add them to the hydrolyzed APTES solution.
5. Stir and hold the suspension overnight at room temperature, to ensure sufficient interaction between the platelets and the APTES.
6. Transfer the suspension to a filtration setup to separate the silanized platelets from the liquid.
7. Wash the platelets 5 times with methanol, to remove any residual APTES or unreacted components.

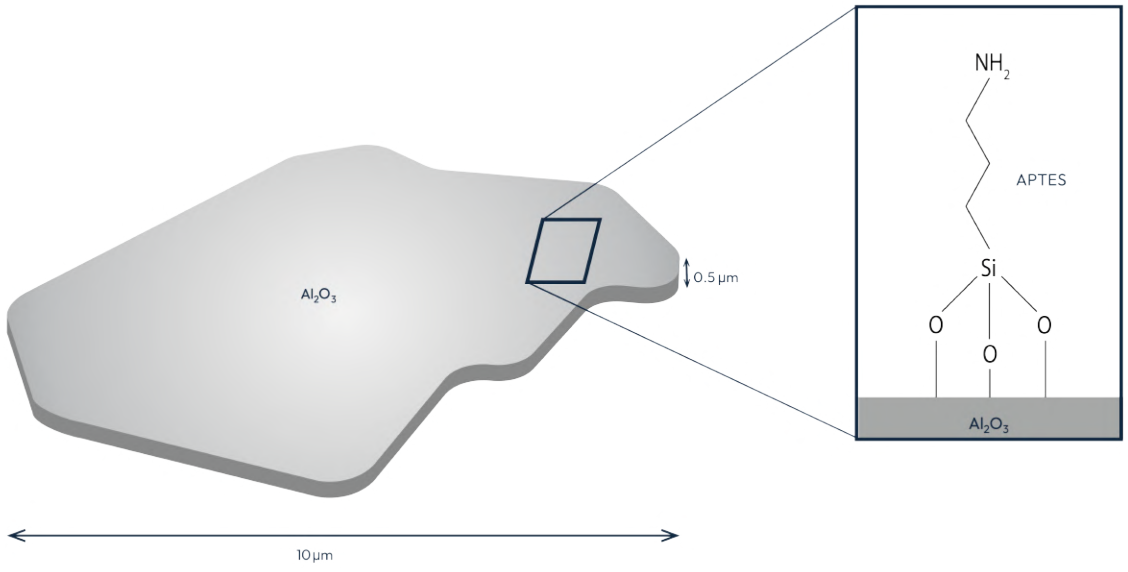

Figure 2.5: Representative diagram of a silanized alumina platelet.

The silanized platelets in Figure 2.5 are now prepared to interact with the polyamic acid during the manufacturing of the coating. The specific polyamic acid used, seen in Figure 2.6 was prepared by polymerization of pyromellitic dianhydride (PMDA) with 4,4-diaminodiphenyl ether (ODA). The amine group of the silane coupling agent can react with the carboxylic acid group in the polyamic acid in a condensation reaction forming an amide bond, as illustrated in Figure 2.7.

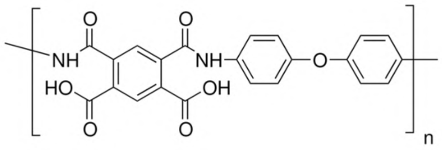

Figure 2.6: Schematic illustration of the polyamic acid.

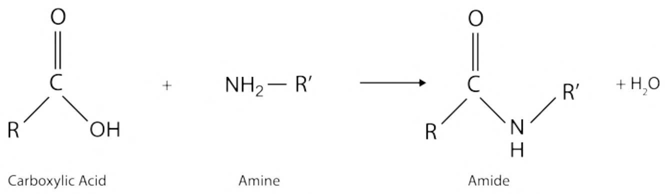

Figure 2.7: Amide bond formation between the silanized alumina platelets and the polyamic acid.

2.2.2. Layer by layer

Coating with alumina platelets

The coating was constructed using a layer-by-layer deposition method, as described by Bonderer et al. (2009)[7]. This technique alternates between depositing polymer and inorganic layers. As a substrate, aluminium 1060 was used. The metal was cut in 20x20mm squares and cleaned with acetone.

Preparation of polyimide layers:

1. Dilute 15 wt% stock solution of polyamic acid with NMP to change the polymer concentration to 10 wt% in NMP.

2. Spin 0.3 mL of polyamic acid solution at 1000 rpm for 15s, followed by a 15s rest before spinning the coated substrate again at 3000 rpm for 40s.
3. Soft bake on a hot plate at 120° C for 60s for solvent removal, hydrogen bonded to the PAA as seen in Figure 2.8.

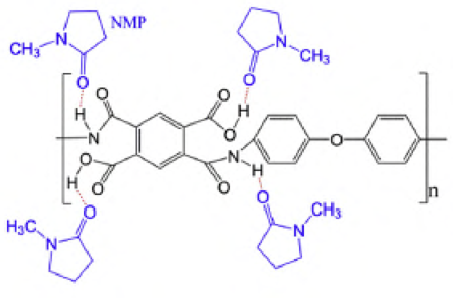

Figure 2.8: Schematic illustration of the NMP molecules H-bonded to the amide moiety and to the carboxylic acid of the PAA. [10]

Preparation of alumina platelet layers:

1. Slowly drop an ethanol solution with 1 wt% surface-modified platelets onto a 250ml beaker (6.8 cm diameter) completely filled with water, until complete coverage of the water surface (approximately 0.4 ml). Due to the high aspect-ratio of the alumina platelets, these naturally align at the water-ethanol interface due to surface tension effects.
2. Sonicate the beaker for 25 min. The effect of this sonication can be clearly seen in Figure 2.9.
3. Transfer the platelet layers to the aluminium substrate by manual dipping.
4. Dry in the oven at 50° C for 30 min.

As seen in Figure 2.10, this process was repeated iteratively to build the desired multi-layer structure with alternating polyimide and alumina platelet layers.

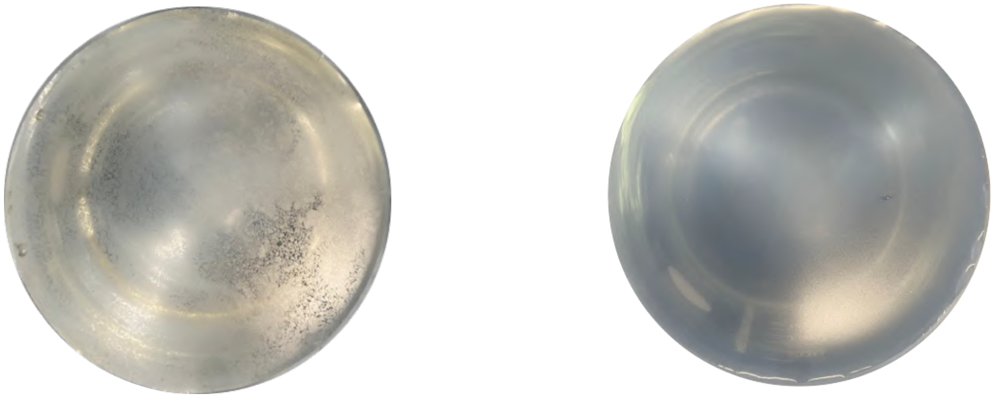

(a) Before.

(b) After.

Figure 2.9: Alumina platelet film before and after sonicating for 25 min.

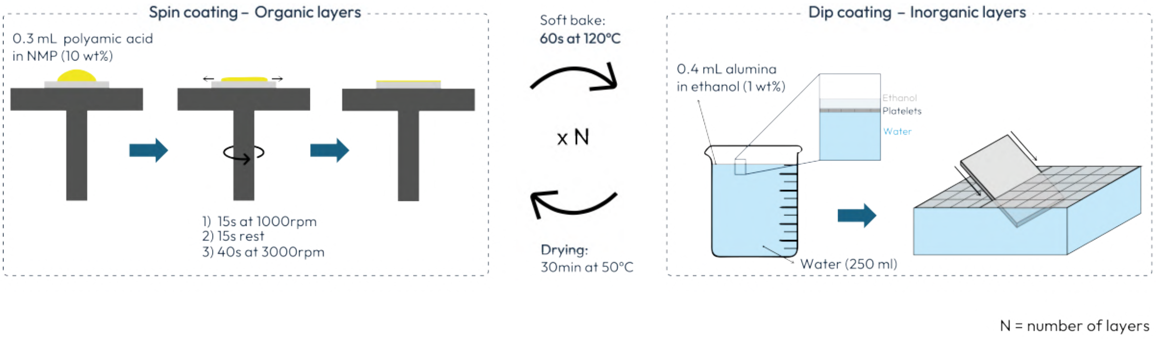

Figure 2.10: Illustrative diagram of the layer by layer method used. The coating always starts with a spin coating and ends with a dip coating.

Curing process

After deposition of all layers, the samples were dried in vacuum (1 mbar) at room temperature for 24 h in order to remove the water and solvent in the sample. The sample is then placed in the oven at a heating rate of 200ºC/h until 300ºC for 30 min to convert the polyamic acid to polyimide. During this curing process occurs thermal imidization, schematized in Figure 2.11, with the closing of the imide rings, to produce the aromatic polyimide. The cycle used can be seen in Figure 2.12.

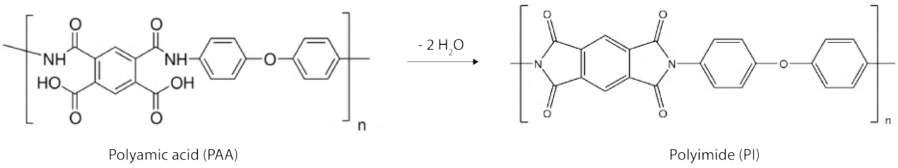

Figure 2.11: Imidization of the polyamic acid into polyimide.

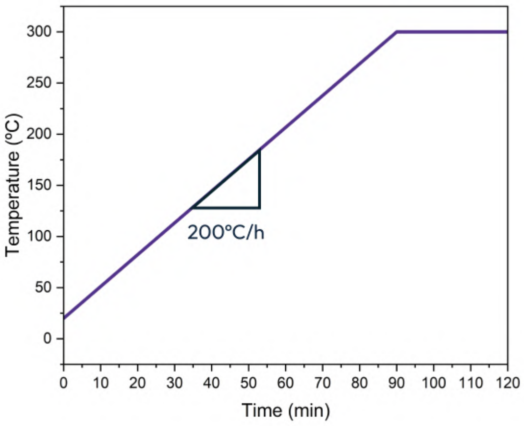

Figure 2.12: Curing cycle of the polyamic acid to polyimide at a rate of 200ºC/h until 300ºC and keeping at this temperature for 30min.

Coating with LMS-1 particles

In addition to the polyimide/alumina platelet coating, an alternative coating was fabricated by substituting alumina platelets with lunar simulant LMS-1 particles as the inorganic component. This approach aimed to open the topic of the feasibility of using regolith-based materials in coatings, aligning with ISRU principles.

However, modifications to the fabrication process were required due to the differences in morphology between alumina platelets and LMS-1 particles. The spherical and irregularly shaped LMS-1 particles did not exhibit self-alignment at the water-ethanol interface when the original layer-by-layer deposition method was applied. To address this issue, an adjusted deposition process was implemented. After each organic polyamic acid layer, a 0.5 mL suspension of sieved and silanized LMS-1 particles (less than 20 μm in size) in ethanol at 10 wt% concentration was spin-coated for 15 seconds at 500 rpm. Once all the wanted layers were deposited, following the layer-by-layer sequence illustrated in Figure 2.13, the samples underwent the same curing process as before.

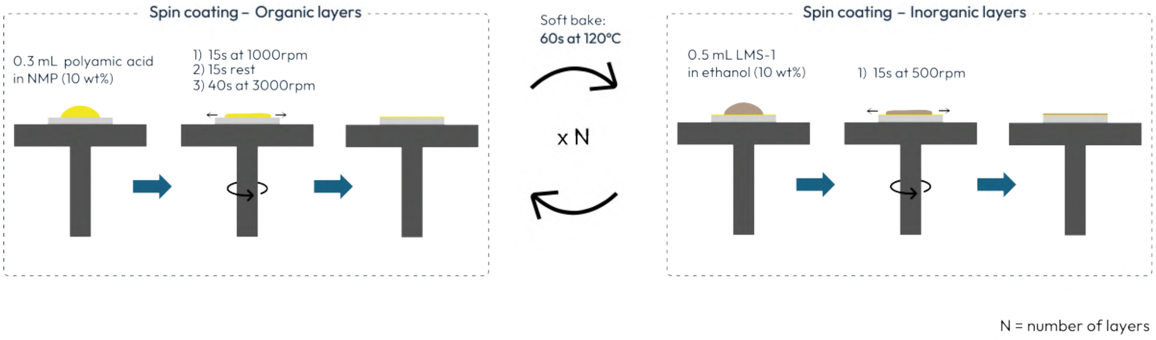

Figure 2.13: Illustrative diagram of the adapted layer by layer method used for the polyimide/LMS-1 particles coating.

2.3. Charged samples

Electrostatically charged samples are critical in demonstrating the coating's capability to repel lunar dust under the different electrical conditions present on both sides of the Moon. On the sunlit side, where the lunar surface is positively charged due to photoelectric effects from solar radiation, the coating must effectively repel positively charged dust particles. On the dark side, the surface becomes negatively charged as a result of interactions with the solar wind plasma. To simulate these conditions, positive charges on the samples were introduced chemically and negative charges physically.

2.3.1. Positive

The positively charged samples were prepared by further modifying the already silanized alumina platelets. As seen in Figure 2.14, the amino groups present in the amine-terminated APTES were alkylated to generate quaternary ammonium cations, following the methodology described by Bandl et al. (2024) [5]. These positively charged alumina platelets were then incorporated into the coating using the previously outlined layer-by-layer deposition method, as illustrated in Figure 2.15. The procedure is as follows:

1. In a beaker, immerse 2g of silanized alumina platelets in 15mL of methanol.
2. Slowly add 1.33mL of iodomethane dropwise to the beaker.
3. Allow the reaction to proceed for 6 hours at room temperature under continuous stirring

to ensure complete conversion of the amino groups to quaternary ammonium groups.

4. After the reaction is complete, remove the platelets to a filtration setup, wash thoroughly with methanol to remove any residual reactants, and dry at room temperature.

Figure 2.14: Schematic illustration of the quaternization of the silane coupling agent.

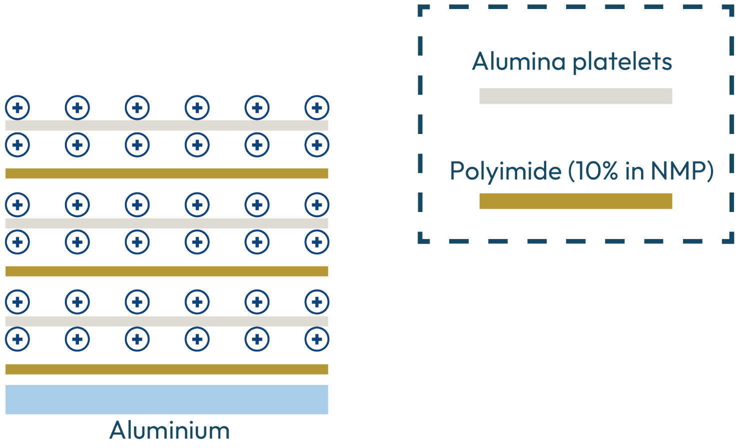

Figure 2.15: Illustrative diagram of the positively charged coating.

2.3.2. Negative

For the negatively charged samples, the coating was exposed to an electron beam inside a scanning electron microscope. This technique was used to charge the surface, taking advantage of the non-conductive nature of the coating to retain the negative charges, and therefore making use of what is, usually, an undesirable effect. The environment inside the miscroscope provided high-vacuum conditions at approximately 10^{-5} Pa, ensuring a controlled atmosphere for the charging process. The parameters employed were as follows: probe current of 150 nA, acceleration voltage of 15 kV, emission current of 20 μA, and a magnification of 40x.

As illustrated in Figure 2.16, the electron beam was focused on a specific area of the coating for 30 seconds before being moved systematically to the next section. As the sample becomes negatively charged, when the incident electrons reach it, the beam is then repelled by the sample, leading to a higher intensity of brightness on the screen, allowing to visualize the charged area of the sample. This process was repeated until the entire coating surface was charged. The final product is displayed in Figure 2.17.

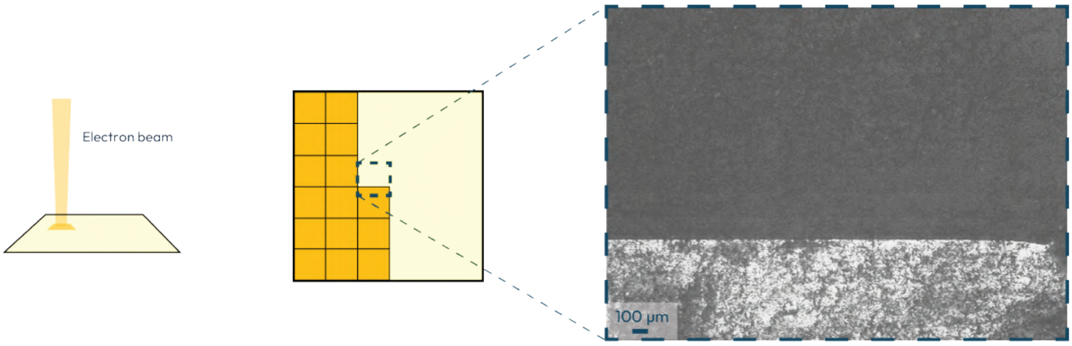

Figure 2.16: Schematic illustration of the negative charging of the surface of the coating using an electron beam. On the SEM picture on the right, we can clearly identify the already charged surface by its brighter colour.

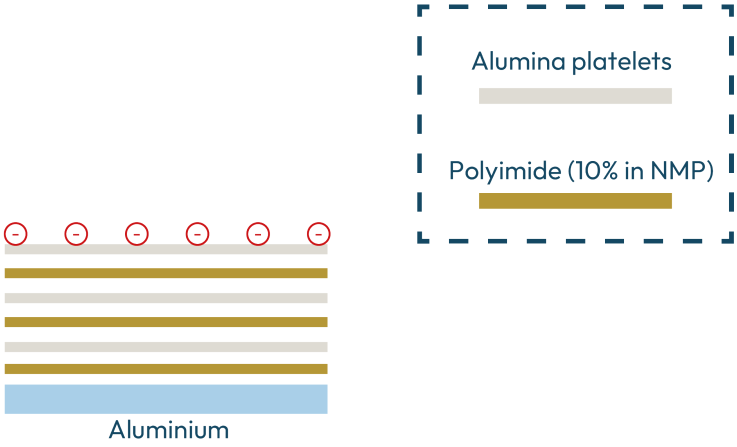

Figure 2.17: Illustrative diagram of the negatively charged coating.

2.4. Charged simulant

To obtain positively and negatively charged lunar dust simulant, we used the triboelectric effect, a phenomenon where charge transfer occurs during the dynamic contact of two materials. This effect, commonly observed in mechanical processes such as rolling, sliding, vibration, and impact, can result in significant electric potential differences. The approach was inspired by the work of Yeo et al. (2023) [23], who demonstrated that lunar dust could be charged through interaction with rover wheels made of different materials.

In this study, we aimed to reproduce the electrostatic properties of lunar dust as observed on the Moon by using two polymers positioned at opposite ends of the triboelectric series, as seen in Figure 2.18. Polyamide (PA), commonly known as Nylon, known for its position high on the series, was used to generate negative charges on the simulant, while polytetrafluoroethylene (PTFE), commonly known as Teflon, which is low on the series, was used to generate positive charges.

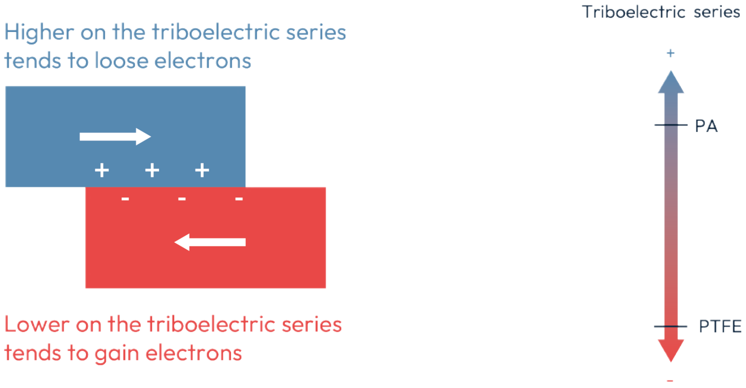

Figure 2.18: Illustrative diagram of the triboelectric charging effect (left) and position of the polymers used in the triboelectric series (right)

The charging process was straightforward, as described in Figure 2.19. The lunar dust simulant was placed inside bags made of either PA or PTFE, and the bags were vigorously shaken for 30 seconds to ensure sufficient dynamic contact. Once charged, the simulant was directly applied to the sample during the antidust performance tests.

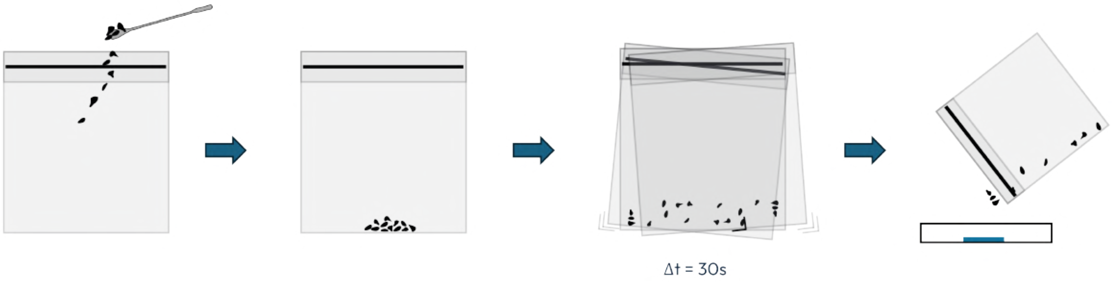

Figure 2.19: Illustrative diagram of charging of lunar dust simulant by triboelectric charging.

2.5. Coating characterization

To analyse the samples, different characterization techniques were used. This section describes how the Scanning Electron Microscopy (SEM), Fourier Transform Infrared spectroscopy (FTIR), contact angle (CA) measurements and microindentation testing were performed.

2.5.1. Coating imaging

Scanning Electron Microscopy (SEM), using a JSM-7500F Scanning Electron Microscope, was employed to observe the LMS-1 regolith simulant and, more critically, to examine the cross-section of the coating and verify its multi-layered composition. SEM is ideally suited for this purpose as it generates high-resolution images with a large depth of field, enabling detailed visualization of the topography of samples's cross-section.

SEM operates by directing a focused beam of electrons onto the surface of a sample. The interaction of the electron beam with the material generates various signals, such as secondary electrons, backscattered electrons, and X-rays, which can provide detailed information about the surface and subsurface properties. For imaging the cross-sections in this study, the primary focus was on detecting secondary electrons. These low-energy electrons are highly sensitive to surface topography and do not penetrate deeply, making them ideal for capturing the morphology of the coating's cross-section.

Sample Preparation

First, the samples were carefully cut to expose the cross-sections of interest. Multiple samples were then stacked together in a sample mold, followed by embedding them within the Technovit®4071 fast-curing, two-component methyl methacrylate resin to maintain their alignment and make further processing easier. Once the resin cured, the embedded samples were polished to expose the material of the specimen cross-sections and create a flat, consistent surface for the microscopes to focus on. The polishing process involved using progressively finer silicon carbide papers with grit sizes of #1000, #2000, and #4000. The force applied to the embedded samples was 25 N for 1 minute. This eliminates any potential scratches that could interfere with microscopy observations. A Tegramin-20 grinding and polishing machine was used for this step. Finally, the epoxy puck was sputter coated with a 15nm-thick gold layer, providing the conductivity and stability needed for high-quality imaging.

Layer by layer method

The layer-by-layer deposition method was employed to fabricate coatings with alternating layers of polyimide and alumina platelets. In this section, the results of studies aimed at optimizing the polymer layer thickness, analyzing the internal structure of the coatings, and investigating the effects of excess alumina platelets are presented.

Polymer layer thickness

To optimize the polymer layer thickness for the coating process, a study was conducted to investigate the effects of polyamic acid concentration in NMP (wt.%) and spin coating speeds. The polyamic acid concentrations used were **15%**, **10%**, and **5%** and the spin coating speeds tested were **4000 rpm**, **3000 rpm** and **2000 rpm**. Single layers of polyamic acid were spin-coated onto Aluminium 1060 samples, cured to polyimide and the resulting thicknesses were measured.

The average thicknesses obtained for each combination of parameters are presented in Table 2.2, while representative SEM images of the samples are shown in Figure 2.20. As expected, higher spin coating speeds produced thinner polymer layers due to increased centrifugal forces that spread the solution more thinly.

It is important to note that for the 5% polyamic acid concentration at 4000 rpm and 3000

Table 2.2: Polyimide layer thickness [µm] for different polyamic acid concentration in NMP and spin coating speeds.

		PAA concentration in NMP [wt. %]		
		15	10	5
Spin coating speed [rpm]	4000	6.55 ± 1.18	1.33 ± 0.16	-
	3000	7.93 ± 1.23	2.18 ± 0.03	-
	2000	12.57 ± 2.87	7.76 ± 2.51	1.68 ± 0.34

rpm, the speed was too high to allow the polyamic acid to adhere properly to the aluminium substrate, resulting in the absence of any detectable polyimide layer after curing.

The parameters chosen for the fabrication of all subsequent samples were 10% polyamic acid concentration and a spin speed of 3000 rpm. This combination resulted in the most homogeneous and consistent polymer layer across the sample, as confirmed by the SEM analysis. For higher concentrations at lower spin speeds (such as 15% at 2000 rpm), the polymer layer exhibited detachment from the substrate, making it unsuitable for the coating process.

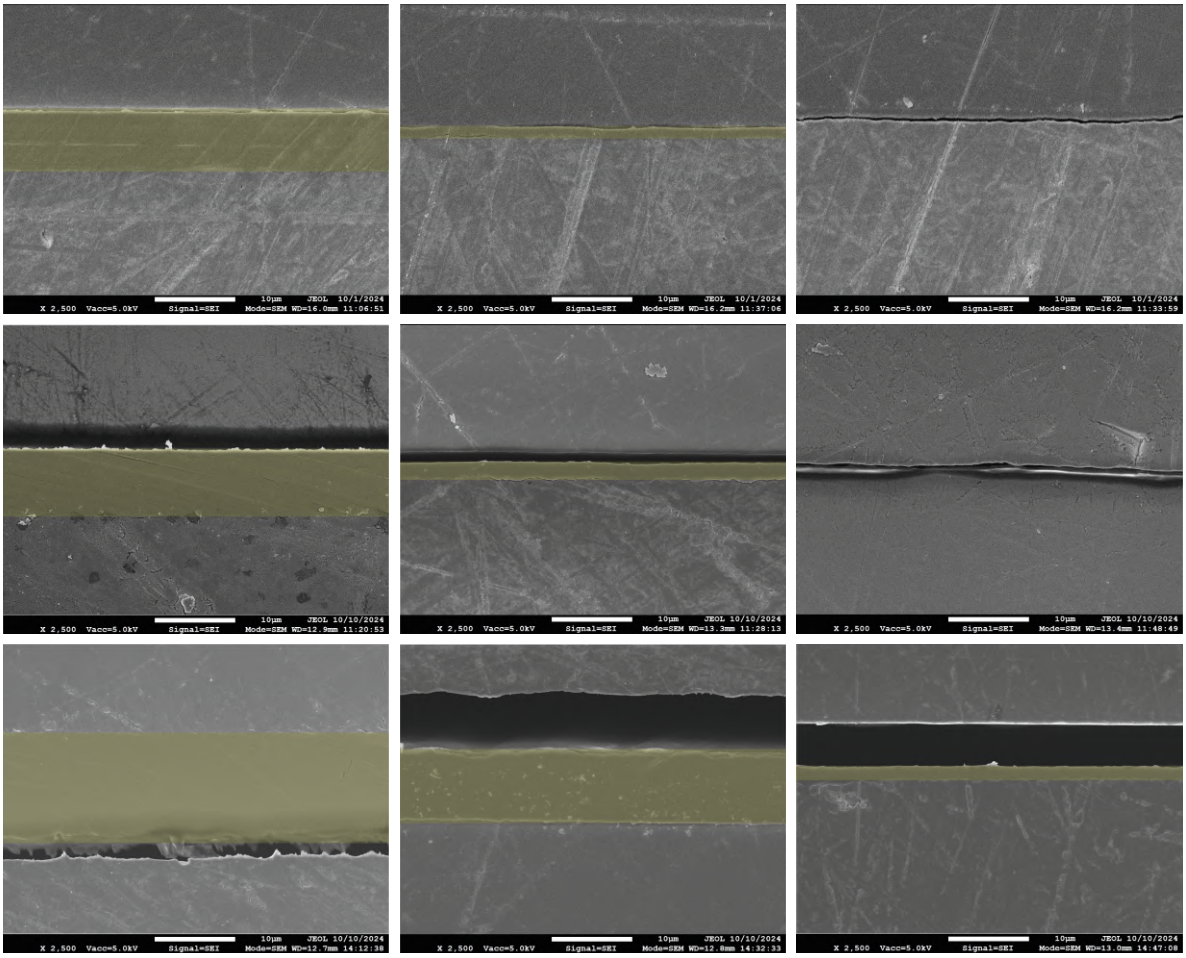

Figure 2.20: SEM pictures of a single layer of polyimide on an aluminium 1060 substrate at 15%, 10% and 5% (left to right) polyamic acid concentration in NMP and 4000rpm, 3000rpm and 2000rpm (top to bottom) spin coating speed. The PI layer is highlighted in yellow

Polyimide/alumina platelets coating

To check the structure of the coating, samples were fabricated using the layer-by-layer method, consisting of three layers of polyimide alternating with three layers of alumina platelets. The coated samples were then cross-sectioned and analyzed using SEM to visualize the architecture of the multilayer system.

The results, shown in Figure 2.21, reveal a distinct and well-organized structure, where the polymer and ceramic layers alternate as intended. The alumina platelet layers (lighter in colour) appear distributed in the polyimide in layers. This confirms the successful deposition of both materials. The cohesion between layers and lack of interfacial fractures between the platelets and the polymer further highlight the effectiveness of the silanization process in promoting adhesion during sample preparation and observation.

However it is possible to see that the first and second layers of polyimide are thinner (around 0.7 µm) than the 2.18 µm previously expected thickness. This may indicate that the spin-coating also affects the previously deposited organic layers, leading to thinner layers. The total coating thickness was calculated to be around 5µm across these three samples.

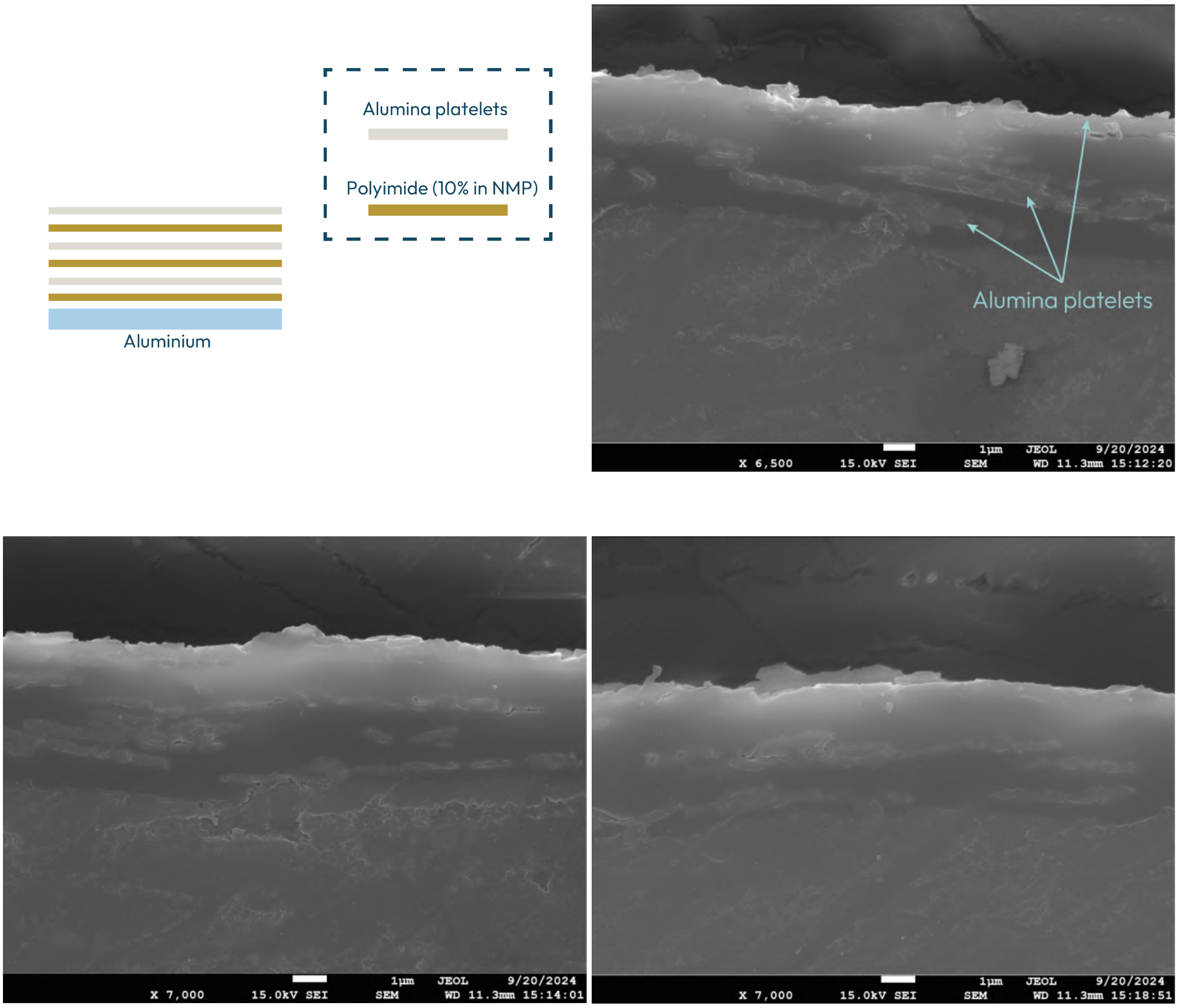

Figure 2.21: Diagram of the expected 3 layer coating (top left) and SEM pictures of the polyimide/alumina platelets coating.

Polyimide/LMS-1 particles coating

The same process as before was used to check the structure of the coating with LMS-1 particles. The cross-section of the coated samples was analyzed under SEM. The results are as seen in Figure 2.22.

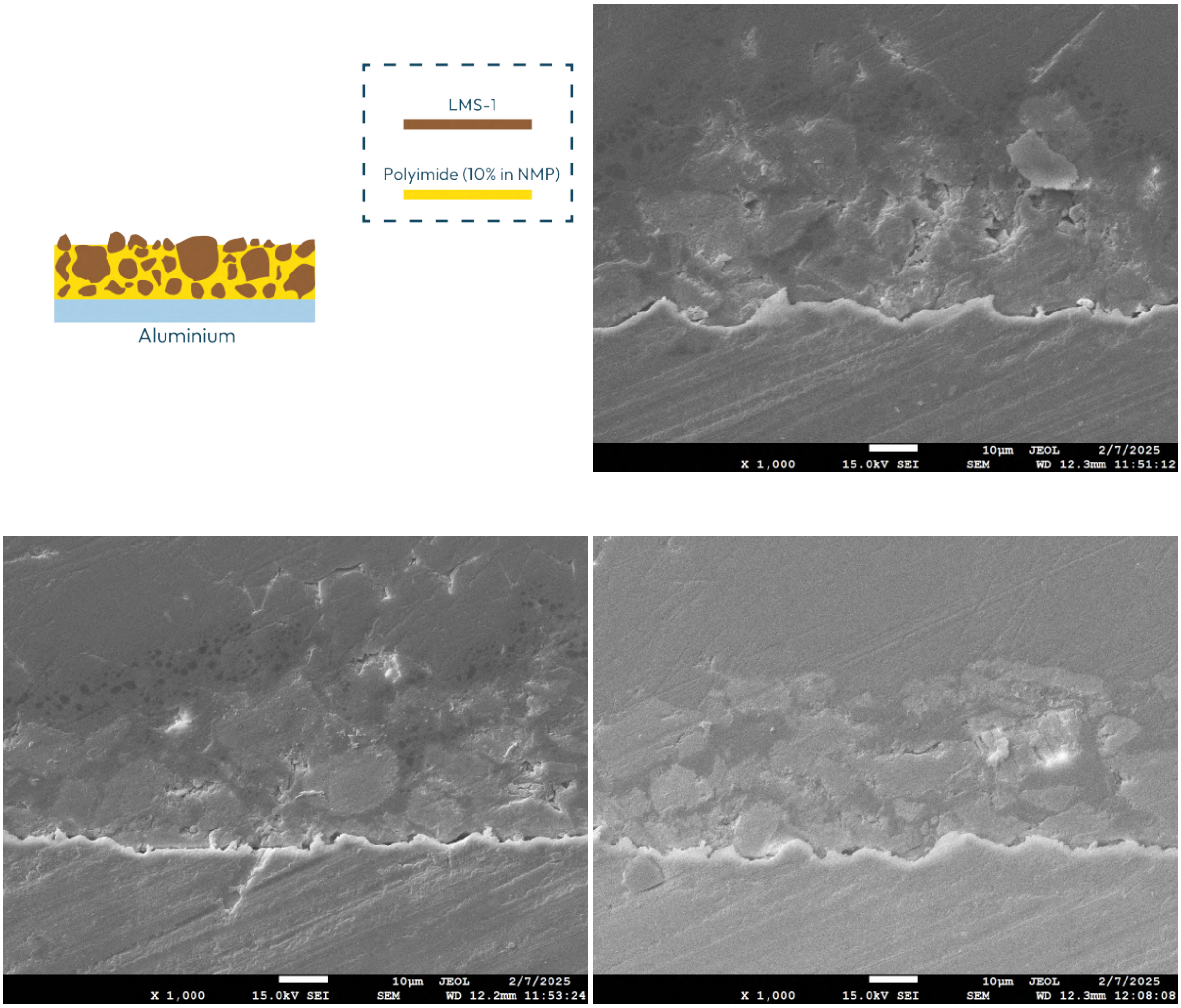

Figure 2.22: Diagram of the resulting coating (top left) and SEM pictures of the polyimide/LMS-1 particles coating.

SEM analysis of the polyimide/LMS-1 particle coating reveals a distinct structure compared to the polyimide/alumina platelet coating. Unlike the well-defined layer-by-layer architecture observed in the alumina-based coating, the LMS-1 coating lacks a clear stratified structure. Instead, the images show LMS-1 particles embedded within a polymeric matrix, with no obvious layering between the polyimide and the lunar simulant particles.

This absence of visible layers may be attributed to the interaction between the polyamic acid and the LMS-1 particles during deposition. Given that the spin-coated LMS-1 particles do not exhibit natural interfacial alignment, they likely sink into the previously deposited polyamic acid layer rather than forming a discrete layer on top. The heterogeneous size and shape of the LMS-1 particles further contribute to this behavior. Unlike the flat, platelet-like alumina, which forms a stacked layer, the irregular, rounded particles of LMS-1 create an uneven surface, allowing the polyamic acid to infiltrate and distribute between them rather than forming distinct layers. This hypothesis is supported by the total thickness of the coating, which averages 35 µm. Instead of stacking in an ordered manner, the LMS-1 particles become lodged within the surface roughness created by the previous deposition step, with the polyamic acid coating and surrounding the particles rather than forming structured layers. This significantly alters the final coating morphology, making it a continuous particle-polymer composite rather than a stratified material.

Another challenge in analyzing the coating cross-section is the difficulty in distinguishing the boundary between the coating and the epoxy mold. The porous nature of the LMS-1 particle coating likely allowed for epoxy infiltration during sample embedding, making it difficult to clearly identify where the coating ends and the epoxy begins in SEM images. EDS analysis (see Appendix D) also did not provide clear separation between the coating and the embedding resin, as the chemical elements of the polyimide overlap with those of the epoxy medium.

Comparing this coating to the polyimide/alumina platelet coating, another notable difference is the higher inorganic content in the LMS-1 composite. Since the LMS-1 particles are significantly larger than the alumina platelets, yet the same amount of polyamic acid was used in both coatings, the ratio of inorganic-to-organic content is much higher in the LMS-1 coating. This change in composition may have implications for the mechanical properties.

This modification demonstrates, however, the feasibility of incorporating regolith-based materials into protective coatings, potentially paving the way for locally sourced antidust solutions in future lunar missions. However, given the morphological and interfacial differences between alumina platelets and LMS-1 particles, further optimization is required to improve particle distribution and possibly mechanical properties.

Excess of alumina platelets

An interesting observation was made during the coating fabrication process regarding the behavior of the alumina platelets in the ethanol solution. When the platelets stayed in the alcohol solution for more than two days, there was a noticeable need to increase the volume of the solution added on top of the water during the dip coating process. This change is likely due to a loss of hydrophobicity in the platelets, attributed to the degradation of the silane coupling agent over time.

This issue led to the formation of heterogeneous films, as seen inFigure 2.23, where darker regions indicate the presence of multiple layer of alumina platelets on top of each other. The accumulation of excess platelets resulted in uneven coatings and poorer-quality specimens, as shown in Figure 2.24. The excess platelets contributed to increased brittleness in the coatings, which caused delamination at the second alumina platelet layer. To avoid this issue, it was necessary to prepare a fresh alumina platelet ethanol solution for each batch of samples.

Figure 2.23: Alumina platelet with excessive platelet number. Is is possible to see a heterogeneous film with darker portions that indicate multiple layers of platelets, like the one highlighted in red.

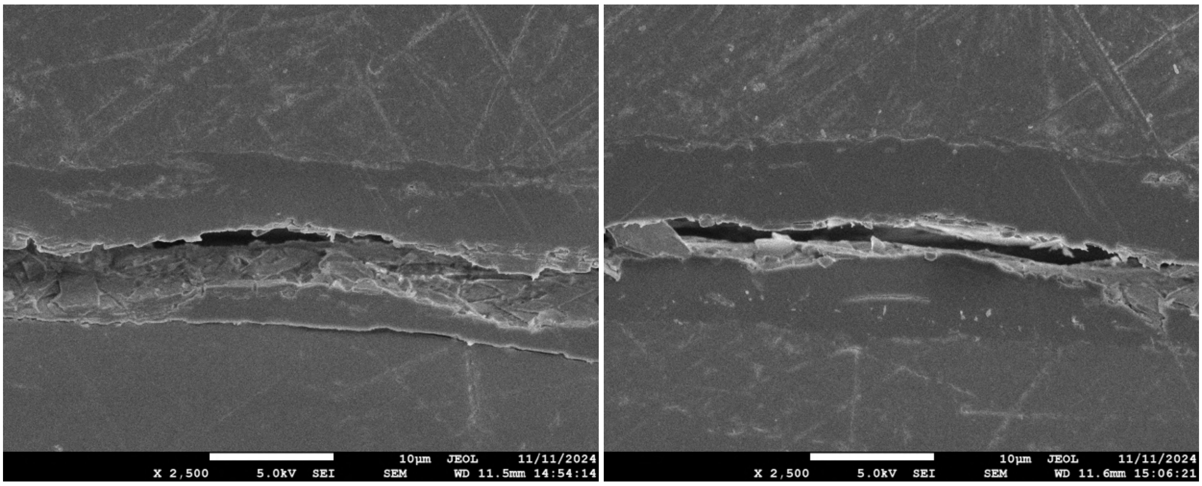

Figure 2.24: SEM picture of a 3 layer PI/alumina coating that peeled off on the second layer of alumina due to excess number of platelets.

2.5.2. Chemical characterization

Fourier Transform Infrared Spectroscopy (FTIR) is a powerful analytical technique used to determine the chemical composition of various materials. FTIR works by exposing a material to infrared light and measuring the light that is absorbed or transmitted, since specific IR wavelengths are absorbed by the sample, depending on the nature of its bonds and molecular composition. The resulting spectrum serves as a ”molecular fingerprint,” identifying the chemical bonds present within the material. A Spectrum 100 FTIR spectrometer (Perkin Elmer) was used. The spectrum produced ranges from 4000 to 600 cm^{-1} at 32 scans.

The technique was used to confirm two key processes. First, to verify the successful curing of polyamic acid into polyimide. The imidization process involves the chemical transformation of polyamic acid into polyimide through high-temperature curing, resulting in characteristic FTIR peaks that distinguish the fully cured material. After spin coating with a layer of polyamic acid and subsequent drying in vacuum for 24 hours, the sample was analysed using FTIR. The spectrum of the same sample after curing was there compared to the one before.

Second, FTIR was employed to confirm the silanization of alumina platelets. The silanization process introduces functional groups onto the platelet surfaces, that react with the polymer. The spectra of a coating manufactured with non silanized alumina platelets and of one with silanized ones was used to check for any identifiable differences.

Polyamic acid curing

To verify the successful conversion of polyamic acid into polyimide, seen in Figure 2.25, the spectra of the polyamic acid before and after curing were compared.

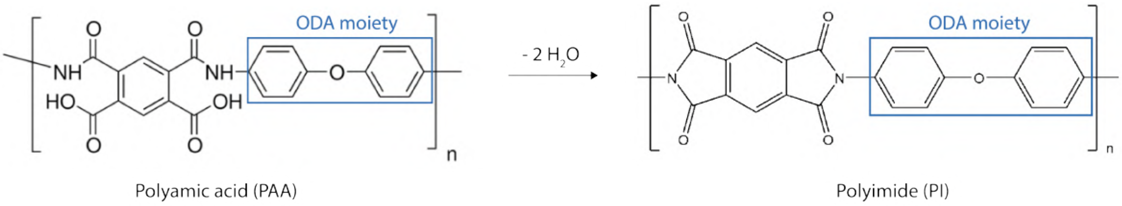

Figure 2.25: Schematic illustration of the imidization of PAA into PI.

The FTIR spectrum of the polyamic acid is presented in Figure 2.26, with key peaks summarized in Table 2.3.

Upon curing, the IR transmission spectrum changed as shown in Figure 2.27. These changes align with previously reported data in the literature [38], confirming the expected chemical transformations. In the polyamic acid spectrum, characteristic peaks at 1650 cm^{-1}, 1601 cm^{-1}, and 1408 cm^{-1} corresponding to amide and carboxylic acid bonds were observed. After curing, these peaks disappeared, indicating the elimination of these during the imidization process.

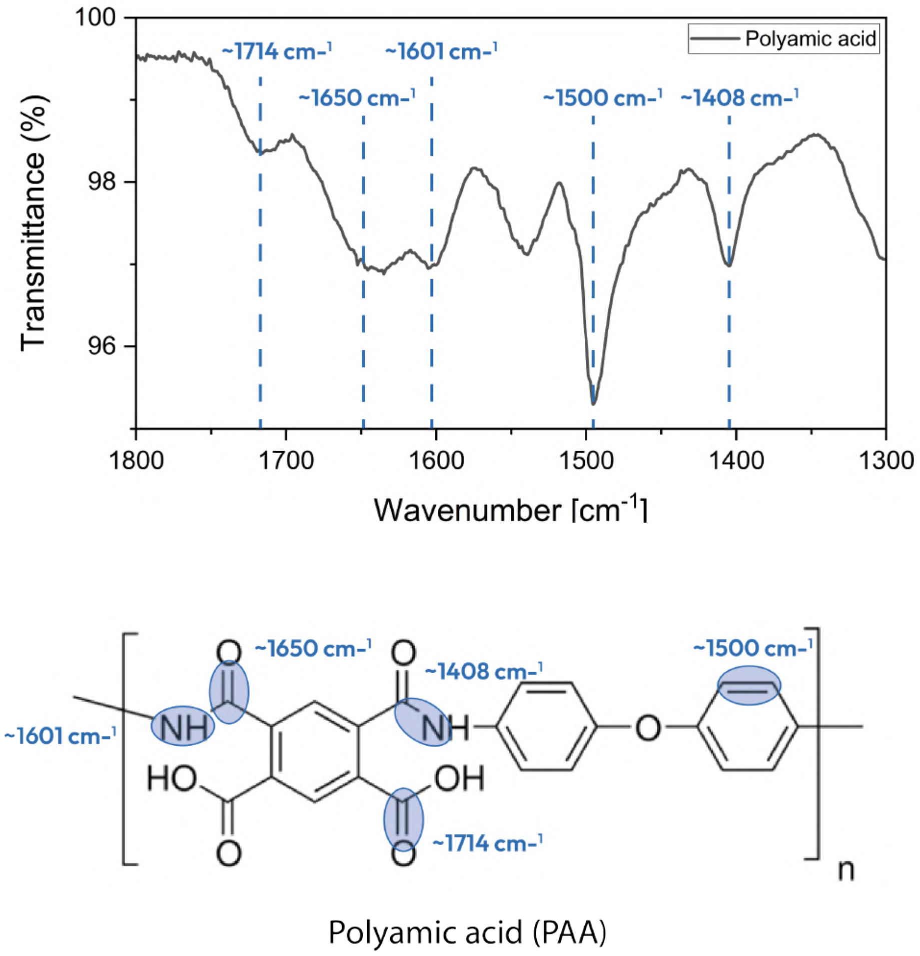

Figure 2.26: FTIR spectrum of polyamic acid and corresponding chemical bonds.

Table 2.3: FTIR transmittance peaks and their corresponding assignments for polyamic acid. [46]

Wavenumber [cm^{-1}]	Assignment
1714	Carboxyl C=O
1650	Amide C=O
1601	Secondary amine N-H
1500	Aromatic C—C stretching
1408	Secondary amine C-N

Simultaneously, new peaks emerged at 1774 cm^{-1} and 1710 cm^{-1}, attributed to the C=O stretching modes of the imide ring. Another prominent peak appeared at 1362 cm^{-1}, corresponding to the C–N stretching of the imide. These spectral features confirm the closure of the imide ring and the successful formation of the polyimide structure.

Additionally, the peak at 1500 cm, associated with the aromatic C=C stretching mode of the oxydianiline (ODA) moiety, was retained in both spectra.

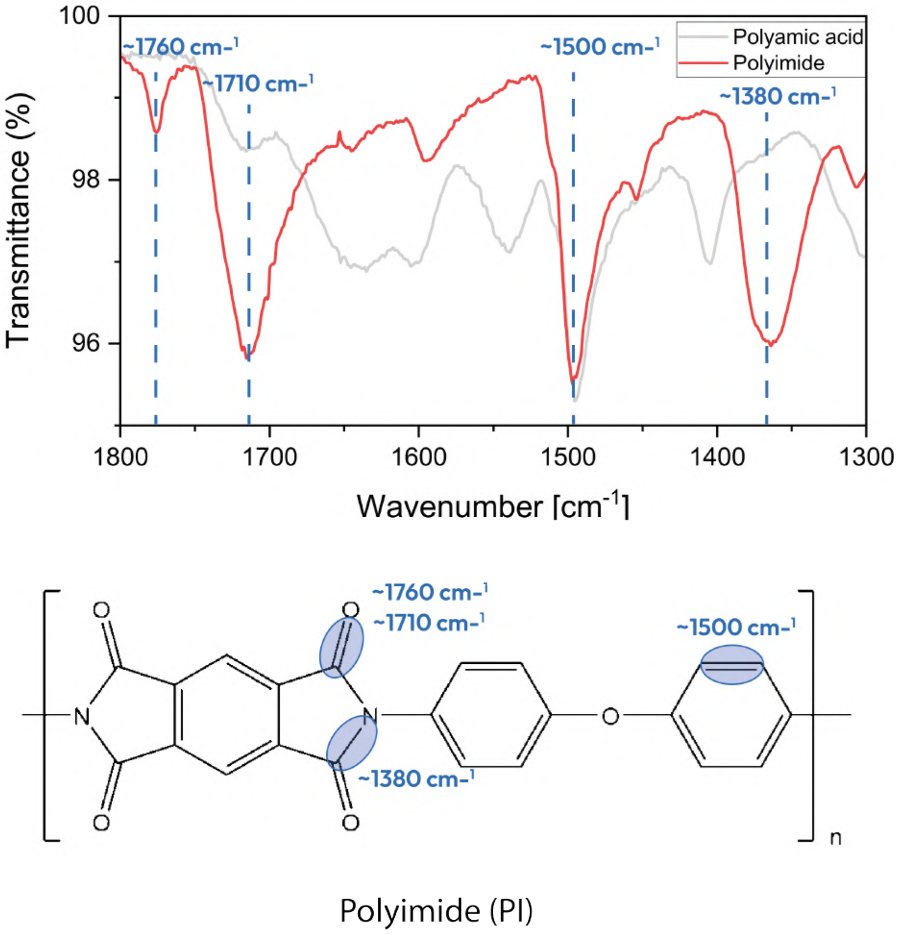

Figure 2.27: FTIR spectrum of polyimide using polyamic acid as the precursor and corresponding chemical bonds.

Table 2.4: FTIR transmittance peaks and their corresponding assignments for polyimide [38].

Wavenumber [cm^{-1}]	**Assignment**
1760	Aromatic Imide C=O
1710	Asymmetrical C=O stretching
1500	Aromatic C—C stretching
1380	Aromatic imide C—N stretching

Silanization of alumina platelets

The amine group of the silane coupling agent (APTES) reacts with the carboxylic acid group in the polyamic acid through a condensation reaction, forming amide bonds that chemically bond the alumina platelets to the polymer matrix.

To confirm the formation of amide bonds between the alumina platelets and the polymer, the FTIR spectra of three samples were compared: polyimide alone, untreated alumina platelets and the coating containing silanized alumina platelets. The spectra are presented in Figure 2.28. It is worth noticing that the spectrum of the untreated alumina platelets showed no significant peaks, indicating that any observed peaks in the coating spectrum can be attributed to the polyimide and to theinteractions between the polymer and the silanized platelets.

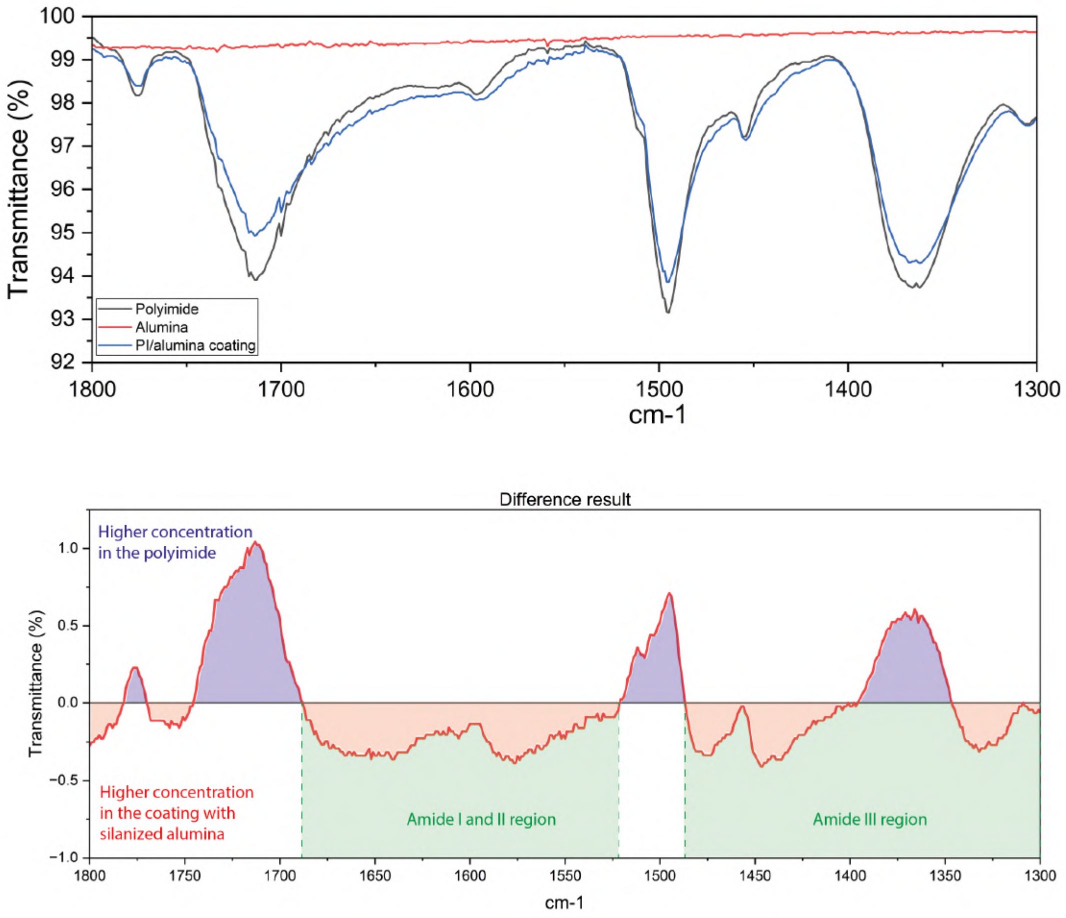

Figure 2.28: FTIR transmittance peaks of polyimide, untreated alumina platelets and the polyimide/silanized alumina platelets coating (top) and difference between the transmittance of the spectra of the coating and of the polyimide.

At first glance, the spectra of the coating and the polyimide appear to have a similar shape, with the coating displaying higher transmittance. This could initially suggest interference from the alumina platelets, as they may scatter or block some infrared radiation. However, if this were only due to scattering, the difference in transmittance would be relatively constant across the entire spectrum. Instead, the transmittance differences are wavelength-dependent, indicating chemical changes rather than uniform scattering effects.

To further investigate, the difference in transmittance between the coating and the pure polyimide was plotted. Positive values correspond to bonds with higher concentrations in the polyimide, while negative values indicate bonds with higher concentrations in the coating. A significant positive peak was observed around 1714 cm^{-1}, corresponding to the carboxylic acid C=O stretching vibration. This suggests a lower concentration of carboxylic acid groups in the coating.

Additionally, regions associated with amide bonds showed higher concentrations in the coating. An exception to this trend was observed at 1362 cm^{-1}, a characteristic peak of the imide C–N stretching mode, which did not display the same pattern. However, in the surrounding ”wings” of this region, the trend still holds.

These two factors support the formation of covalent bonds between the silanized platelets and the polymer, with the reaction between the carboxylic acid groups of polyamic acid and the amine groups of APTES to form amide bonds.

This evidence confirms the successful silanization of the alumina platelets and their effective incorporation into the coating structure.

2.5.3. Hydrophobicity

The silanization process is also used to increase the hydrophobicity of the alumina platelets, enabling their effective adsorption to the air–water interface during the coating manufacturing process. The effectiveness of the silanization in increasing the hydrophobicity of the alumina platelets was evaluated through water contact angle (CA) measurements. The results, as presented in Figure 2.29, show a significant increase in hydrophobicity after silanization. The contact angle for the coating containing silanized alumina platelets was 97.3° ± 1.2°, compared to 60.2° ± 1.6° for the coating with untreated platelets. This increase confirms that the surface modification with APTES successfully improved the water-repellent properties of the alumina platelets.

(a) Untreated

(b) Silanized

Figure 2.29: Water contact angle of coating with untreated and with silanized alumina platelets.

2.5.4. Surface Energy

Contact angle measurements are crucial for determining the surface energy of materials, a key parameter influencing adhesion. Water contact angle is usually used to provide information about the wettability of the surface. However, because we are interested in the forces between the lunar dust particles and the surfaces, using just water was not enough. A broader picture was needed, using a series of liquids with different surface energy components to get a more accurate idea of the surface energy, and therefore checking how these surface energies influenced the antidust performance of the difference surfaces.

Three droplets (5 µl each) of the test liquid were placed on the surface of interest. The contact angles were determined for each droplet and the CA of the liquid on the surface was calculated as the average of these measurements. To measure the CA, a KSV CAM 200 Optical Contact Angle Meter was used.

Oss and Good acid-base method

To determine the surface energy of different surfaces, van Oss and Good acid-base method was employed [22]. This method is based on the Young's equation, which relates the contact angle (θ) of a liquid on a solid surface to the interfacial tensions, as seen in Figure 2.30:

$$\gamma_{lv} \cos\theta = \gamma_{sv} - \gamma_{sl} \tag{2.1}$$

Where:

- γ_{lv} is the liquid-vapor interfacial tension (surface tension of the liquid),
- γ_{sv} is the solid-vapor surface energy,
- γ_{sl} is the solid-liquid interfacial energy.

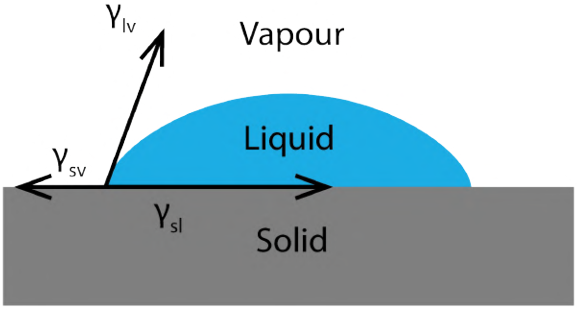

Figure 2.30: Schematic diagram of a liquid drop on a solid surface showing the interfacial tensions at the three phase boundary.

The acid-base method of Van oss et al.(1988) [51] separates the total surface energy (γ_s) of the solid into two main components: Lifshitz - van der Waals (γ_s^{LW}) and acid-base contributions that include two components(electron donor - γ_s^+) - and electron acceptor - γ_s^-):

$$\gamma_s = \gamma_s^{LW} + 2\sqrt{\gamma_s^+ \gamma_s^-} \tag{2.2}$$

and the solid-liquid interfacial energy is therefore:

$$\begin{aligned}\gamma_{sl} = \left(\sqrt{\gamma_s^{LW}} - \sqrt{\gamma_l^{LW}}\right)^2 + 2\left(\sqrt{\gamma_s^+ \gamma_s^-} + \sqrt{\gamma_l^+ \gamma_l^-}\right) \\ - 2\left(\sqrt{\gamma_s^+ \gamma_l^-} + \sqrt{\gamma_s^- \gamma_l^+}\right)\end{aligned} \tag{2.3}$$

The Young's equation becomes then:

$$\frac{(1+\cos\theta)\gamma_l}{2} = \sqrt{\gamma_s^{LW}\gamma_l^{LW}} + \sqrt{\gamma_s^+ \gamma_l^-} + \sqrt{\gamma_s^- \gamma_l^+} \tag{2.4}$$

By using three different liquids on the same solid surface, three distinct contact angles can be measured. Since the surface tension parameters of the liquids are known, solving a 3×3 system of equations allows for the determination of the surface properties of the solid.

Using this method, three liquids are required to determine the surface energy of the surface. One needs to be a liquid with only Lifshitz - van der Waals component and the other two have to be liquids with known acid and base parts. Water should always be used as one of the test liquids, as the neutral point in the Lewis scale [29]. Four liquids, with the chemical formulas seen in Figure 2.31, with different components of surface energy were used, three at a time, for contact angle measurements. The contact angle results are described in Appendix A. The surface energy components used in the calculations for the different test liquids are summarized in Table 2.5:

Table 2.5: Surface energy components of the different test liquids, at 20ºC [40]

Liquid	γ_l**[mN/m]**	γ_l^{LW}**[mN/m]**	γ_l^{+}**[mN/m]**	γ_l^{-}**[mN/m]**
Diiodomethane	50.8	50.8	0.0	0.0
Ethylene Glycol	48.0	29.0	1.92	47.0
Glycerol	64.0	34.0	3.92	57.4
Water	72.8	21.8	25.5	25.5

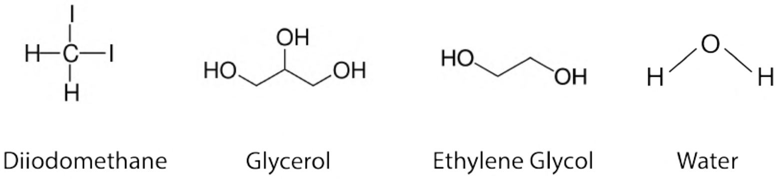

Figure 2.31: Structural formulas of the test liquids used to calculate the surface energy of the different surfaces.

Spark Plasma Sintering (SPS) of LMS-1

Due to the powdered nature of LMS-1, it was not possible to directly place test liquid droplets onto the powder for measurement. To overcome this, spark plasma sintering (SPS) was used to consolidate the LMS-1 powder into a solid form suitable for contact angle testing. SPS is a manufacturing technique that utilizes uniaxial pressure and a pulsed or unpulsed DC/AC current to consolidate powders into dense structures, as illustrated in the diagram in Figure 2.32. This method has been previously studied for the consolidation of lunar regolith simulants [31].

For this study, an SPS machine (FCT Group, Germany) was used, operated under vacuum with a 20 mm graphite die and graphite punches. During sintering, a direct pulsed current of 1000 A, voltage of 6V, and pulse on/off cycle of 15:5 ms was applied. A pyrometer was used for temperature regulation, focusing on the inside of the top punch of the die. To prevent adhesion and unwanted reactions between the LMS-1 powder and the graphite mold, a 0.2 mm thick graphite foil was placed inside the die.

Following the method of Laot et al. (2021)[31], 4 g of LMS-1 powder (sieved to a maximum particle size of 50 µm) was sintered at 1050°C under a pressure of 80 MPa. The resulting consolidated LMS-1 disk is shown in Figure 2.33. After sintering, the surface was polished using silicon carbide paper (#4000) to ensure a smooth and uniform surface for accurate contact angle measurements.

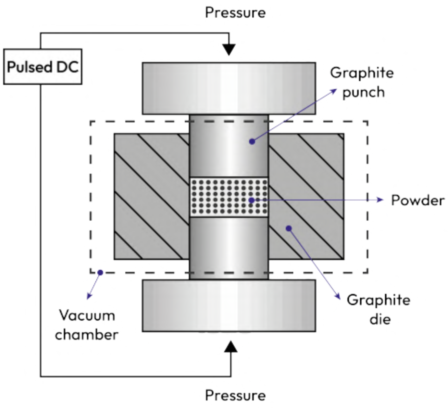

Figure 2.32: Diagram of the spark plasma sintering process.

Figure 2.33: Resulting samples of SPS of LMS-1.

Surface energy results

Young's equation assumes that a solid surface is chemically homogeneous and topographically smooth, providing an idealized model for contact angle measurements. However, real surfaces are rarely perfectly smooth or chemically uniform. In reality, the measured contact angle represents the angle between the tangent to the liquid-fluid interface and the actual, local surface of the solid, rather than an idealized flat plane.

To accurately determine the surface free energy of a solid, it is necessary to use the actual contact angle rather than the apparent, measured contact angle. The Wenzel equation [55] provides a correction for surface roughness effects by relating the actual Young's contact angle (θ_Y) to the measured contact angle (θ_m), with r as the roughness ratio:

$$\cos\theta_m = r\cos\theta_Y \tag{2.5}$$

The roughness ratio can be determined using S_{dr}[41]. It is given by:

$$r = 1 + \frac{S_{dr}}{100} \tag{2.6}$$

With the actual contact angles, the surface energy of the different surfaces as well as its components were calculated. The results are in Table 2.6

Table 2.6: Surface energy components of the different test surfaces.

Surface	γ_s**[mN/m]**	γ_s^{LW}**[mN/m]**	γ_s+**[mN/m]**	γ_s^-**[mN/m]**
Aluminium 1060	41.36	36.15	21.73	0.31
Aluminium 1060 (not cleaned)	39.22	38.50	10.89	0.01
Anodized aluminium	37.62	33.32	1.30	3.55

Continued on next page

Table 2.6: Surface energy components of the different test surfaces. (Continued)

PEEK	43.11	39.33	13.23	0.27
ZrB2	41.41	39.21	12.58	0.10
Polyimide	41.40	36.63	7.99	0.71
PI/alumina coating	34.02	33.96	0.75	0.00
PI/alumina coating (+)	39.64	34.7	36.43	0.03
PI/alumina coating (-)	35.70	34.28	1.18	0.12
PI/LMS-1 coating	34.81	34.54	0.21	0.09
PI/LMS-1 coating (polished)	34.70	34.54	0.73	0.01
LMS-1 coating (SPS)	34.83	34.40	28.42	0.00

2.5.5. Surface Roughness

Surface roughness is a critical parameter when evaluating adhesion. In this thesis, surface roughness measurements were performed using confocal microscopy, that provides detailed surface topography. The analysis was conducted using a Keyence VK-X1000 confocal scanning microscope at 20x magnification.

The root mean square (RMS) height (S_q) and Developed Interfacial Area Ratio (S_{dr}) values were calculated to assess the surface roughness. As seen in Figure 2.34a, the S_q parameter represents the standard deviation of the height distribution of the surface and is one of the most commonly used metrics in surface characterization. It provides statistically robust and stable results, as it is minimally influenced by surface scratches, contamination, or measurement noise. S_{dr} on the other hand represents the percentage of the area's additional surface area due to the texture in relation to the perfectly planar area, as seen in Figure 2.34b. The values for the different surfaces studied are in Table 2.7.

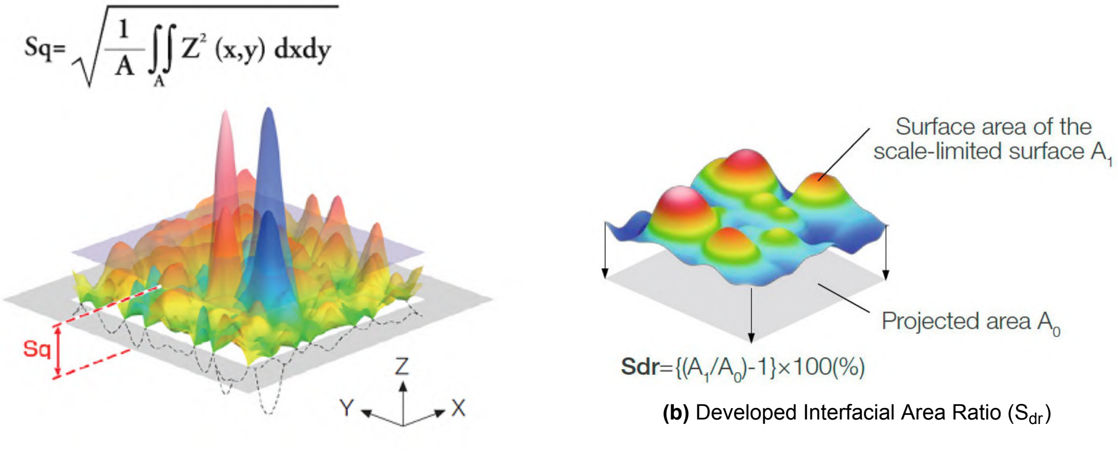

(b) Developed Interfacial Area Ratio (S_{dr})

(a) Root mean square height (S_q)

Figure 2.34: Surface roughness parameters studied [39].

Table 2.7: S_q and S_{dr} values of the different surfaces.

Surface	**S_q [µm]**	**S_{dr} [-]**
Aluminium 1060	1.06 ± 0.19	0.05793 ± 0.00496
Aluminium 1060 (not cleaned)	1.92 ± 0.09	0.06234 ± 0.00446
Anodized aluminium	1.05 ± 0.05	0.35040 ± 0.06301
PEEK	0.58 ± 0.02	0.00118 ± 0.00039
ZrB2	0.20 ± 0.04	0.00320 ± 0.00065
Polyimide	0.76 ± 0.11	0.01039 ± 0.00359
PI/alumina coating	1.12 ± 0.15	0.11570 ± 0.05230
PI/alumina coating (+)	1.05 ± 0.13	0.19310 ± 0.08165
PI/alumina coating (-)	1.07 ± 0.21	0.17610 ± 0.07236
PI/LMS-1 coating	6.35 ± 0.37	1.04900 ± 0.05215
PI/LMS-1 coating (polished)	2.85 ± 0.20	0.25710 ± 0.02975
LMS-1 (SPS)	2.88 ± 0.48	0.21820 ± 0.05315

2.5.6. Hardness and indentation modulus

To characterize the mechanical properties of the coating, microindentation testing was performed using a CSM Micro Indentation Tester equipped with a Vickers tip, a square-based pyramid-shaped diamond. This method was chosen due to its applicability over a wide range of hardness values, making it particularly suitable for this study since the materials involved in the coating exhibit vastly different hardness levels (Polyimide – 0.37 GPa[57], Alumina – 10 GPa[50]).

The indentation tests were conducted at five different loads: 250 mN, 500 mN, 1000 mN, 1500 mN, and 2000 mN, with each load test being repeated three times. The load and unload time are of 30s with a pause of 2s between them. The spacing between successive indentations was maintained at 0.5 µm to prevent interference from residual stress fields of adjacent indents.

From these tests, two primary mechanical properties were obtained: hardness and indentation modulus (E_{IT}). The hardness was determined based on the applied force and the projected surface area of the indentation, as illustrated in Figure 2.35. The E_{IT} describes the elastic surface behavior of the material during indentation. It was calculated using the Oliver–Pharr method from the unloading portion of the load–displacement curve, like the one shown in Figure 2.36. Both of these parameters are direct indicators for wear resistance.

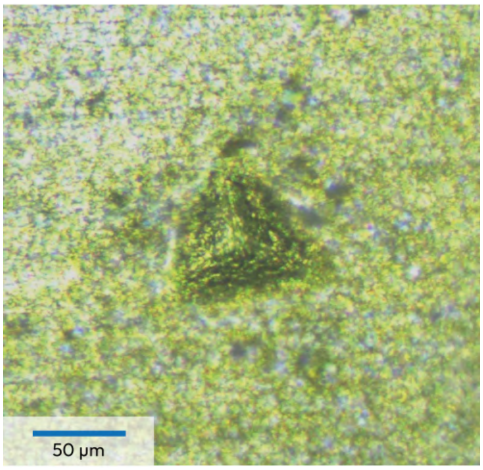

Figure 2.35: Indentation using a Vickers indenter on PI/alumina platelets coating.

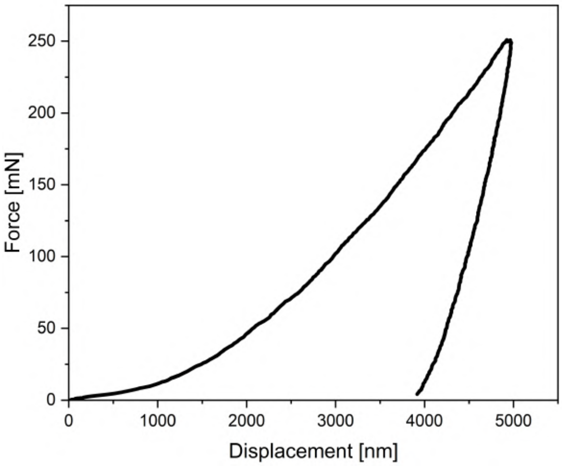

Figure 2.36: Load–displacement curve of a Vickers indentation on PI/alumina platelets coating at a load of 250mN.

Due to the small thickness of the coating (5 µm), direct measurement of its hardness is not possible across all indentation loads. This is because, at higher indentation depths, the underlying aluminium substrate also undergoes plastic deformation, affecting the measured hardness. It is generally assumed that this substrate effect becomes significant when the indentation depth exceeds one-tenth of the film thickness.[33] Given this constraint, the microindenter would require a minimum indentation depth of 0.7 µm, which did not produce accurate load–displacement curve, making it necessary to apply a correction model. To determine the true hardness of the coating, the Lesage model [33] was used, which allows the extrapolation of surface hardness from standard microindentation tests.

Similarly, for coated materials, a direct measurement of (E_{IT}) is complicated by the influence of the substrate, as the elastic deformation field extends beyond the indentation area, affecting the measured values. To mitigate this, the method used by Lorenz et al. (2021)[36] was applied, where indentation modulus results at different loads were extrapolated to zero depth, thereby isolating the coating's elastic response.

A detailed explanation of these correction models is provided in Appendix B. The final results of the hardness and indentation modulus for both the coating and the substrate are presented in Table 2.8.

Table 2.8: Hardness (at 250mN) and E_{IT} of the surfaces studied.

Surface	Hardness [GPa]	E_{IT} [GPa]
PI/alumina coating	0.59 ± 0.02	16.59 ± 0.27
Aluminium 1060	0.45 ± 0.02	26.50 ± 0.79

3

Antidust Performance

This chapter starts by explaining the design and construction of a vacuum chamber for dust adhesion tests, and the image processing techniques used to quantify dust coverage. It provides a detailed explanation of the methods and tools used to study the antidust properties of the coating, ensuring accurate and reproducible results for the subsequent analysis of dust adhesion behavior.

It goes on to explores the antidust performance of the polyimide/alumina platelet coating through various experimental tests, also comparing it to different surfaces. These tests were designed not only to investigate the origins of dust adhesion but also to evaluate how the coating responds to external stressors, such as mechanical erosion and UV radiation exposure.

By simulating different lunar-relevant conditions, this study provides insight into the effectiveness and durability of the coating in mitigating dust accumulation in extreme environments.

3.1. Antidust Setup

To evaluate the antidust performance of the coated samples, it was necessary to design and construct an in-house vacuum chamber. This custom-built chamber was required to meet the following criteria:

1. Sustain a pressure of 1 mbar inside the chamber.
2. Accommodate samples measuring 20x20 mm.
3. Include an inlet to connect an air pump for pressure regulation.
4. Have a transparent window to allow the microscope to observe the samples during testing.

3.1.1. Material Selection

The final choice for the chamber material was polymethyl methacrylate (PMMA). PMMA is transparent to visible light, making it suitable for microscopy, and its mechanical properties are sufficient to withstand the pressure difference for a small vacuum chamber.

3.1.2. Chamber Design

The chamber design consisted of a PMMA pipe with an attached PMMA plate at the bottom and a screw-on PMMA lid at the top for easy access. The dimensions were determined based on the working distance of the microscope and the required structural integrity to withstand the vacuum.

Microscope Model: AM7915MZT The microscope's working distance varies depending on the magnification [14]:

- At 50x magnification, the working distance is 43.5 mm.
- At 100x magnification, the working distance is 29.2 mm.

A chamber height of 10 mm was chosen, as the microscope can simply be positioned higher if a larger working distance is needed.

The outer pipe diameter was selected from the available sizes of 50 mm, 60 mm, 70 mm, 80 mm, 90 mm, and 100 mm. A 70 mm diameter pipe was chosen as it provides enough room for the sample while minimizing the volume of air that needs to be pumped out.

To ensure the chamber could withstand the vacuum, the required wall thickness (t) was calculated using the hoop stress formula for thin-walled cylinders:

$$t = \frac{\Delta P \times r}{\sigma_{\text{allowable}}} \tag{3.1}$$

Where:

- ΔP is the pressure difference: 101,315 Pa (considering a vacuum pressure of 10Pa),
- r is the inner radius: 35 mm,
- $\sigma_{\text{allowable}}$ is the allowable stress for PMMA: 35,000,000 Pa (σ_{yield} = 70 MPa with a safety factor of 2).

This results in a calculated value of 0.101 mm of wall thickness. Since the wall thickness options are of 10mm or 6mm, the pressure is therefore not a limiting factor.

The final design seen in Figure 3.1 uses a pipe with an outer diameter of 70mm and a thickness of 10mm so as to be able to accommodate the threaded inserts for the M3 screws used for the lid. The technical drawing of the chamber with the relevant dimensions can be seen in Appendix C.

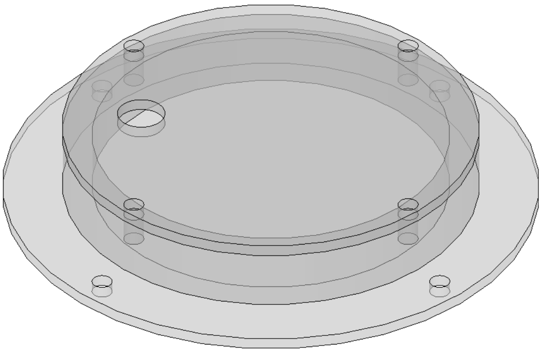

Figure 3.1: 3D model of the vacuum chamber used in the antidust tests.

3.2. Procedure

To evaluate the antidust performance of the coatings, the following procedure in Figure 3.2 was followed:

1. Carefully place the sample inside the vacuum chamber and secure it to the bottom using a small amount of black tacky tape. Ensure that the sample remains horizontal, providing optimal conditions for microscopy imaging.
2. Use a small spatula to scoop the LMS-1 lunar dust simulant. Deposit the dust onto the sample through a funnel positioned to direct the simulant to the center of the sample.
3. To enhance the airtight seal, apply Dow Corning®high-vacuum grease inside the threaded holes and a thin layer of tacky tape between the lid and the chamber walls, like in Figure 3.3. Then screw the lid onto the chamber.

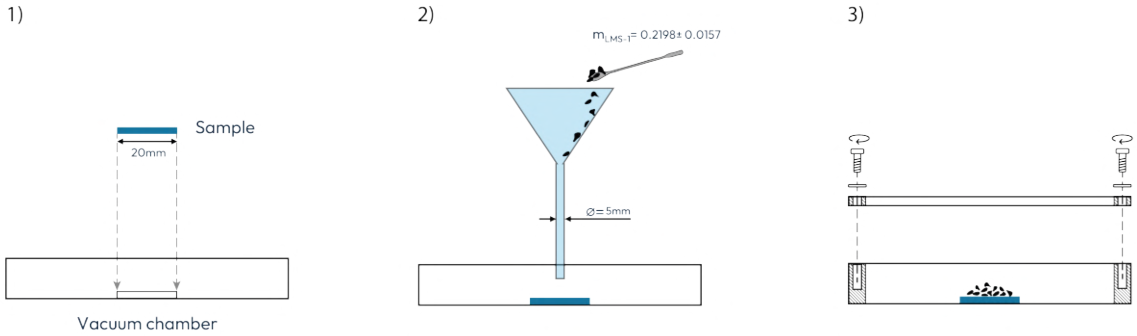

Figure 3.2: Diagram of the vacuum chamber preparation.

(a) Vacuum grease.

(b) Tacky tape.

Figure 3.3: Application of vacuum grease in the screw holes and of tacky tape around the wall of the vacuum chamber to create an airtight seal.

As seen in Figure 3.5 and Figure 3.6, the chamber was connected to an air pump and a manometer to monitor the internal pressure. At the inlet connection of the vacuum chamber, a filter paper was added to prevent any dust from entering the pump. The vacuum chamber was placed under the microscope, which was held by a microscope holder with a flat base that provided a stable resting platform for the chamber. The microscope was aligned to focus on the center of the sample, as seen in Figure 3.4. For all tests, the magnification used was around 108x, except for the ZrB_2 that due to its higher thickness, required less magnification (105x) to focus on the surface. The air pump was turned on, and the chamber was evacuated until the manometer indicated a pressure of 1 mbar. A brightfield high-resolution image of the sample's surface was captured using the digital microscope with the built-in coaxial light. The chamber and microscope were then manually rotated 90°, and a second image of the surface was captured, as described in Figure 3.7. This second picture is the one analysed to obtain the results of the antidust performances tests. The procedure was repeated for 3 different samples of each material. Because the digital microscope used has a resolution of 5.0 Megapixel (2592 x 1944 pixels), at the magnification of 108x, 1 pixel corresponds to 1.2μm, and therefore these are the smallest sized particles that are possible to differentiate.

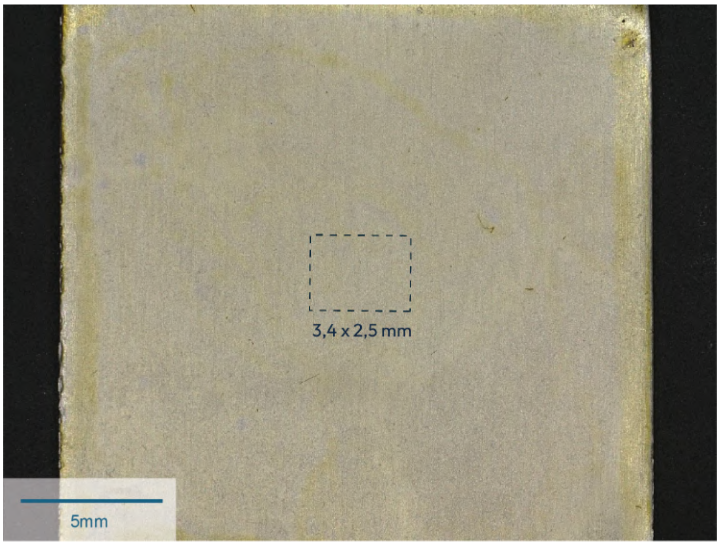

Figure 3.4: Field of view of the microscope at 108x magnification.

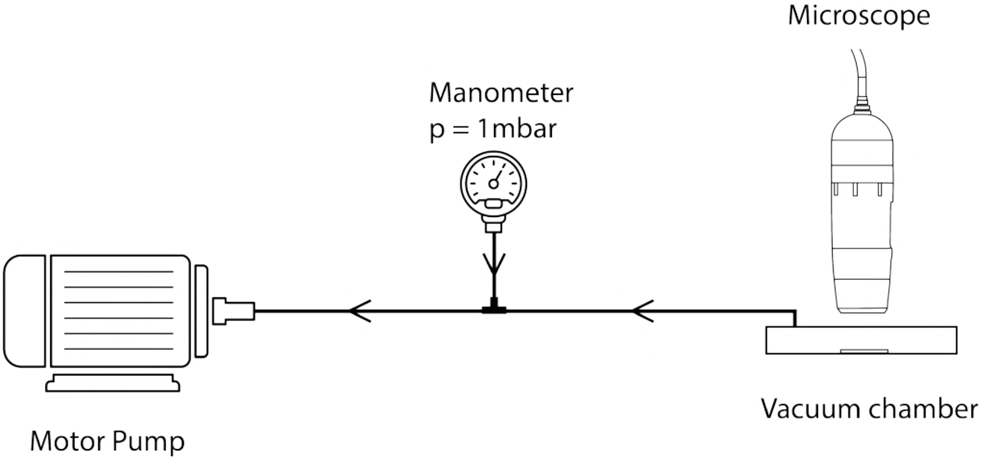

Figure 3.5: Diagram of the test setup during the experiments.

Figure 3.6: Test setup during the experiments.

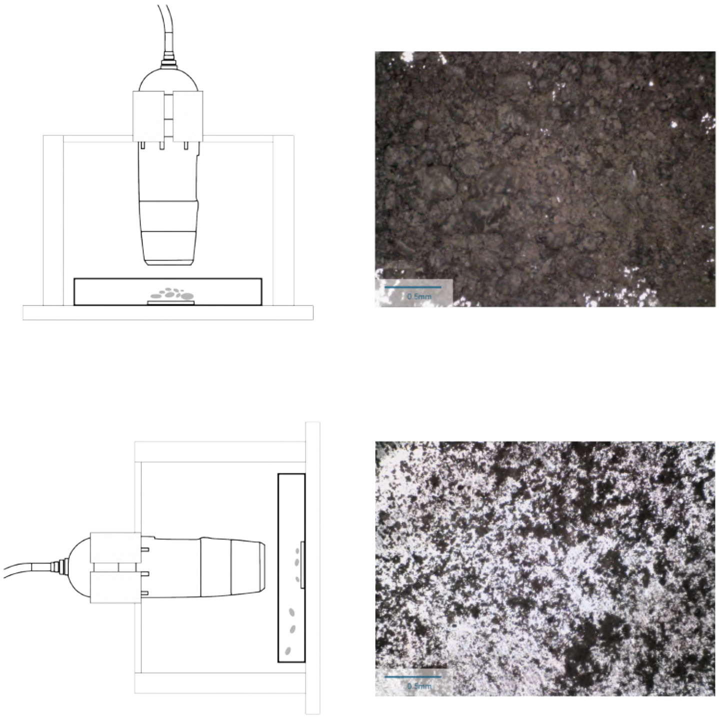

Figure 3.7: Before (top) and after (bottom) rotating the microscope + chamber 90°. The sample is aluminium 1060 (not cleaned).

3.2.1. Dust-covered area

To quantify the antidust performance, the percentage of the surface area covered by lunar dust simulant was calculated using ImageJ software.

The first step in the analysis involved converting the captured images to grey scale, where each pixel of the image has a corresponding number between 0 and 255 that represents its intensity, with 0 being black and 255 being white. This makes it easier to distinguish dust particles from the background during the thresholding process. Thresholding was then applied to create a binary image where the dust particles were separated from the background. The sliders were adjusted until the dust particles appeared as white regions and the background as black. This is the threshold value. Although this value varied from material to material due to differences in contrast between the dust and the surface, the same threshold was maintained across the three tests used to determine the dust coverage for a given surface. For example, a threshold value of 115 was chosen for all the tests using the PI/alumina platelets coating. This means that all the pixels with intensity between 0 and 115 will be treated as dust particles and their intensity will be changes to 255 (white). Similarly, the pixels with intensity in the range of 116 to 255 will be considered as the background surface and their intensity will be changes to 0 (black). The "Analyze Particles" tool in ImageJ was then used in the thresholded images. This tool calculated the area of white pixels, which corresponds to the regions covered by dust. The different images resulting from this process can be seen in Figure 3.8. For comparison, Figure 3.9 depicts the same process but now done at a sample without any dust particles. The final completely black picture shows that the program correctly does not detect any dust.

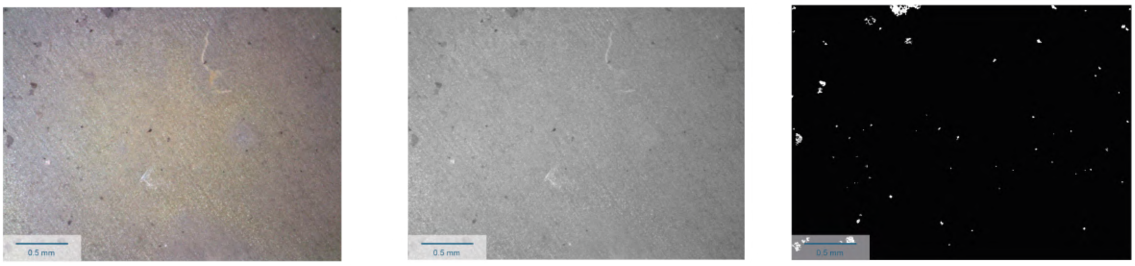

Figure 3.8: Sequence of the steps performed with ImageJ to calculate the percentage of dust-covered area. First the image obtained with the microscope, then the grey scale image and finally the image after the threshold is applied. The sample is aluminium coated with the polyimide/alumina platelets coating.

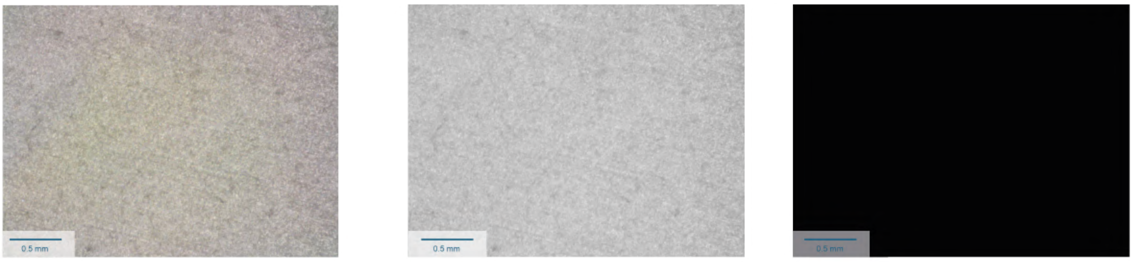

Figure 3.9: Raw, grey scale and thresholded images of a polyimide/alumina coating before the test, without any dust particles.

Since both the dust simulant (LMS-1) and the coating material share the same chemical composition, the image processing method used in previous dust adhesion tests were not feasible for the antidust tests of the samples coated in the polyimide/LMS-1 particles coating. Differentiating between dust particles and the coating surface was challenging due to the lack of contrast. An alternative image processing approach was then used. First, 5 images were taken from the coating surface before testing and after the test, 5 additional images were taken from the same positions to ensure a direct comparison, as seen in Figure 3.10.

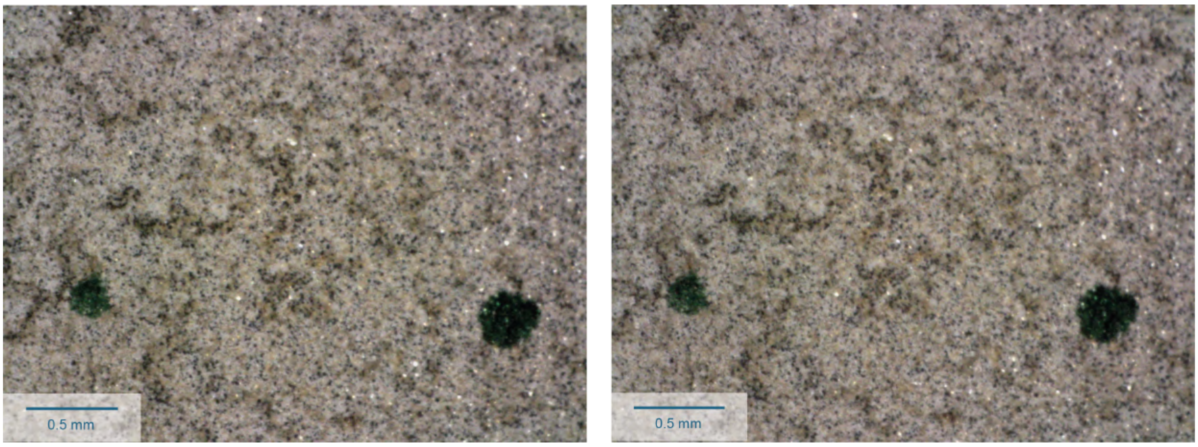

(a) Before. **(b)** After.

Figure 3.10: Digital microscope images of the coating before and after the antidust performance test. The particles are almost impossible to differentiate.

Because slight movements or misalignments can occur during testing and imaging, an ImageJ plugin was used to perform recursive repositioning, aligning the post-test images precisely with the pre-test images, like the one in Figure 3.11a. To improve the accuracy of this process, small dots were added to the surface with a pen. This facilitates the detection of any translation and/or rotation.

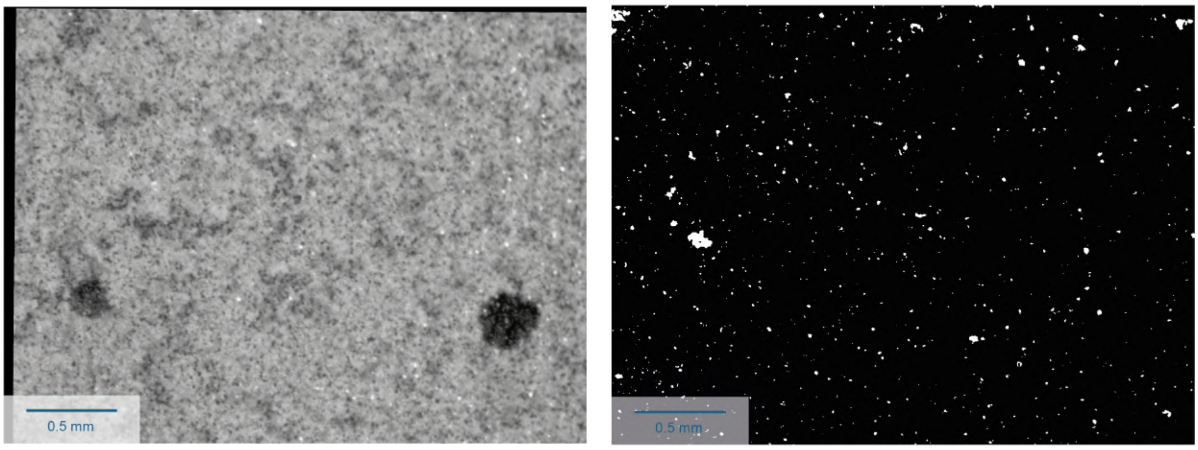

(a) Post-test image after aligning with the pre-test ones. **(b)** Final thresholded image.

Figure 3.11: Comparison of the post-test image before and after thresholding.

After image alignment, the changes in the coating surface were analyzed using an ImageJ plugin that applies a subtract dark median filter. This method highlights the dust particles newly adhered to the surface by subtracting the pre-test image from the post-test image and generates a binary image where the new dust particles appear as white regions against a black background (Figure 3.11b). The median filter removes noise and refines particle detection.

Any extra artifacts caused by image realignment were manually removed by cropping the image to the area of interest, ensuring only relevant dust adhesion was considered.

3.3. Antidust results

3.3.1. Adhesion Forces

As discussed in previous sections, Van der Waals forces, electrostatic interactions, and capillary forces are the primary mechanisms governing particle-surface adhesion. Each of these forces plays a role depending on the environmental conditions, such as humidity and surface charge. Various tests were conducted to assess these adhesion mechanisms under different simulated conditions. These experiments were designed to mimic scenarios that could occur during a lunar mission, providing a comprehensive evaluation of the coating's antidust capabilities.

Material's Surface Properties

To investigate how the lunar simulant adheres to different surfaces under vacuum conditions, antidust tests were conducted at a pressure of 1 mbar on various materials. These included three different bare surfaces representative of different classes of materials: Al 1060 (metal), PEEK (polymer), and ZrB$_{(}$2) (ceramic). Additionally, several treated and coated surfaces were tested: Al 1060 samples with adhesive residue from the protective film (not cleaned), anodized aluminum samples, Al 1060 coated with only polyimide, Al 1060 coated with polyimide/alumina platelets, and Al 1060 coated with polyimide/LMS-1 particles (both as-manufactured and polished with #4000 silicon carbide paper). The results of the test can be seen in Figure 3.12.

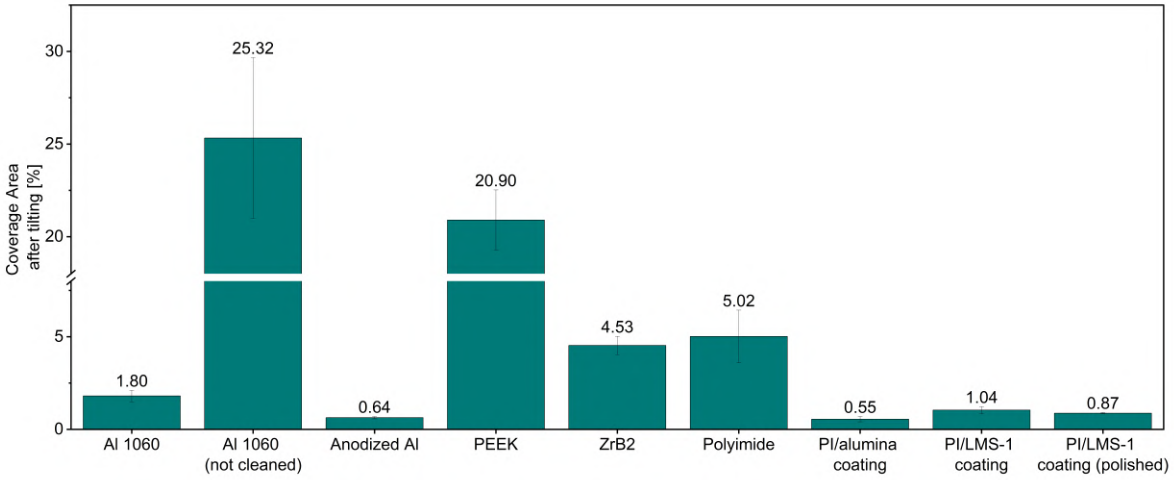

Figure 3.12: Coverage area after tilting of different surfaces under vacuum.

From these results, it is evident that the aluminum sample with glue residue exhibited the highest dust coverage after tilting (25.32%), while the **polyimide/alumina platelets coating** displayed the **lowest coverage (0.55%)**. The bare aluminum and anodized aluminum samples also exhibited relatively low dust adhesion, with 1.80% and 0.64% dust coverage, respectively. It is worth noting that aluminum naturally forms a thin oxide layer upon exposure to air, and anodization produces a micro-thin alumina coating so at the surface of these samples, alumina is present. The **polyimide/LMS-1 particles coatings** also demonstrated **low dust adhesion**, though slightly higher than the polyimide/alumina platelets coating, with 1.04% and 0.87% for the unpolished and polished variants, respectively. In contrast, PEEK, ZrB_2, and the polyimide film exhibited intermediate levels of dust adhesion, with values of 20.90%, 4.53%, and 5.02%. The relatively higher dust coverage on the polyimide sample suggests that the surface composition of the polyimide/alumina platelets coating is indeed dominated by alumina rather than polymer, as expected.

To understand the observed dust adhesion trends, the influence of surface properties was further analyzed. In dry vacuum conditions, dust adhesion is expected to be dominated by Van der Waals and electrostatic forces due to the absence of moisture, which eliminates capillary forces [52]. Since neither the dust nor the surfaces were previously exposed to external charging effects, electrostatic forces were neglected. This allowed the focus to be placed solely on **Van der Waals interactions**.

Using Equation 1.2, Van der Waals forces were calculated for each surface, assuming a particle radius of 30 µm, which represents the **average particle size** of the lunar dust simulant batch used in the study. The resulting values were plotted against the measured dust coverage values in the graph in Figure 3.13.

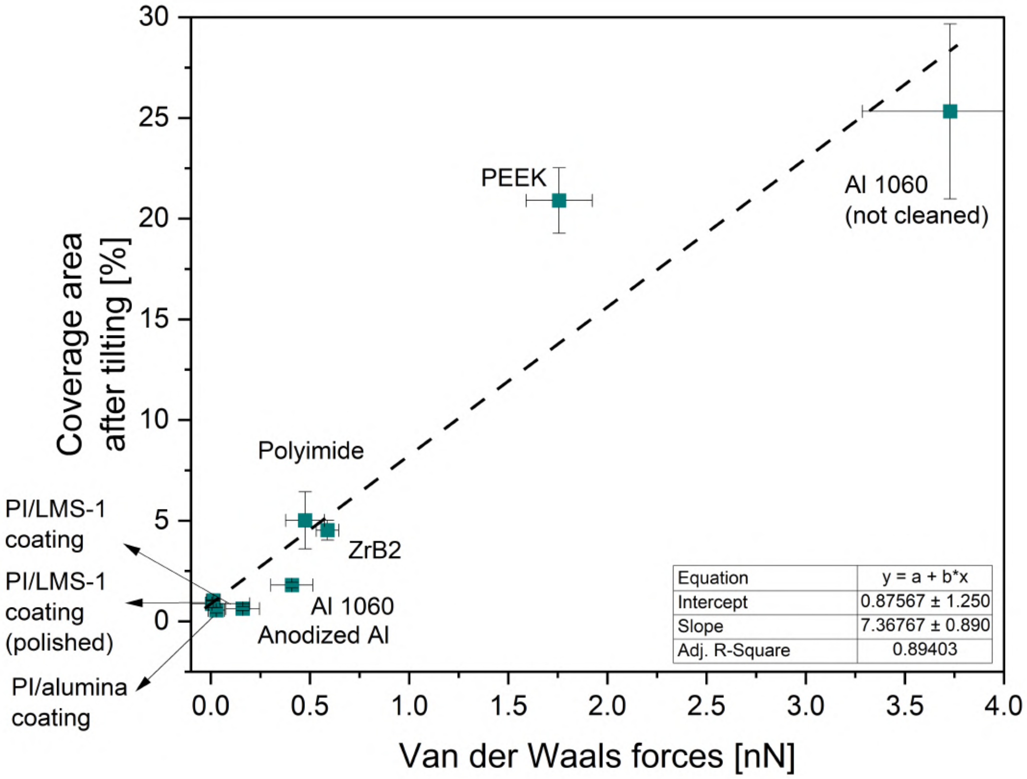

Figure 3.13: Coverage area after tilting of different surfaces under vacuum as a function of the van der Waals forces. (R=30µm)

While a linear correlation is observed with an adjusted R^2 of 0.8940, some discrepancies arise, particularly for surfaces with higher dust coverage. Examining the final thresholded images from the tests (Figure 3.14) reveals that most of the particles remaining on the surface after tilting are significantly smaller than 30 µm, with an average size of approximately 4 µm (3 pixels). Given this, Van der Waals forces were recalculated using a **particle radius of 2 µm**, and the results were plotted again in Figure 3.15.

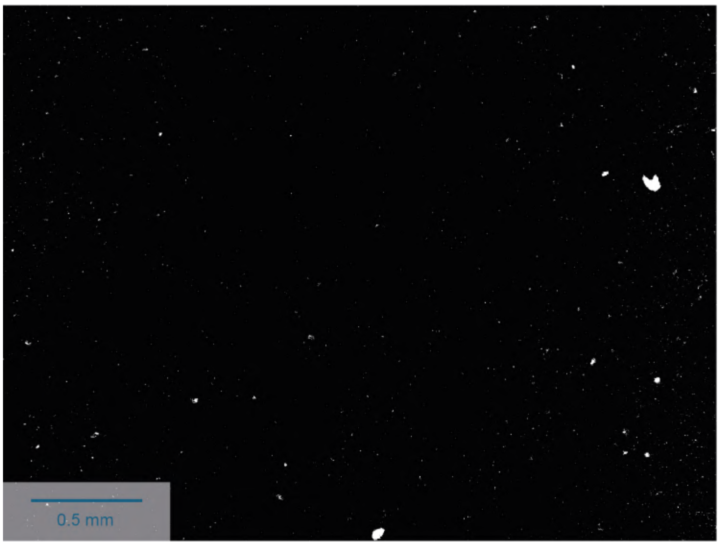

Figure 3.14: Thresholded image of the surface of a polyimide/alumina platelets coating after the test, showing the smaller size of the particles.

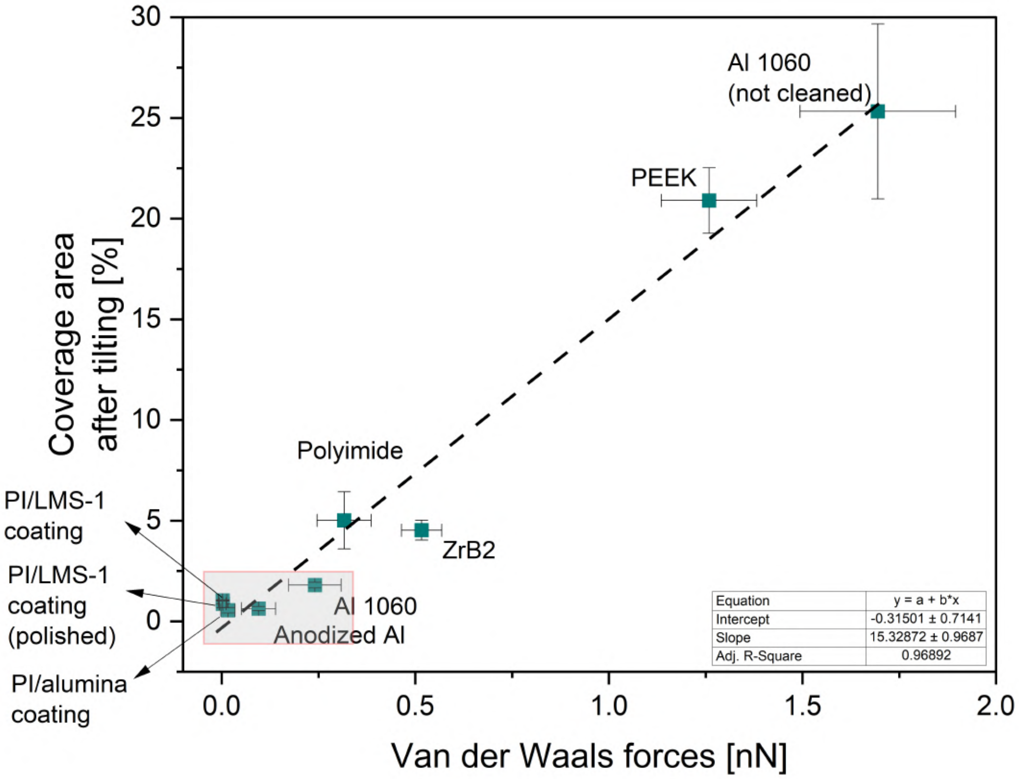

Equation	y = a + b*x
Intercept	-0.31501 ± 0.7141
Slope	15.32872 ± 0.9687
Adj. R-Square	0.96892

Figure 3.15: Coverage area after tilting of different surfaces under vacuum as a function of the van der Waals forces (R=2µm).

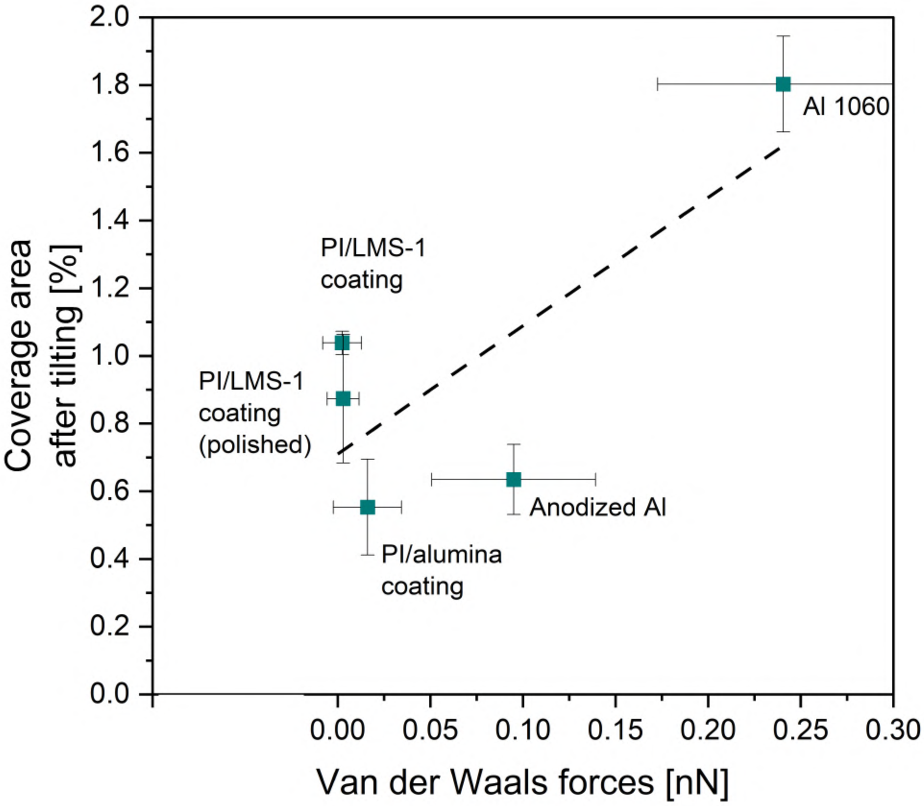

Figure 3.16: Zoomed in portion of the graph above.

The recalculated Van der Waals forces exhibit a **stronger linear correlation** with dust adhesion (R^2 = 0.9689). The most notable outlier in this analysis is ZrB_2, which has the lowest surface roughness among the materials tested (Sq = 203 nm). This suggests that ZrB_2 is less affected by the **”inlaid effect”**, a phenomenon in which smaller dust particles settle into surface asperities, effectively increasing dust coverage (schematic in Figure 3.17) [58]. The smoother surface of ZrB_2 reduces this effect, contributing to its relatively lower than expected dust coverage.

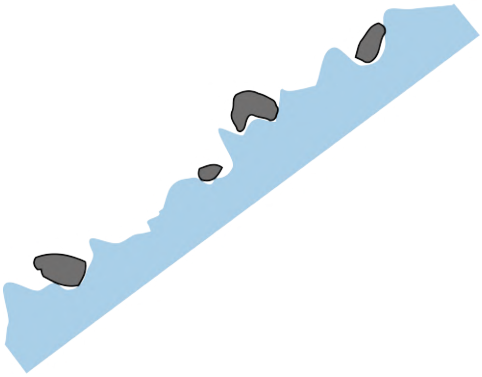

Figure 3.17: Schematic diagram of the inlaid effect.

Despite the strong correlation between Van der Waals forces and dust adhesion, some anomalies remain. For example, while the polyimide/LMS-1 particles coatings exhibit the lowest Van der Waals interactions, the polyimide/alumina platelets coating and anodized aluminum samples show even lower dust coverage. This further supports the hypothesis that the inlaid effect plays a role, as the LMS-1 coatings have a higher surface roughness (Sq = 6.35 μm and 2.84 μm for the unpolished and polished samples, respectively) compared to anodized aluminum (Sq = 1.05 μm) and coated Al 1060 with polyimide/alumina platelets (Sq = 1.12 μm).

Another notable observation when comparing both graphs is that larger particles exhibit stronger Van der Waals interactions due to their greater contact area with the surface. However, as mentioned, the tilting tests show that the remaining adhered particles tend to be smaller. In addition to the inlaid effect, this can be explained by the role of gravitational forces in particle detachment during the test. Gravitational forces scale with mass, meaning larger particles experience stronger detachment forces. Thus, while Van der Waals interactions increase with particle size, the gravitational force acting against adhesion also increases, leading to preferential removal of larger particles.

The intensity of Van der Waals forces is strongly influenced by the Hamaker constant, which in turn depends on the **difference in surface energies** between the interacting materials. A larger disparity in surface energy between two materials results in stronger adhesive forces. This trend is evident in the experimental results, particularly when comparing the coatings composed of materials with similar compositions to the lunar simulant.

The polyimide/LMS-1 particles coating exhibited the lowest Van der Waals forces among all tested samples. This aligns with the fact that the top layer of the coating is composed of the lunar simulant, minimizing the surface energy difference between the dust particles and the coated surface. Following this trend, the coatings with alumina at their surface, such as the polyimide/alumina platelets coating, anodized aluminum, and to certain extent the aluminium 1060, also displayed relatively low dust adhesion. Alumina is one of the main constituents of lunar regolith, and its presence on the surface of these samples contributes to a lower surface energy contrast between the dust particles and the coating, thereby reducing Van der Waals attraction.

This suggests that surface energy matching can play a key role in mitigating dust adhesion, reinforcing the concept that coatings with compositions similar to lunar dust can help minimize adhesion forces.

Charged Environment

As previously mentioned, lunar dust is expected to exhibit different surface charges depending on the time of day. During daylight, exposure to UV radiation induces a positive charge on dust due to the photoelectric effect, while at night, the interaction with solar wind electrons leads to a negative charge. Since electrostatic interactions can play a significant role in adhesion, a test was conducted to investigate the influence of charge on the antidust performance of the PI/alumina coating. To assess this effect, the antidust performance test was repeated using dust samples with different surface charges and deposited onto coatings with different charge state. The results are presented in Figure 3.18, and they reveal a clear charge-dependent trend in dust adhesion.

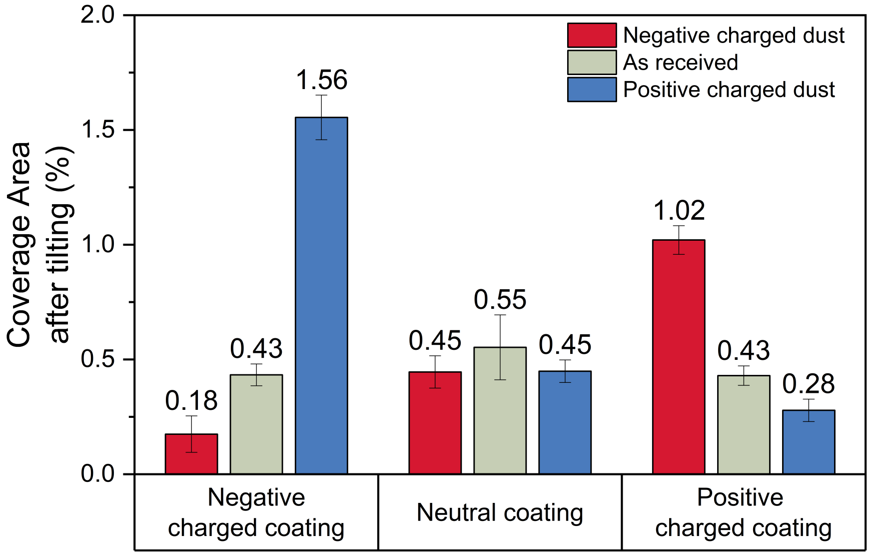

Figure 3.18: Coverage area after tilting of negative, neutral (as received) and positive charged dust on negative, neutral and positive PI/alumina coating.

When the dust and the coating were both negatively or positively charged, the **lowest coverage** values were recorded. Specifically, negatively charged dust on a negatively charged coating resulted in only 0.18% surface coverage, while positively charged dust on a positively charged coating led to 0.28% coverage.

In contrast, when the dust and the coating carried opposite charges, dust adhesion increased. The **highest coverage** area was observed for positively charged dust on a negatively charged coating, reaching 1.56%, while negatively charged dust on a positively charged coating led to 1.02% coverage.

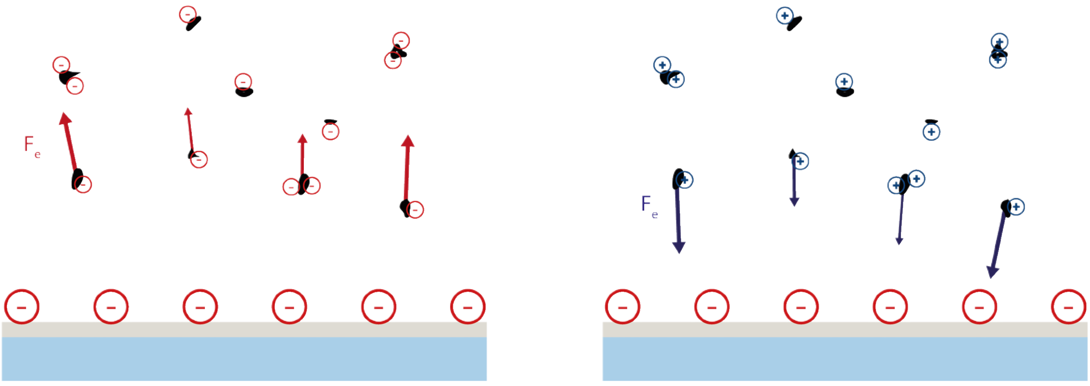

(a) Repulsive. **(b)** Attractive.

Figure 3.19: Diagram of the repulsive and attractive electrostatic force on the charged dust.

However, when only **one of the components** (either the dust or the coating) was charged, the resulting dust adhesion remained within the range of the neutral coating with neutral dust.

This suggests that charging only one of the interacting surfaces is insufficient to significantly alter adhesion.

Additionally, the magnitude of the charge effect appears to be greater for negatively charged coatings than for positively charged ones. This could be attributed to the different methods used to induce the charges. The physical charging method applied to achieve a negative charge on the coating may have resulted in a higher surface charge density compared to that of the chemical modification used for positive charging.

The surface energy measurements of the differently charged PI/alumina coatings, presented in Table 3.1, further support the hypothesis that electrostatic effects, rather than variations in surface energy, are responsible for the differences in dust adhesion observed in this test. The Lifshitz–van der Waals (γ_s^{LW}) component of surface energy remains nearly identical across all three coatings, indicating that the fundamental Van der Waals interactions between the coating and dust particles are not significantly altered by the charging process.

Table 3.1: Surface energy components of the negative, neutral and positive charged PI/alumina coating.

Surface	γ_l**[mN/m]**	γ_s^{LW}**[mN/m]**	γ_l^+**[mN/m]**	γ_l^-**[mN/m]**
PI/alumina coating (-)	35.04	34.28	1.18	0.12
PI/alumina coating	34.02	33.96	0.75	0.00
PI/alumina coating (+)	36.94	34.7	34.63	0.03

The total surface energy of the positively charged coating is higher than that of the neutral and negatively charged coatings. This difference arises primarily from the much higher electron acceptor component (γ_l^+), which likely results from the quaternization of the silane coupling agent at the surface. This chemical modification introduces stable, positively charged functional groups that affect the surface interaction properties. However, the negatively charged coating exhibits surface energy values nearly identical to the neutral sample. This suggests that the negative charges from the physical charging method dissipated during the contact angle measurements due to interactions with the test liquid and the moisture present in the laboratory environment.

All of this indicates that electrostatic repulsion plays a role in mitigating dust adhesion, supporting the hypothesis that a controlled charging strategy could be an effective way of enhancing antidust performance. By designing coatings that develop charge states aligned with those of the lunar dust, it may be possible to **reduce the accumulation of dust** on exposed surfaces in the Moon.

Ambient pressure vs vacuum

In lunar missions, dust interaction with equipment occurs in both pressurized cabins and the vacuum environment of the Moon's surface. Therefore, understanding how the presence of atmospheric moisture influences dust adhesion of the PI/alumina coating is also important. In this experiment, the previous antidust performance test was repeated under two conditions: ambient pressure (with the pump turned off) and vacuum (with the pump turned on). The laboratory environment had a recorded relative humidity of 30%. The results are presented in Figure 3.20 for negatively charged dust and Figure 3.21 for positively charged dust.

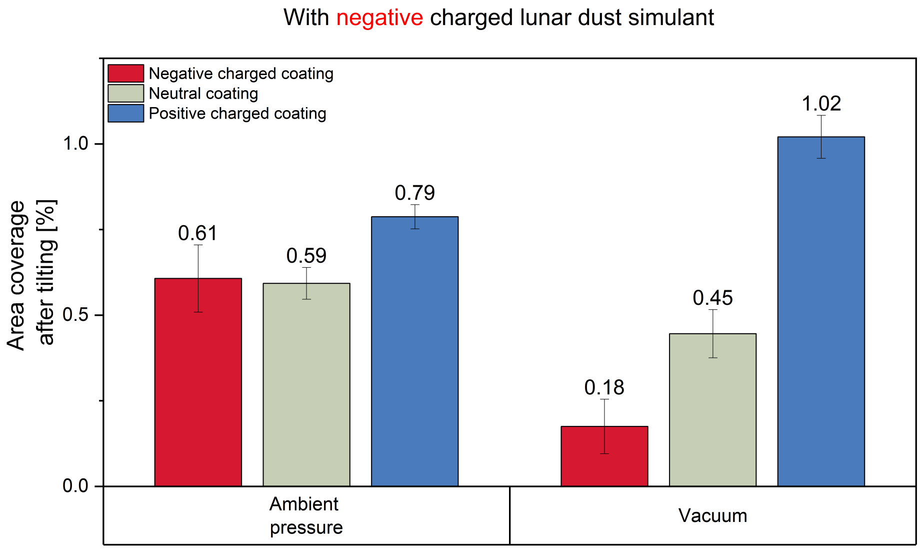

Figure 3.20: Coverage area after tilting of negative charged dust on negative, neutral and positive PI/alumina coating in ambient pressure and in vacuum.

The findings indicate that the previously observed electrostatic effect on dust adhesion is **reduced in ambient pressure**. In vacuum, **negatively charged dust** exhibited minimal adhesion on a negatively charged coating, with a coverage area of only 0.18%. However, when the same test was conducted in ambient conditions, the coverage area increased to 0.61%. Similarly, for neutral coatings, dust coverage rose from 0.45% in vacuum to 0.59% in ambient conditions. This suggests that the presence of moisture disrupts the charge-based repulsion mechanism that was effective in vacuum.

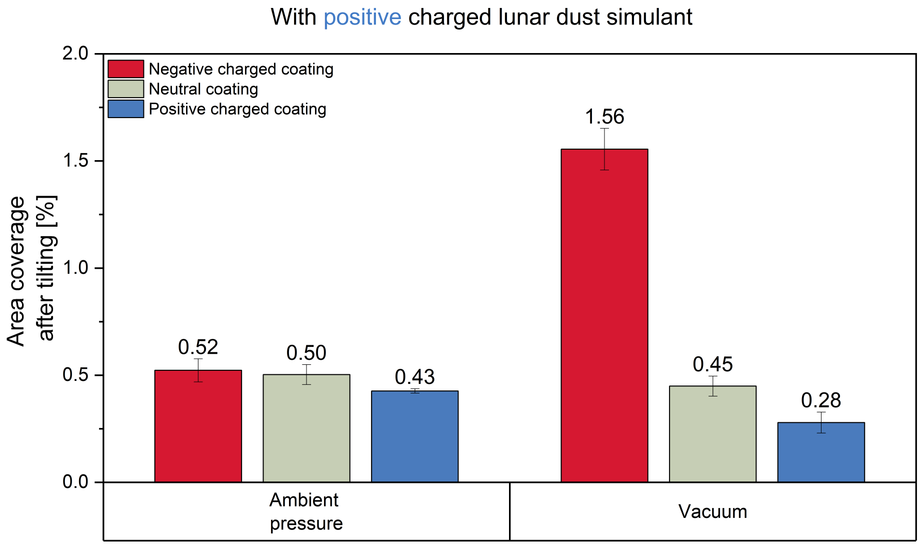

Figure 3.21: Coverage area after tilting of positive charged dust on negative, neutral and positive PI/alumina coating in ambient pressure and in vacuum.

Two main factors contribute to this effect. In ambient pressure, even with moderate humidity, water molecules present in the air provide a pathway for **charge dissipation**. This reduces the charges on both the dust and the coating, neutralizing the electrostatic forces responsible for repelling dust in vacuum. The presence of water molecules also introduces **capillary adhesion forces**, which become an additional mechanism for dust adhesion. These effects are illustrated in Figure 3.22.

The value of 0.79% of the negative dust on the positive coating in ambient pressure is lower than in vacuum but greater than on the negative and neutral coating. This can mean that the chemically bound positive charges on the coating remained more stable than the physically induced negative charges, leading to some attraction although less that in vacuum. On top of that, charge dissipation and capillary forces still contributed to increased dust adhesion.

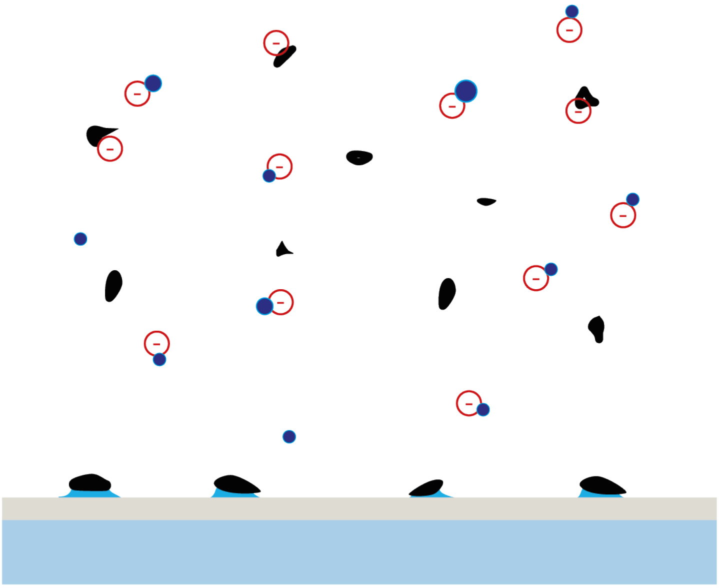

Figure 3.22: Diagram of the humidity effect on the electrostatic environment. The water molecules in the air cause charge dissipation and a water film at the surface of the sample promotes capillary effects.

For **positively charged dust**, the trends are reversed but follow the same logic.

This shows that although electrostatic repulsion can be an effective antidust strategy in vacuum, its **effectiveness is significantly reduced in the presence of atmospheric moisture**. This is particularly relevant in pressurized environments, such as those found in lunar habitats, where humidity control may be a factor.

3.3.2. Layer by layer erosion

To evaluate the durability and erosion behavior of the layer-by-layer coating, a controlled manual grinding test was performed using silicon carbide (SiC) paper #4000 (grain size 5 µm). The samples were ground in 15-second cycles until the aluminum 1060 substrate was fully exposed. The before and after of this process can be seen in Figure 3.23. After each grinding cycle, the antidust performance was measured. The results are displayed in Figure 3.24, showing the evolution of dust coverage after tilting as a function of grinding time.

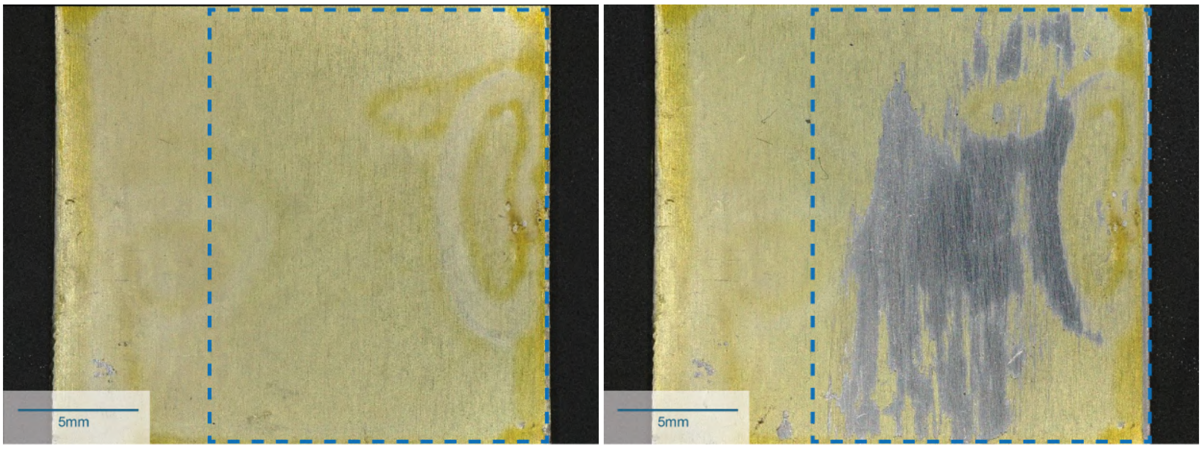

Figure 3.23: PI/alumina platelets coating on Al1060 before (left) and after (right) the manual grinding cycles. In blue is the area that was grinded.

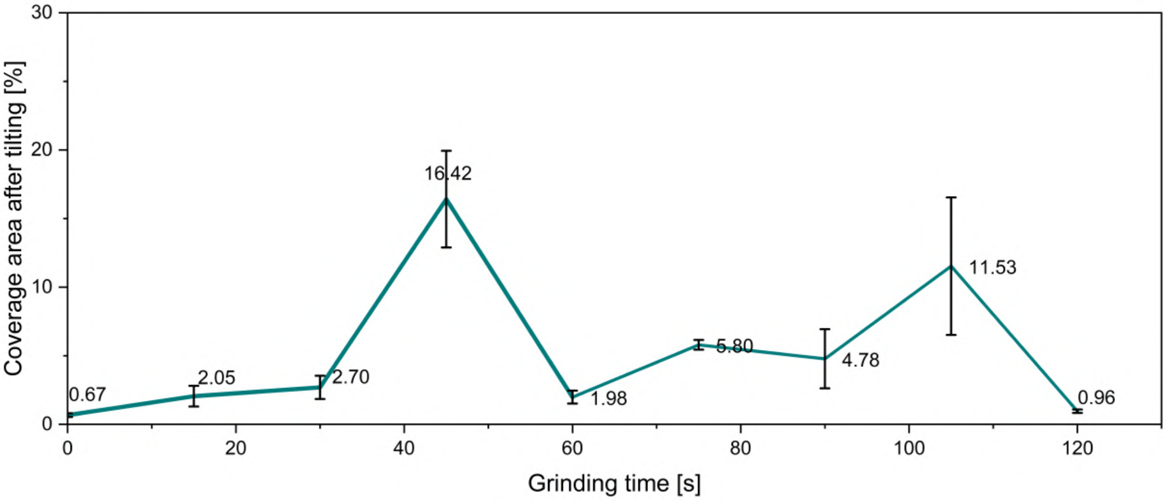

Figure 3.24: Coverage area after tilting of the PI/alumina particles coating after manual grinding.

The initial measurement, before grinding, showed a dust coverage of 0.67%. In the first two grinding cycles, this percentage **slightly increased**, as expected due to the removal of surface material. However, after 45 seconds of grinding, a sharp peak was observed, reaching a **maximum** of 16.42% dust coverage. This suggests that a different layer within the coating was exposed, which drastically increased dust adhesion.

After this peak, dust coverage **dropped significantly** to 1.98% in the next grinding cycle (60s), before **rising again** and reaching a second peak at 11.53% at 105s. Finally, after 8 grinding cycles (120s), the aluminum **substrate was reached**, and dust coverage dropped to 0.96%. It is relevant to notice that the dust coverage of what is expected to be the polyimide layers is higher than the previously reported 5.02% on the Al1060 coated with polyimide. This might be due to the higher roughness of the surface because of the grinding process, leading to more dust adhering to the rough polyimide layer.

This oscillating trend in dust adhesion is directly related to the layered structure of the coating, where alternating alumina and polyimide layers influence the surface properties. To confirm this hypothesis, SEM images were taken after 0s, 15s, 45s, 60s, and 90s of grinding (Figure 3.25).

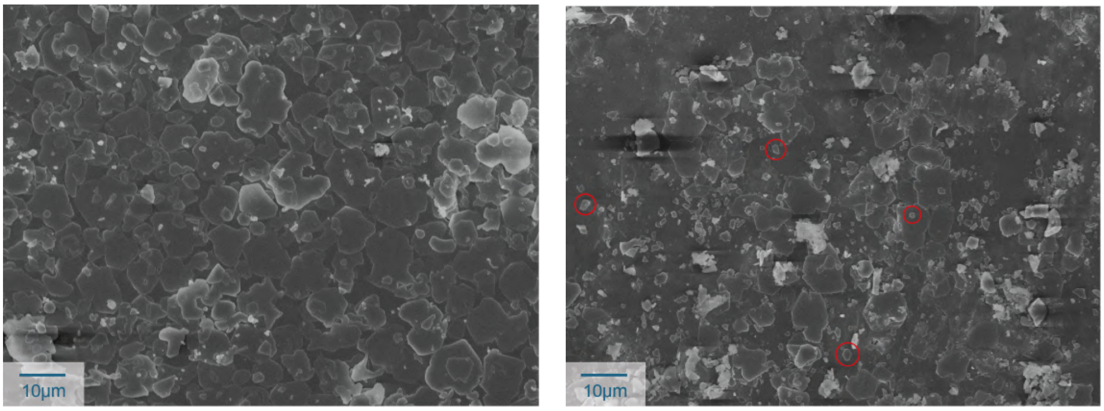

(a) 0s **(b)** 15s

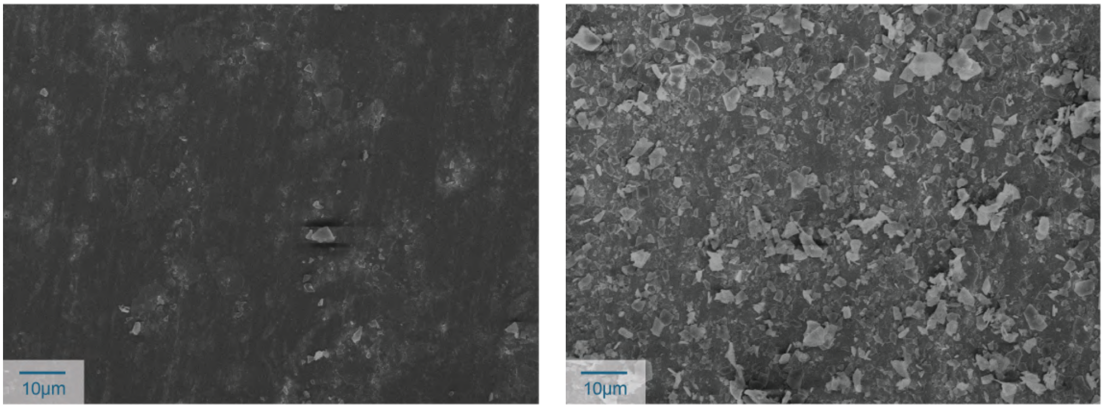

(c) 45s **(d)** 60s

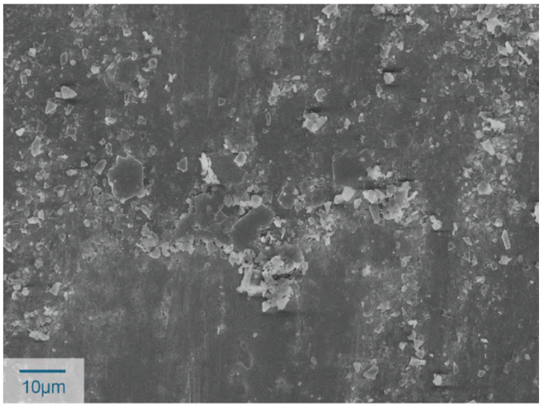

(e) 90s

Figure 3.25: SEM pictures of the surface of the coating after manual grinding at 0s, 15s, 45s, 60s, and 90s. Detail of the SiC particles from the SiC paper, in red. (Magnification: 1000x)

Initially, before any grinding **(0s)**, the coating exhibited an intact top layer of alumina platelets, which correlated with the low initial dust coverage observed in the antidust performance test. After **15 seconds** of grinding, a slight reduction in platelet coverage was evident, along with the presence of broken platelets. This alteration in the surface structure led to a small increase in dust adhesion, suggesting that damage to the alumina layer lightly compromised its antidust effect. At **45 seconds**, the SEM images revealed that the coating was nearly devoid of alumina platelets, indicating that the grinding process had reached the underlying polyimide layer. This transition corresponded to the sharp increase in dust coverage, as polyimide alone exhibits higher dust adhesion compared to the alumina. Following **60 seconds** of grinding, the number of alumina platelets increased again, although they appeared more fragmented than in the initial state. This partial restoration of the alumina layer reduced dust adhesion, reinforcing the role of platelets in maintaining the coating's antidust properties. By **90 seconds**, the surface displayed a heterogeneous mixture of both alumina and polyimide, leading to an intermediate dust adhesion value. This heterogeneous surface is probably due to the manual grinding that makes it difficult to mantain a homogeneus grinding of the surface. If we look back at the SEM pictured of the coating in chapter 2 it can also be seen that the first and second layers of alumina platelets are not completely horizontal to the substrate in some samples. This non-uniform layering could lead to inhomogeneous erosion, making the transition between alumina and polyimide layers more gradual and irregular.

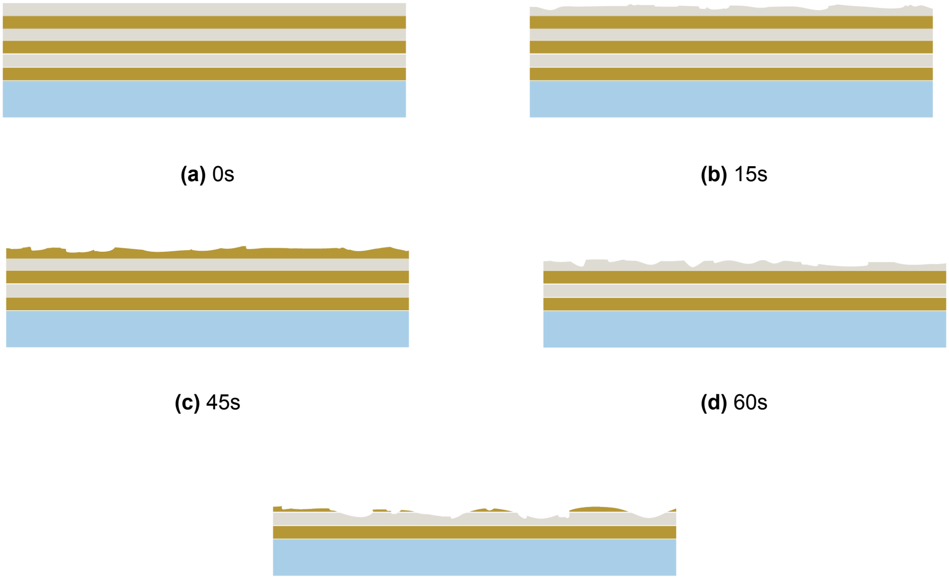

(a) 0s

(b) 15s

(c) 45s

(d) 60s

(e) 90s

Figure 3.26: Diagram of the erosion of the layer-by-layer coating.

Additional energy dispersive X-ray spectroscopy (EDS) analysis (see Appendix D) confirmed the presence of the silicon-containing particles in the samples after grinding, displayed in red. These are likely SiC particles from the grinding paper, which adhered to the coating surface during the test.

These observations are particularly relevant for the lunar environment, where micrometeoroid impacts, mechanical abrasion from dust transport, and astronaut activity can lead to progressive erosion of exposed surfaces. The results from the grinding test indicate that, although the erosion of the coating initially reduces its antidust performance, further wear can restore these properties as new alumina layers are exposed. The layer-by-layer structure can then extend thelifespan of the coating, providing a mechanism for self-renewing antidust protection over time.

3.3.3. UV effect

To evaluate the impact of UV radiation on the coating's antidust properties, samples were exposed to UV radiation, better simulating lunar surface conditions. This is particularly relevant as lunar dust and equipment are continuously subjected to high-intensity solar radiation, which includes UV wavelengths. The UV irradiation was performed using an OmniCure S1500 UV Curing System, which emits 27.7 W/cm² at the source. The spectral output ranges from 250 nm to 600 nm, covering UV to visible light, with higher intensity in the UVB and UVA regions. In general, the spectrum used for solar simulation is limited to the UV region, because it is assumed that the major degradation is due to these photons.[12].

The effect of UV exposure on dust adhesion was assessed by measuring the dust coverage after tilting at different exposure durations. The results are shown in Figure 3.27, where the initial dust coverage of 0.55% at 0 hours of UV exposure only slightly increased to 0.77% after 24 hours. This increase remains within the error margin, indicating that UV radiation **did not significantly affect** the antidust performance of the coating.

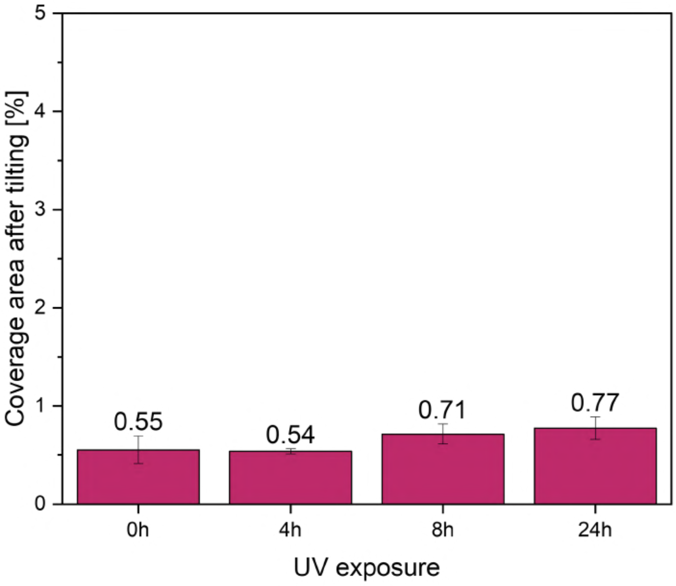

Figure 3.27: Coverage area after tilting of PI/alumina coating after UV exposure.

This stability is likely due to the high resistance of alumina platelets to UV degradation. Alumina is known for its chemical inertness and stability, which prevents structural changes that could influence the coating's antidust properties. Even after prolonged UV exposure, there was no significant degradation in the coating's ability to repel dust, reinforcing the idea that the layered alumina-polyimide structure provides UV resistance.

To further analyze the effect of UV exposure on the coating's chemical structure, FTIR spectroscopy was performed at the different exposure durations. The resulting spectra, shown in Figure 3.27, reveal that the characteristic polyimide (PI) peaks remain unchanged throughout the 24-hour UV exposure period.

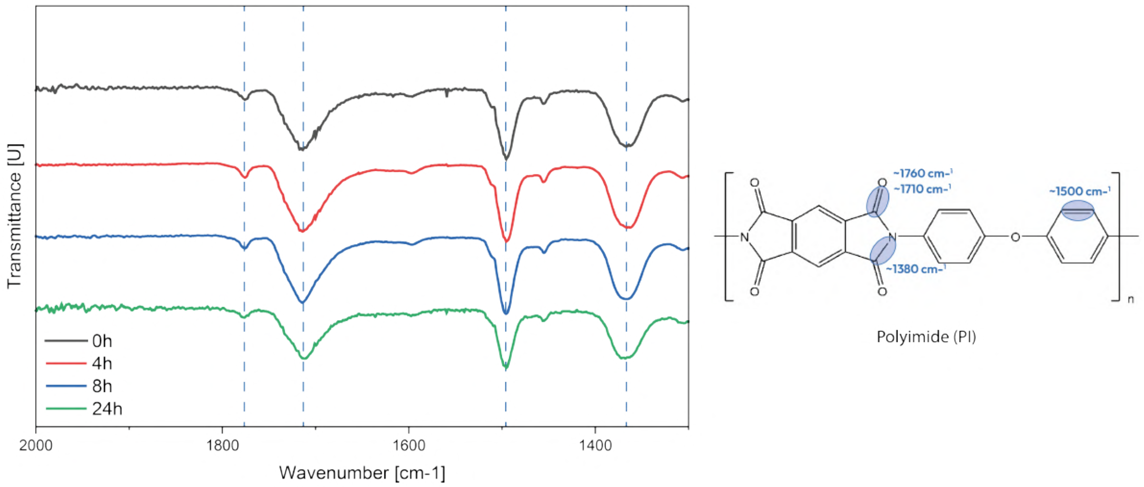

Figure 3.28: FTIR transmittance spectrum of the PI/alumina platelets coating after UV irradiation where the characteristic peaks of polyimide can be seen.

This result suggests that the polyimide matrix remains structurally stable, with no significant photodegradation occurring within the timeframe of the test. This is coherent with studies that show that UV radiation has not been shown to significantly affect the mechanical properties of polyimide films [42]. The alumina platelets embedded in the coating might be also acting as a protective barrier, preventing direct UV radiation from penetrating the polymer matrix. The shielding effect from alumina further enhances the coating's durability in the lunar environment.

3.4. Discussion

The various experimental tests conducted in this study provided a comprehensive understanding of the adhesion forces influencing dust particles in different environmental conditions. These tests allowed for an analysis of how van der Waals, electrostatic, and capillary forces contribute to dust adhesion and how they interact under conditions relevant to lunar missions.

Focusing on the performance of the polyimide/alumina platelets coating, it was observed that this coating exhibited the lowest dust coverage after tilting compared to other tested surfaces. One of the primary reasons for this result is the surface energy of the coating, which closely matches that of the lunar dust simulant. Since van der Waals forces are significantly influenced by the difference in surface energies between the dust and the surface, the similar energy values between the coating and the simulant resulted in a reduced adhesion force, thereby minimizing dust accumulation. However, this effect was further enhanced by the introduction of electrostatic repulsion. The ability to charge both the surface and the dust with the same polarity demonstrated a clear reduction in dust adhesion, reinforcing the idea that electrostatic repulsion is a viable antidust strategy. It is important to note that the magnitude of the electrostatic repulsion effect may have been underestimated in these laboratory tests due to the limitations of the vacuum conditions. The vacuum pressure achieved in the experimental setup was 1×10^{-3} bar, whereas the true lunar environment operates at an extreme vacuum level of $\tilde{3} \times 10^{-15}$ bar [34]. In such a hard vacuum, charging effects would be significantly more pronounced, and both the dust particles and the coated surface would retain more charge and for much longer durations.

In a real lunar scenario, a polyimide/alumina platelets-coated surface would charge similarly to the surrounding lunar dust, exhibiting positive charging during daylight due to photoionization and negative charging in darkness due to interaction with solar wind electrons. The same electrostatic levitation phenomenon observed when dust particles are lifted and transported by electrostatic forces, [1] could theoretically occur between this coating and the dust, preventing the dust from depositing on the surface. In cases where dust still manages to settle on the surface, the low van der Waals interaction between the dust particles and the coating would mean that even small tilting or vibrations could remove the particles with ease, even in the lower gravity environment of the Moon.

Beyond its antidust capabilities, the alumina component of the coating serves multiple protective roles. The hard alumina platelets protect the underlying polyimide matrix from the abrasive nature of lunar dust, which is known to cause mechanical wear and degradation of exposed materials. Additionally, alumina acts as a shield against UV radiation, preventing UV-induced degradation of the polymer. The stability of the coating under UV exposure, as demonstrated in the experiments, further supports its long-term viability in space applications.

Another critical aspect of this coating is its multilayer architecture, which provides a self-renewing antidust effect. Even if the top alumina layer is damaged due to mechanical wear, or surface scratches, subsequent alumina layers will be exposed, restoring the coating's antidust properties. The layer-by-layer structure ensures that as erosion occurs, fresh alumina platelets become available at the surface, maintaining both the antidust functionality and protective properties over time.

4

Conclusion and Recommendations

With the upcoming Artemis III mission, set to be the first crewed lunar landing since Apollo 17 in December 1972, there is a renewed drive for materials and technologies tailored for the harsh lunar environment. As astronaut Gene Cernan noted during the Apollo 17 Technical Debrief, ”dust is probably one of our greatest inhibitors to a nominal operation on the Moon.” Lunar dust presents a significant challenge for exploration and long-term human presence, leading to the need of innovative solutions such as antidust coatings to mitigate its effects.

This thesis set out to answer the research question: Can a layer-by-layer coating composed of polyimide and alumina platelets be developed with effective antidust properties for lunar applications? To do this, this question had to be broken down into different tasks. A systematic testing methodology was developed that used imaging techniques to enable the quantification of dust accumulation. This approach provided a reliable means of assessing the antidust performance of the coating under controlled conditions. Next, the study investigated how dust adhesion changes under different testing conditions. Experiments conducted under varying pressure and humidity, and electrostatic environments revealed that adhesion is highly dependent on external factors. These findings emphasized the importance of designing coatings specifically tailored for lunar conditions, where environmental influences play a critical role in dust behavior. Another crucial aspect examined was how to measure the material properties that influence dust adhesion. Different techniques were employed to assess surface roughness and surface energy. These analyses provided valuable insights into the key parameters that determine the interaction between dust particles and the coating surface. The durability of the layer-by-layer system was also explored to determine its effectiveness over prolonged use. Mechanical degradation tests demonstrated that the multilayer approach contributes to the longevity of the coating, making it more resistant to mechanical wear and environmental stressors. Finally, the study examined how the lunar environment affects the coating's antidust performance. Vacuum chamber experiments were conducted to replicate lunar conditions, particularly focusing on electrostatic interactions and vacuum. The results indicated that the electrostatic properties of the Moon could be leveraged to actively repel dust particles, reinforcing the feasibility of using charge-based repulsion as an antidust strategy.

This research presents a novel approach to lunar antidust coatings by integrating polyimide and alumina platelets in a layer-by-layer system. While the coating itself is not new, its application as an antidust solution is unprecedented. This study is the first to explore a dual strategy, combining composition matching with lunar dust and harnessing the Moon's electrostatic environment to actively repel particles. By aligning the surface properties of the coating with those of lunar regolith, dust adhesion due to van der Waals forces is minimized, while electrostatic repulsion further reduces accumulation.

Another key part of this research was the development of a custom vacuum chamber setup and test procedure, specifically designed to simulate lunar conditions. The experimental methodology, including controlled pressure, charge manipulation, and tilting tests, allowed for systematic evaluation of the coating's antidust performance in a realistic, low-pressure environment. This unique setup provides a valuable framework for future antidust research, enabling consistent and repeatable testing of coatings and materials intended for lunar applications.

4.1. Recommendations for future research

While this study has demonstrated the potential of a polyimide/alumina platelet coating as an effective antidust solution for lunar applications, further research is needed to refine and expand upon these findings.

Testing in a More Realistic Lunar Environment

One of the primary limitations of this study was the vacuum level achieved during testing. The experiments were conducted at 1×10^{-3} bar, which, while lower than Earth's atmospheric pressure, does not fully replicate the extreme vacuum conditions of the lunar surface (3×10^{-15} bar). Additionally, temperature variations should be incorporated into the testing setup. On the Moon, surface temperatures can reach 121°C during the day and drop to -133°C at night [56]. This extreme thermal cycling could influence the mechanical properties of the coating, potentially affecting its structural integrity and antidust performance. Future experiments should then include a high-vacuum chamber and temperature-controlled conditions to assess the durability of the coating under a better-simulated lunar environment.

Expanding the Layer-by-Layer Architecture

The layered structure of the coating has shown promise in extending the lifespan of its antidust functionality, as new alumina layers are gradually exposed during erosion. However, this study tested only a limited number of layers. Future research should investigate the effects of adding more layers to determine whether the structure remains consistent and whether additional layers further improve self-renewing antidust performance.

Quantifying Triboelectric Charging

The triboelectric charging behavior of the coating should be further analyzed. While this study demonstrated that electrostatic repulsion plays a key role in dust mitigation, future work should aim to quantify the charge aquired during the triboelectric charging of the dust. This would further solidify that the recorded changes in dust coverage are due to the charges on the particles. This can be achieved by measuring the charge on individual particles using a Faraday cup.

Extended UV Exposure Testing

While the UV tests conducted in this study demonstrated that the coating remains stable after 24 hours of UV exposure, the Moon experiences continuous sunlight for much longer periods. A lunar day (from sunrise to sunset) lasts approximately 14 Earth days, meaning that surfaces on the Moon are exposed to prolonged UV radiation. Extended UV tests should reflect this to assess whether prolonged exposure alters the coating's structure or degrades its antidust performance over time.

Optimization of the Polyimide/LMS-1 Particles Coating

The polyimide/LMS-1 particles coating, manufactured in this study as an alternative to the alumina platelet-based coating, requires further optimization. The lack of a clearly defined layered structure suggests that the deposition process needs refinement to improve the distribution of the lunar simulant particles within the polymer matrix. Despite this, the high inorganic content of this coating presents an exciting opportunity for In-Situ Resource Utilization (ISRU) by reducing reliance on Earth-supplied materials.

The concept of ISRU refers to the processing and utilization of local extraterrestrial resources, such as lunar regolith, to produce materials and consumables that would otherwise need to be transported from Earth. Transporting 1 kg of payload to the Moon requires launching 7.5 to 11 kg into Earth orbit, significantly increasing mission costs and complexity. Since lower mass requirements lead to fewer launches, ISRU can help reduce launch frequencies, which also decreases mission risk by minimizing the number of complex and costly launches. A local supply of critical consumables can also increase mission longevity by eliminating the need to wait for Earth-based resupply missions [4].

While commercial rockets have significantly reduced launch costs, transporting large amounts of materials remains expensive. Falcon Heavy can launch 63,800 kg to LEO for $97 million, resulting in a a cost of $1.52k/kg [26]. Although the cost per kilogram for launching mass to orbit has declined over time, for long-duration or permanent lunar operations, harnessing lunar resources will ultimately be more efficient. By incorporating lunar regolith into antidust coatings, ISRU could provide a sustainable and cost-effective approach to mitigating dust-related challenges in lunar environments.

References

[1] M M Abbas et al. *Planetary and Space Science, 2007, in press LUNAR DUST CHARGING BY PHOTOELECTRIC EMISSIONS*. Tech. rep.

[2] Phillip B Abel et al. *Lunar Dust Mitigation: A Guide and Reference First Edition (2021)*. Tech. rep. 2023. URL: `http://www.sti.nasa.gov`.

[3] Nima Afshar-Mohajer et al. "Review of dust transport and mitigation technologies in lunar and Martian atmospheres". In: *Advances in Space Research* 56.6 (Sept. 2015), pp. 1222–1241. ISSN: 18791948. DOI: `10.1016/j.asr.2015.06.007`.

[4] Koorosh R Araghi. *NASA Lunar In-Situ Resource Utilization Technology Overview*. Tech. rep. 2022.

[5] C. Bandl et al. "Functionalization of PTFE substrates with quaternary ammonium groups – An approach towards anion conducting properties". In: *Applied Surface Science* 661 (July 2024). ISSN: 01694332. DOI: `10.1016/j.apsusc.2024.160084`.

[6] W. Barthlott and C. Neinhuis. "Purity of the sacred lotus, or escape from contamination in biological surfaces". In: *Planta* 202.1 (Apr. 1997), pp. 1–8. ISSN: 0032-0935. DOI: `10.1007/s004250050096`.

[7] Lorenz J. Bonderer et al. "Strong and ductile platelet-reinforced polymer films inspired by nature: Microstructure and mechanical properties". In: *Journal of Materials Research* 24.9 (Sept. 2009), pp. 2741–2754. ISSN: 08842914. DOI: `10.1557/jmr.2009.0340`.

[8] R. Allen Bowling. "An Analysis of Particle Adhesion on Semiconductor Surfaces". In: *Journal of The Electrochemical Society* 132.9 (Sept. 1985), pp. 2208–2214. ISSN: 0013-4651. DOI: `10.1149/1.2114320`.

[9] Kevin M. Cannon et al. "Working with lunar surface materials: Review and analysis of dust mitigation and regolith conveyance technologies". In: *Acta Astronautica* 196 (July 2022), pp. 259–274. ISSN: 00945765. DOI: `10.1016/j.actaastro.2022.04.037`.

[10] Wenjuan Chen et al. "Thermal imidization process of polyimide film: Interplay between solvent evaporation and imidization". In: *Polymer* 109 (Jan. 2017), pp. 205–215. ISSN: 00323861. DOI: `10.1016/j.polymer.2016.12.037`.

[11] Morton Corn. "The adhesion of solid particles to solid surfaces, i. a review". In: *Journal of the Air Pollution Control Association* 11.11 (1961), pp. 523–528. ISSN: 00022470. DOI: `10.1080/00022470.1961.10468032`.

[12] Lucas F M Da Silva, Andreas Öchsner, and Robert D Adams. *Handbook of Adhesion Technology*. Tech. rep. 2018.

[13] Chiaramonti Debay. *Moon Dust Micrographs*. Jan. 2017.

[14] Dino-Lite. *Dino-Lite Digital Microscopes Specifications*. 2024.

[15] Adrienne Dove et al. “Mitigation of lunar dust adhesion by surface modification”. In: *Planetary and Space Science* 59.14 (Nov. 2011), pp. 1784–1790.

[16] Ayoub El Baraka et al. “Assessment of dust adhesion forces on the hydrophilic/hydrophobic glasses at two representative CSP sites in Morocco”. In: *Journal of Coatings Technology and Research* 20.1 (Jan. 2023), pp. 403–412. ISSN: 19353804. DOI: `10.1007/s11998-022-00681-3`.

[17] Hartmut R Fischer. “In-situ resource utilization–feasibility of the use of lunar soil to create structures on the moon via sintering based additive manufacturing technology”. In: *Aeronautics and Aerospace Open Access Journal* 2.4 (Aug. 2018). DOI: `10.15406/aaoaj.2018.02.00056`.

[18] Reiner Fürstner et al. “Wetting and Self-Cleaning Properties of Artificial Superhydrophobic Surfaces”. In: *Langmuir* 21.3 (Feb. 2005), pp. 956–961. ISSN: 0743-7463. DOI: `10.1021/la0401011`.

[19] James R Gaier et al. *Evaluation of Surface Modification as a Lunar Dust Mitigation Strategy for Thermal Control Surfaces*. Tech. rep. 2011. URL: `http://www.sti.nasa.gov`.

[20] L. A. Girifalco and R. J. Good. “A Theory for the Estimation of Surface and Interfacial Energies. I. Derivation and Application to Interfacial Tension”. In: *The Journal of Physical Chemistry* 61.7 (July 1957), pp. 904–909. ISSN: 0022-3654. DOI: `10.1021/j150553a013`.

[21] Mihir Gondhalekar et al. *Mitigation and Prevention of Lunar Dust on NASA Artemis xEMU Spacesuits Final Report*. Tech. rep. 2020.

[22] Robert J. Good and Carel J. van Oss. “The Modern Theory of Contact Angles and the Hydrogen Bond Components of Surface Energies”. In: *Modern Approaches to Wettability*. Boston, MA: Springer US, 1992, pp. 1–27. DOI: `10.1007/978-1-4899-1176-6{\_}1`.

[23] Li Hsia Yeo et al. “Laboratory Investigations of Triboelectric Charging of Dust by Rover Wheels”. In: *Advances in Space Research xx* (2023). DOI: `10.1016/j.jasr.xxxx.xx.xxx`. URL: `www.sciencedirect.comwww.elsevier.com/locate/asr`.

[24] Rima J. Isaifan et al. “Evaluation of the adhesion forces between dust particles and photovoltaic module surfaces”. In: *Solar Energy Materials and Solar Cells* 191 (Mar. 2019), pp. 413–421. ISSN: 09270248. DOI: `10.1016/j.solmat.2018.11.031`.

[25] Jacob N. Israelachvili. “Van der Waals Forces between Particles and Surfaces”. In: *Intermolecular and Surface Forces*. Elsevier, 2011, pp. 253–289. DOI: `10.1016/b978-0-12-375182-9.10013-2`.

[26] Harry W Jones. *Take Material to Space or Make It There?* Tech. rep.

[27] Robert Jones et al. “Adhesion Forces between Glass and Silicon Surfaces in Air Studied by AFM: Effects of Relative Humidity, Particle Size, Roughness, and Surface Treatment”. In: *Langmuir* 18.21 (Oct. 2002), pp. 8045–8055. ISSN: 0743-7463. DOI: `10.1021/la0259196`.

[28] H. Krupp. “Particle adhesion theory and experiment”. In: *Advances in Colloid and Interface Science* 1.2 (May 1967), pp. 111–239. ISSN: 00018686. DOI: `10.1016/0001-8686(67)80004-6`.

[29] Kruss. *Oss and Good method*. 2024. URL: `https://www.kruss-scientific.com/en/know-how/glossary/oss-and-good-method`.

[30] Abhijith Kunneparambil Sukumaran et al. “Recent trends in tribological performance of aerospace materials in lunar regolith environment – A critical review”. In: *Advances in Space Research* 73.1 (Jan. 2024), pp. 846–869. ISSN: 18791948. DOI: `10.1016/j.asr.2023.10.039`.

[31] Mathilde Laot et al. “Additive Manufacturing and Spark Plasma Sintering of Lunar Regolith for Functionally Graded Materials”. In: *Spool* 8.2 (Sept. 2021), pp. 7–29. ISSN: 22150900. DOI: `10.7480/spool.2021.2.5258`.

[32] Samuel S. Lee et al. “Engineering Large-Area Antidust Surfaces by Harnessing Interparticle Forces”. In: *ACS Applied Materials and Interfaces* 15.10 (Mar. 2023), pp. 13678–13688. ISSN: 19448252. DOI: `10.1021/acsami.2c19211`.

[33] J. Lesage et al. “A model to determine the surface hardness of thin films from standard micro-indentation tests”. In: *Thin Solid Films* 497.1-2 (Feb. 2006), pp. 232–238. ISSN: 00406090. DOI: `10.1016/j.tsf.2005.09.194`.

[34] Joel S Levine. *Perturbing the Mass and Composition of the Lunar Atmosphere During the Artemis Surface Missions*. Tech. rep. 2011.

[35] Jared M Long-Fox et al. *Geomechanical Properties of Lunar Regolith Simulants LHS-1 and LMS-1*. Tech. rep. 2023. URL: `https://www.elsevier.com/open-access/userlicense/1.0/`.

[36] L. Lorenz et al. “Indentation modulus extrapolation and thickness estimation of ta-C coatings from nanoindentation”. In: *Journal of Materials Science* 56.33 (Nov. 2021), pp. 18740–18748. ISSN: 15734803. DOI: `10.1007/s10853-021-06448-2`.

[37] Kavya K. Manyapu et al. “Proof of concept demonstration of novel technologies for lunar spacesuit dust mitigation”. In: *Acta Astronautica* 137 (Aug. 2017), pp. 472–481. ISSN: 00945765. DOI: `10.1016/j.actaastro.2017.05.005`.

[38] M L Maurer et al. *Characterization of polyimide via FTIR analysis FTIR ANALYSIS OF POLYIMIDE 1 CHARACTERIZATION OF POLYIMIDE VIA FTIR ANALYSIS*. Tech. rep. 2014.

[39] Olympus IMS. *Surface Roughness Measurement—Parameters*. 2024. URL: `https://evidentscientific.com/en/applications/metrology/surface-roughness-measurement-portal/parameters#!cms%5Bfocus%5D=023`.

[40] Manuel Palencia. “Surface free energy of solids by contact angle measurements.” In: *Journal of Science with Technological Applications* 2 (May 2017), pp. 84–93. ISSN: 0719-8647. DOI: `10.34294/j.jsta.17.2.17`. URL: `https://www.jsta.cl/resource?doi=j.jsta.17.2.17`.

[41] Jouko Peltonen et al. “Topographical Parameters for Specifying a Three-Dimensional Surface”. In: *Langmuir* 20.22 (Oct. 2004), pp. 9428–9431. ISSN: 0743-7463. DOI: `10.1021/la0400252`.

[42] Elena A. Plis et al. “Review of Radiation-Induced Effects in Polyimide”. In: *Applied Sciences* 9.10 (May 2019), p. 1999. ISSN: 2076-3417. DOI: `10.3390/app9101999`.

[43] Yun Yun Quan et al. “Self-cleaning of Surfaces: The role of surface wettability and dust types”. In: *Scientific Reports* 6 (Dec. 2016). ISSN: 20452322. DOI: `10.1038/srep38239`.

[44] Yakov I Rabinovich et al. “Capillary forces between surfaces with nanoscale roughness”. In: *Advances in Colloid and Interface Science* 96.1-3 (Feb. 2002), pp. 213–230. ISSN: 00018686. DOI: `10.1016/S0001-8686(01)00082-3`.

[45] Yakov I. Rabinovich et al. “Adhesion between nanoscale rough surfaces. I. Role of asperity geometry”. In: *Journal of Colloid and Interface Science* 232.1 (Dec. 2000), pp. 10–16. ISSN: 00219797. DOI: `10.1006/jcis.2000.7167`.

[46] Hussein Kh Rasheed and Aseel A. Kareem. “The potential barrier and thermal stability dependence on PI thickness of AL/PI/C-SI schottky diode”. In: *Iraqi Journal of Science* 61.12 (Dec. 2020), pp. 3235–3241. ISSN: 23121637. DOI: `10.24996/ijs.2020.61.12.12`.

[47] Paramjit Singh et al. “High dose gamma radiation exposure upon Kapton-H polymer for modifications of optical, free volume, structural and chemical properties”. In: *Optik* 205 (Mar. 2020), p. 164244. ISSN: 00304026. DOI: `10.1016/j.ijleo.2020.164244`.

[48] T J Stubbs, R R Vondrak, and W M Farrell. *IMPACT OF LUNAR DUST ON THE EXPLORATION INITIATIVE*. Tech. rep.

[49] T. J. Stubbs et al. “Dependence of lunar surface charging on solar wind plasma conditions and solar irradiation”. In: *Planetary and Space Science* 90 (Jan. 2014), pp. 10–27. ISSN: 00320633. DOI: `10.1016/j.pss.2013.07.008`.

[50] Suprapedi, Muljadi, and Priyo Sardjono. “The characterization of ceramic alumina prepared by using additive glass beads”. In: *IOP Conference Series: Materials Science and Engineering*. Vol. 299. 1. Institute of Physics Publishing, Feb. 2018. DOI: `10.1088/1757-899X/299/1/012043`.

[51] Carel J. Van Oss, Manoj K. Chaudhury, and Robert J. Good. “Interfacial Lifshitz-van der Waals and polar interactions in macroscopic systems”. In: *Chemical Reviews* 88.6 (Sept. 1988), pp. 927–941. ISSN: 0009-2665. DOI: `10.1021/cr00088a006`.

[52] Otis R Walton. *Adhesion of Lunar Dust*. Tech. rep. 2007. URL: `http://www.sti.nasa.gov`.

[53] Liyong Wang et al. *Progress in Studies of Surface Nanotextures and Coatings with Nanomaterials on Glass for Anti-Dust Functionality*. Oct. 2022. DOI: `10.3390/nano12203677`.

[54] Xiao Wang et al. “Lunar Dust-Mitigation Behavior of Aluminum Surfaces with Multiscale Roughness Prepared by a Composite Etching Method”. In: *ACS Applied Materials & Interfaces* 14.29 (July 2022), pp. 34020–34028. ISSN: 1944-8244. DOI: `10.1021/acsami.2c07237`.

[55] Robert N. Wenzel. “RESISTANCE OF SOLID SURFACES TO WETTING BY WATER”. In: *Industrial & Engineering Chemistry* 28.8 (Aug. 1936), pp. 988–994. ISSN: 0019-7866. DOI: `10.1021/ie50320a024`.

[56] J.-P. Williams et al. “The global surface temperatures of the Moon as measured by the Diviner Lunar Radiometer Experiment”. In: *Icarus* 283 (Feb. 2017), pp. 300–325. ISSN: 00191035. DOI: `10.1016/j.icarus.2016.08.012`.

[57] Zhiqing Wu et al. “Preparation and Performance Characterization of Exploding Foil Initiator Based on ODPA-ODA Polyimide Flyer”. In: *Polymers* 14.21 (Nov. 2022). ISSN: 20734360. DOI: `10.3390/polym14214604`.

[58] Minglei Yang et al. “Research on the preparation and performance of anti-dust self-cleaning film on Mars dusty environment”. In: *Journal of Vacuum Science & Technology A* 40.1 (Jan. 2022). ISSN: 0734-2101. DOI: `10.1116/6.0001346`.

[59] Philipp Zanon, Michelle Dunn, and Geoffrey Brooks. “Current Lunar dust mitigation techniques and future directions”. In: *Acta Astronautica* 213 (Dec. 2023), pp. 627–644. ISSN: 00945765. DOI: `10.1016/j.actaastro.2023.09.031`.

A

Contact Angle

For the different surfaces studied, contact angles with the liquids diiodomethane, ethylene glycol and water were calculated. For the samples of the coating made with LMS-1 particles the droplets of ethylene glycol were not stable enough to perform measurements, probably due to the low surface tension of the liquid and the roughness of the surface. Glycerol was used as the third test liquid instead for these surfaces.

Table A.1: Contact angle of the different test liquids on the different surfaces.

Surface	**Contact Angle (º)**		
	Diiodomethane	**Ethylene Glycol/ Glycerol***	**Water**
Aluminium 1060	46.56 ± 0.31	62.69 ± 0.19	70.09 ± 0.52
Aluminium 1060 (not cleaned)	42.12 ± 0.54	56.53 ± 0.69	76.20 ± 0.63
Anodized aluminium	51.54 ± 0.99	25.53 ± 1.52	80.75 ± 0.75
PEEK	40.54 ± 0.53	40.04 ± 0.49	67.60 ± 0.80
ZrB2	40.79 ± 0.85	45.68 ± 0.98	70.22 ± 0.54
Polyimide	45.7 ± 0.93	40.33 ± 1.00	73.41 ± 1.33
PI/alumina coating	50.50 ± 0.73	68.47 ± 0.57	97.35 ± 1.25
PI/alumina coating (+)	49.14 ± 1.20	43.57 ± 0.68	51.70 ± 0.20

Continued on next page

Table A.1: Contact angle of the different test liquids on the different surfaces. (Continued)

PI/alumina coating (-)	49.94 ± 1.16	61.51 ± 1.47	92.86 ± 0.82
PI/LMS-1 coating	49.01 ± 0.83	80.09* ± 2.41	98.22 ± 1.41
PI/LMS-1 coating (polished)	49.40 ± 0.35	70.07 ± 1.31	98.14 ± 0.33
LMS-1 (SPS)	49.66 ± 0.34	50.45 ± 0.81	60.09 ± 1.89

B

Indentation results analysis

As described in chapter 2 the thickness of the coating and the effect of the substrate needed to be accounted for to calculate the hardness and the indentation modulus of the PI/alumina coating. The following chapter describes the methods used.

B.1. Hardness

Lesage et al. (2006) [33] proposed a model to determine the surface hardness of thin films from standard micro-indentation tests. It is based on the idea that when plotting the composite hardness as a function of the ratio of the film thickness to the diagonal of the indent ($\frac{t}{d}$), the values have an upper (H_{CU}) and lower bound (H_{CL}) that can be represented as follows:

$$H_{\mathsf{CU}} = H_{\mathsf{S}} + f\left(\frac{t}{d}\right) \cdot (H_{\mathsf{F}} - H_{\mathsf{S}}) \tag{B.1}$$

$$\frac{1}{H_{\mathsf{CL}}} = \frac{1}{H_{\mathsf{S}}} + f\left(\frac{t}{d}\right) \cdot \left(\frac{1}{H_{\mathsf{F}}} - \frac{1}{H_{\mathsf{S}}}\right) \tag{B.2}$$

with H_{F} being the film hardness and H_{S} being the substrate hardness.

The composite hardness combines both relationships in this way:

$$H_{\mathsf{C}} = H_{\mathsf{CL}} + f\left(\frac{t}{d}\right) \cdot (H_{\mathsf{CU}} - H_{\mathsf{CL}}) \tag{B.3}$$

Using $f = \left(\frac{t}{d}\right)^m$, the value of m is obtained through linear regression by plotting diagonal of the indentation as a function of the applied load during indentation in bilogarithmic coordinate as seen in Figure B.1:

$$\ln d = m \cdot \ln P + b \tag{B.4}$$

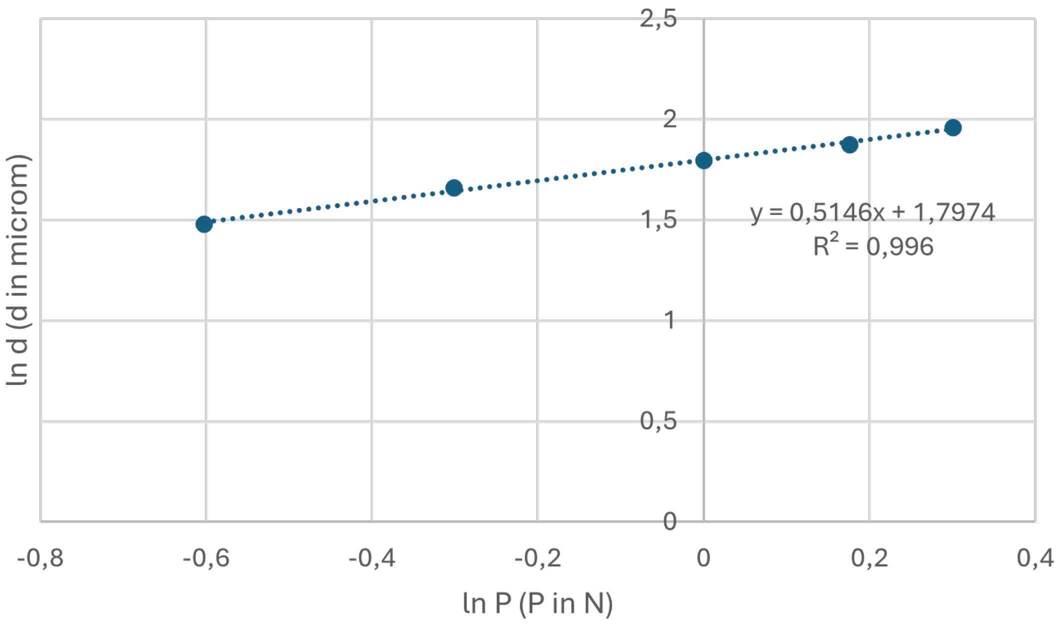

Figure B.1: Relation between indent diagonal, d, and applied load, P, in bilogarithmic coordinates for the PI/alumina coating on an aluminium 1060 substrate.

The composite hardness is then expressed as such:

$$\begin{aligned} H_{\mathsf{C}} =& (1-f)/\left(1/H_{\mathsf{S}} + f \cdot \left(\frac{1}{H_{\mathsf{F}}} - \frac{1}{H_{\mathsf{S}}}\right)\right) \\ &+ f \cdot (H_{\mathsf{S}} + f \cdot (H_{\mathsf{F}} - H_{\mathsf{S}})) \end{aligned} \tag{B.5}$$

Rewriting this equation in terms of H_F, allows us to calculate the film hardness. The hardness in SI units can be obtained from the Vickers hardness number (in kilograms-force per square millimeter [kgf/mm^2]) using the following relation:

$$\text{hardness (GPa)} = \frac{g_0}{1000} HV = \frac{9.80665}{1000} HV \tag{B.6}$$

The measured values of hardness of the coating and substrate together (H_C), the measured hardness of the substrate (H_S) and the calculated hardness of the PI/alumina coating ((H_F)) are in Table B.1:

Table B.1: Measured hardness of the composite and substrate and calculated film hardness at the different indentation loads.

Hardness [GPa]	**Applied load (mN)**				
	250	**500**	**1000**	**1500**	**2000**
H_C	0.507 ± 0.017	0.416 ± 0.011	0.441 ± 0.022	0.462 ± 0.015	0.392± 0.012
H_S	0.452 ± 0.022	0.427 ± 0.010	0.467 ± 0.006	0.411 ± 0.022	0.403 ± 0.021
H_F	0.592 ± 0.017	0.398 ± 0.011	0.384 ± 0.022	0.649 ± 0.015	0.360 ± 0.012

B.2. E_{IT}

To calculate the indentation modulus of the coating, it is necessary to measure it at varying indentation loads and then extrapolate to a zero load. We followed the recommendation of the standard ISO 14577-4:2016 to use a linear extrapolation. An exponential and a sigmoid fitting [36] were also explored as seen in Figure B.2.

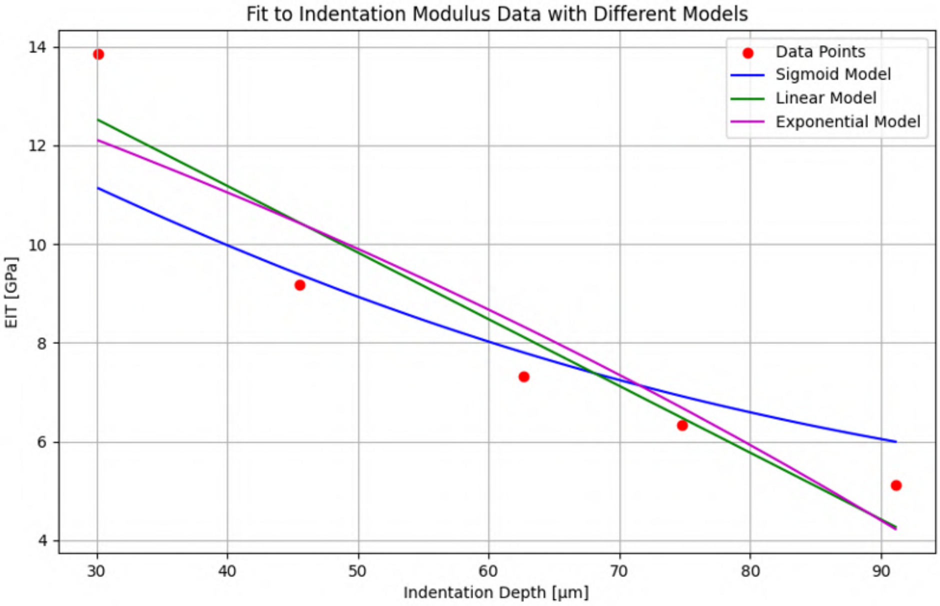

Figure B.2: Indentation modulus as a function of the maximum indentation depth and fitting models explored.

The linear fit achieved the best fitting with an R^2 of 0.8984 and thus the calculated E_{IT}=16.59 ± 0,27 GPa.

C

Vacuum Chamber Drawing

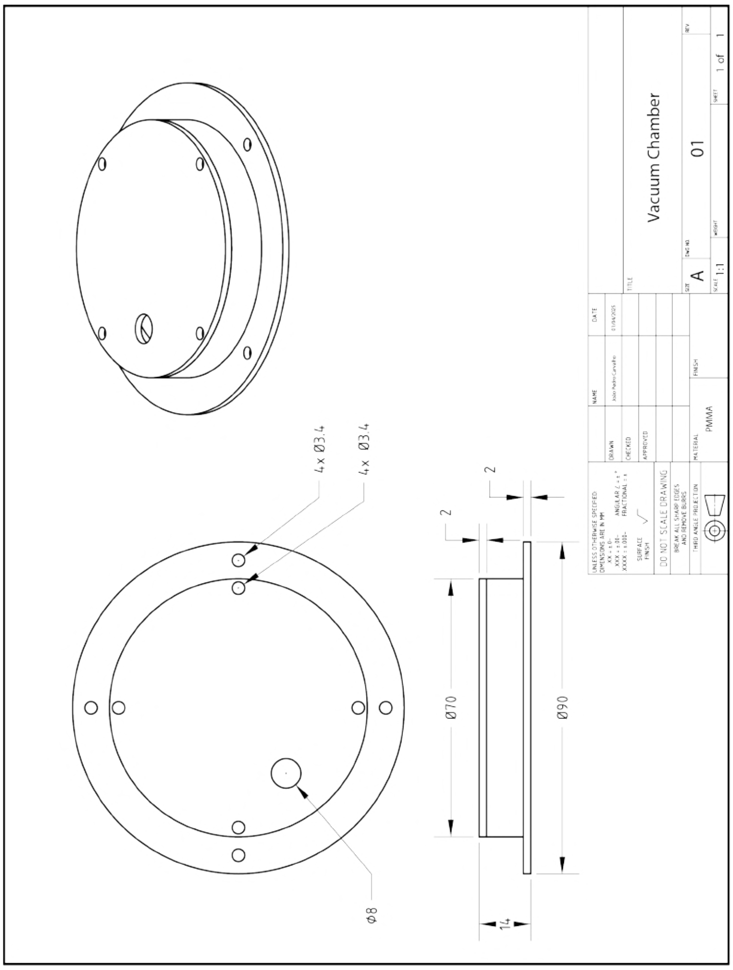

Figure C.1: Technical drawing of the in-house built vacuum chamber. The drawing is not to scale due to formatting of the document.

D

EDS results

D.1. Polyimide/LMS-1 particles coating

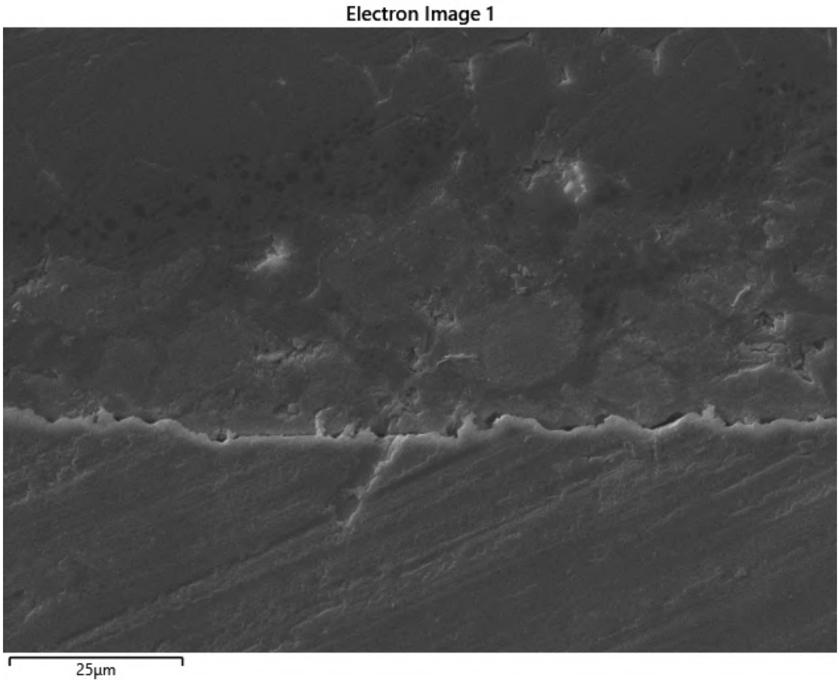

Figure D.1: SEM pictures of the cross section of the coating with polyimide/LMS-1 particles. Magnification:1000x

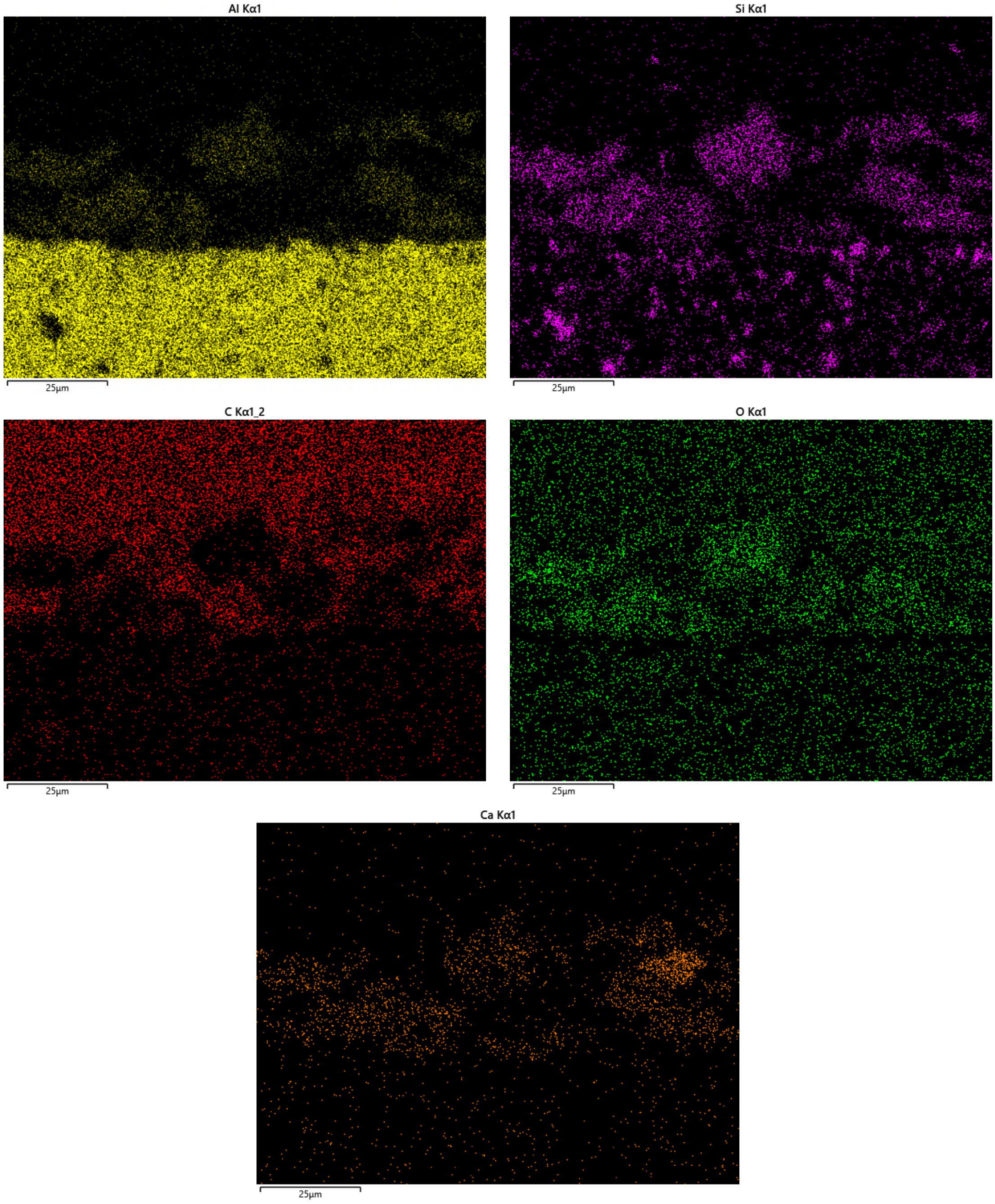

Figure D.2: Energy dispersive x-ray spectroscopy (EDS) map spectra of different elements for the SEM picture above.

D.2. Erosion

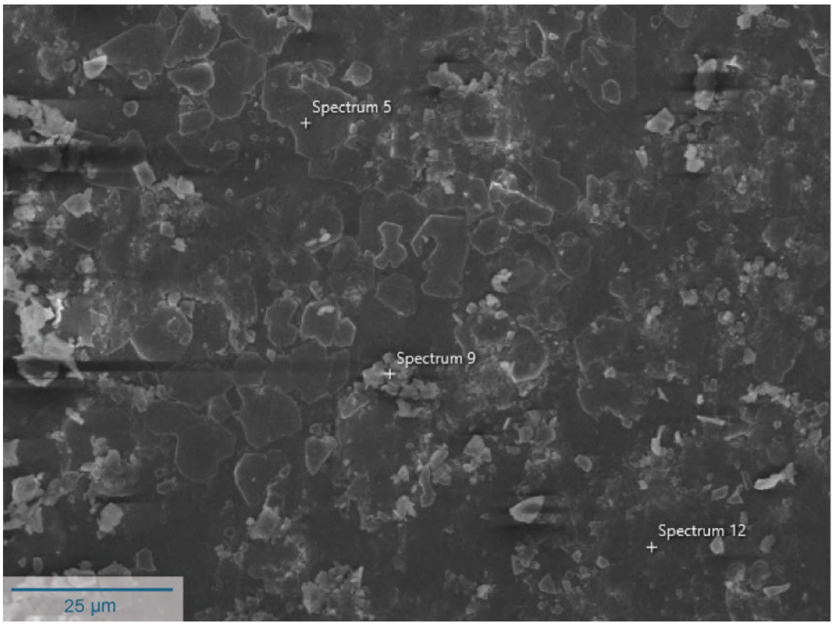

Figure D.3: SEM pictures of the surface of the coating after manual grinding for 15s. Magnification:1000x

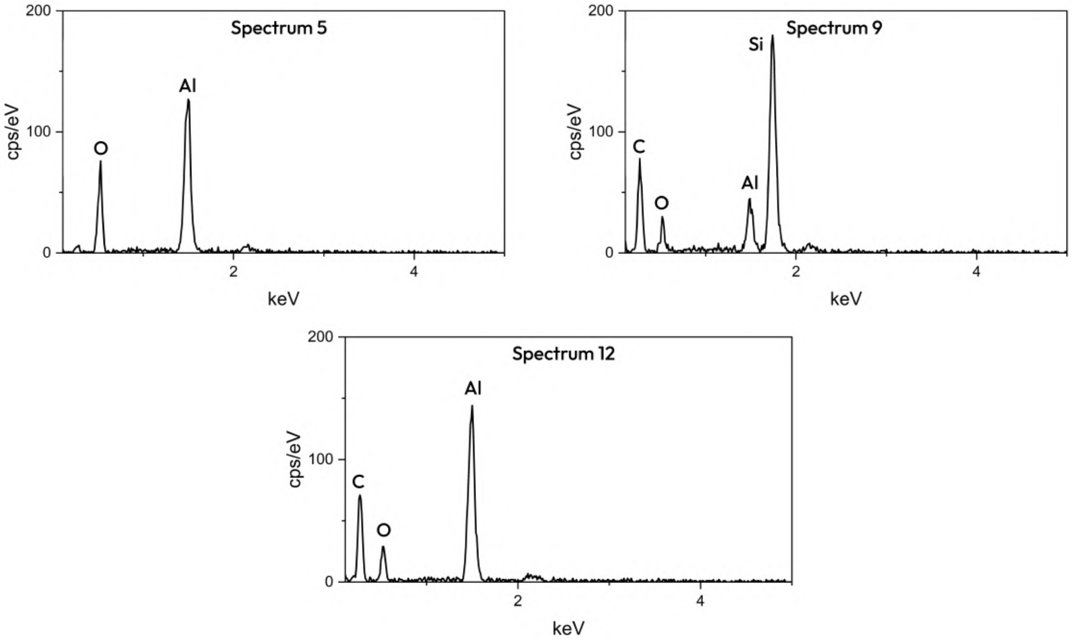

Figure D.4: Energy dispersive x-ray spectroscopy (EDS) spectra of different spot locations of the SEM picture above.